

# **Remotely Sensed Metrics Help Map Range-Wide Habitat Suitability and Identify Habitat Restoration Priorities for an Endangered Marsh Bird**

A Thesis

Presented in Partial Fulfillment of the Requirements for the

Degree of Master of Science

with a

Major in Natural Resources

in the

College of Graduate Studies

University of Idaho

by

Eamon Harrity

Major Professor: Courtney J Conway, Ph.D.

Committee Members: Tracey Johnson, Ph.D. and Brian Dennis, Ph.D.

Department Administrator: Lisette Waits, Ph.D.

May 2019

This thesis of Eamon J. Harrity, submitted for the degree of Master of Science with a Major in Natural Resources and titled “Remotely Sensed Metrics Help Map Range-Wide Habitat Suitability and Identify Habitat Restoration Priorities for an Endangered Marsh Bird,” has been reviewed in final form. Permission, as indicated by the signatures and dates below, is now granted to submit final copies to the College of Graduate Studies for approval.

Major Professor: \_\_\_\_\_ Date: \_\_\_\_\_  
Courtney J. Conway, Ph.D.

Committee Members: \_\_\_\_\_ Date: \_\_\_\_\_  
Brian Dennis, Ph.D.

Committee Members: \_\_\_\_\_ Date: \_\_\_\_\_  
Tracey N. Johnson, Ph.D.

Department  
Administrator: \_\_\_\_\_ Date: \_\_\_\_\_  
Lisette Waits, Ph.D.

## Abstract

Managers and policy-makers are often confronted with the difficult task of allocating limited resources to conservation efforts and habitat management actions. Data to inform the allocation of resources can be collected in the field, but the high costs and logistical complications of field-based approaches often render large scale field data collection efforts impractical. Satellite remote sensing has become increasingly important to informing conservation decisions because it can serve as an efficient means to collect earth observations. For example, satellite-derived data have been used to track ecosystem degradation, monitor restoration efforts, map land cover, and predict biodiversity. Significant challenges still hinder the wider application of satellite remote sensing techniques in conservation planning. For instance, using satellite imagery often requires expertise in remote sensing techniques, access to expensive image processing software, and the capacity to manage large datasets. These challenges hinder the development of useful information (e.g., habitat assessments) and the dissemination of results (e.g., maps of habitat suitability) to land managers and policy-makers.

We used publicly available Landsat data and generalized linear mixed models to link satellite-derived metrics of marsh condition with the relative abundance of the federally endangered Yuma Ridgway's rail (*Rallus obsoletus yumanensis*). We followed a rigorous model selection process to: 1) identify the most appropriate set of marsh condition variables that best predict rail abundance; 2) optimize the temporal scale at which we measured these predictors; 3) identify the optimal statistical distribution with which to model rail abundance; and 4) account for the spatio-temporal dynamics of a fragmented and stochastic ecosystem (freshwater emergent marshlands). Our model selection process allowed us to objectively select the most parsimonious model for inference. We applied the results of our rail abundance models to generate range-wide predictive maps of habitat suitability at a fine spatial grain (30 m). Such maps will help target management actions, both spatially and temporally, throughout the range of this endangered bird. Moreover, we developed a reliable way to detect wetland disturbances with Landsat imagery, which may help determine how frequently to re-apply management actions.

We addressed many of the challenges facing the use of satellite remote sensing by working with the web-based (and freely available) Google Earth Engine to process large datasets of Landsat imagery and generate maps of habitat suitability. These maps of habitat suitability are shareable, interactive, and easy to update and will enhance our ability to prioritize management actions for recovery of an endangered bird. We focused on the Yuma Ridgway's rail, but our methods could be applied to other species of conservation concern.

## **Acknowledgements**

Courtney Conway, thank you for mentoring and encouraging me during my degree. You have made me a better scientist. Tracey Johnson, from Coon Creek, Wyoming to Moscow, Idaho, you have played an important role in my career and I cannot thank you enough. Brian Dennis, thank you for challenging me to step outside of my comfort zone. Bryan Stevens, thank you for all the advice and guidance-I could not have managed this without you.

The U.S. Fish and Wildlife Service and Bureau of Land Management provided funding for my research assistantship. The Waterbird Society, Association of Field Ornithologists, and Arizona Field Ornithologists provided additional support for travel and supplies.

### **Dedication**

To my parents for their endless support, love, and encouragement. To Kelsey, I want to be like you when I grow up. To Lauren, Kate, and Dad, you made the field seasons so much better. Jared, I think the rails won.

## Table of Contents

Abstract.....	iii
Acknowledgements.....	iv
Dedication.....	v
Table of Contents.....	vi
List of Tables .....	viii
List of Figures.....	x
Introduction.....	1
Methods.....	3
Study system.....	3
Yuma Ridgway’s rail survey data .....	5
Satellite data .....	7
Spectral indices.....	8
Satellite imagery acquisition and processing.....	8
Satellite-derived metrics of marsh condition.....	10
Statistical modeling .....	13
Covariate reduction to generate a global fixed-effects model set.....	13
Identify appropriate statistical distribution .....	15
Identify appropriate random effects structure.....	18
Final model selection.....	19
Predictive maps of habitat suitability .....	20
Wetland disturbance detection .....	20
Reference disturbance data .....	20
Landsat timeseries .....	21
Spectral indices for wetland disturbance detection.....	22
Disturbance detection algorithm.....	24

Detecting wetland disturbance.....	25
Range-wide approach .....	26
Results.....	27
Modeling Yuma Ridgway’s rail relative abundance .....	27
Statistical modeling .....	29
Model performance.....	31
Final marsh condition covariates .....	31
Index performance.....	34
Wetland disturbance detection .....	35
Discussion .....	38
Modeling relative abundance of Yuma Ridgway’s rails .....	38
Wetland disturbance detection .....	42
Literature cited .....	46
Appendix A: Yuma Ridgway’s rail relative abundance modeling: Additional information .....	57
Study location descriptions.....	57
Satellite-derived metrics of marsh condition: Descriptions and justification.....	59
Spectral indices for relative rail abundance modeling.....	60
Extended modeling results .....	61
Model structure.....	70
Random Effects .....	72
Final model selection.....	72
Literature cited .....	77
Appendix B: Landsat imagery acquisition and processing .....	79
Literature cited .....	88

## List of Tables

Table 1. Summary of marsh bird survey data from 6 locations .....	6
Table 2. Spectral indices used to detect wetland disturbances in our study .....	11
Table 3. Metrics of marsh condition were derived from vegetation greenness and moisture content... 12	
Table 4. Summary of the candidate models we evaluated to identify the most appropriate statistical distribution with which to model rail counts .....	18
Table 5. Spectral indices used to detect wetland disturbances in our study .....	22
Table 6. A truncated list of model structures considered for our analyses. ....	29
Table 7. Estimated zero-inflation probability for each location in the study system.....	30
Table 8. Root Mean Squared Error of the top model calculated for each study location. ....	31
Table 9. Standardized parameter estimates from the top model .....	33
Table 10. Performance of BFAST algorithms fit with different indices .....	35
Table 11. Best performing index sets .....	36
Table A.1. Detectability models included linear and quadratic effects for time and date of survey .....	62
Table A.2. Temporal-scale optimization of accumulated greenness covariates .....	63
Table A.3. Temporal-scale optimization of accumulated vegetation moisture content covariates .....	63
Table A.4. Temporal-scale optimization of accumulated marsh condition (fused index) .....	64
Table A.5. Temporal-scale optimization of change in vegetation greenness covariates .....	64
Table A.6. Temporal-scale optimization of change in vegetation moisture covariates .....	64
Table A.7. Temporal-scale optimization of change in vegetation condition covariates (fused index)..	65
Table A.8. Temporal-scale optimization of rate of change of vegetation greenness .....	65
Table A.9. Temporal-scale optimization of rate of change of vegetation moisture content .....	65
Table A.10. Temporal-scale optimization of rate of change of fused vegetation condition covariates.	66
Table A.11. Temporal-scale optimization of maximum vegetation moisture content covariates .....	66
Table A.12. Temporal-scale optimization of maximum vegetation greenness covariates .....	66
Table A.13. Temporal-scale optimization of maximum marsh condition covariates (fused index).....	67
Table A.14. Temporal-scale optimization of minimum vegetation greenness covariates .....	67
Table A.15. Temporal-scale optimization of minimum vegetation moisture covariates. ....	67
Table A.16. Temporal-scale optimization of the minimum fused vegetation condition covariates .....	68
Table A.17. Reduced set of marsh condition covariates included in the global fixed-effects model....	68
Table A.18. Statistical distribution selection .....	71
Table A.19. Random effects structure selection .....	72

Table A.20. Final fixed-effect model selection .....	73
Table B.1. Random Forest image classification accuracies for each processing region.....	85
Table B.2. Missing images in timesereis .....	86

## List of Figures

Figure 1. Marsh bird survey points were grouped into survey routes within each study location.....	7
Figure 2. Landsat imagery processing workflow to generate timeseries of spectral indices.....	9
Figure 3. A conceptual diagram of the 4-step model selection process followed in our analyses.....	13
Figure 4. Hypothetical depiction of multiple sources of variance in Yuma Ridgway's rail count data.	19
Figure 5. A conceptual diagram of our complete modeling process. ....	20
Figure 6. Example of BFAST decomposition of an NDVI timeseries .....	25
Figure 7. Mean observed Yuma Ridgway's rail counts for all surveys conducted within each location during 2006-2018.....	27
Figure 8. Temporal trends of mean Yuma Ridgway's rail counts for each of the 6 study locations .....	28
Figure 9. Distribution of Yuma Ridgway's rail counts at each of 6 locations for all surveys conducted from 2006-2018 .....	28
Figure 10. Temporal trends in expected Yuma Ridgway's rail counts .....	30
Figure 11. Location-specific predicted and observed Yuma Ridgway's rail counts for all years.....	31
Figure 12. Expected counts of Yuma Ridgway's rails as a function of marsh condition covariates.....	34
Figure 13. Average change magnitudes of BFAST estimated breaks .....	36
Figure 14. Maps showing the number of significant breaks detected with the BFAST algorithm at survey points within 4 study locations during the previous 5 years. ....	37
Figure 15. Map of predicted habitat suitability along the Lower Colorado River.....	39
Figure 16. Average predicted relative abundance of Yuma Ridgway's rails in three managed wetland parcels within Imperial National Wildlife Refuge.....	40
Figure A.1. Correlation plot of final marsh condition covariates.....	70
Figure A.2. Zero-inflation probability for each study location.....	76
Figure A.3. Estimated relationship between the dispersion parameter and survey date.....	76
Figure B.1. Landsat imagery processing workflow used to generate timeseries of spectral indices.....	79
Figure B.2. Vegetation mask derivation process .....	82
Figure B.3 An example of a classified image clipped to a regional polygon .....	84
Figure B.4. Proportion of vegetation in the 224-m buffers of survey points through time .....	87

## INTRODUCTION

The Endangered Species Act (ESA) provides for the protection of listed species and the habitats upon which they depend. Yet, we often lack the necessary information to recover species so that they can be removed from ESA listing. Indeed, over 100 birds have been listed under the ESA since its inception, but only 8 have been sufficiently recovered to allow de-listing (U.S. Fish and Wildlife Service 2017). Managers and policy-makers are confronted with the difficult task of allocating limited resources to conservation actions, often in the face of considerable uncertainty (Bottrill et al. 2008). For example, how do we prioritize management actions spatially and temporally to maximize the benefit to listed species? Ideally, managers would have information on relative habitat suitability at potential restoration sites, the effects of proposed management/restoration actions, and a means of prioritizing areas for future management actions. Such data can be gathered through range-wide population and habitat monitoring in the field, but field-based approaches are often impractical because of high costs and time requirements.

Satellite remote sensing (i.e., satellite imagery and satellite-derived data) has become increasingly important to conservation planning because it can provide a cost-effective approach to collect data to guide conservation decisions at broad spatial scales. Satellite-derived data have been used to track ecosystem degradation, monitor restoration efforts, map land cover, and predict biodiversity (Turner et al. 2003, 2015, Salvia et al. 2012, Pettorelli et al. 2014, Cordell et al. 2017). Researchers have paired satellite-derived data with wildlife data to model relationships between vegetation condition and species diversity, occurrence, distribution, life-history traits, and migration patterns for a wide variety of organisms (Goodwin et al. 2008, Lahoz-Monfort et al. 2010, Pau et al. 2012, Wang et al. 2016). Further, satellite-derived data have been used to document changes in vegetation dynamics associated with anthropogenic disturbances (Verbesselt et al. 2010*b*, DeVries et al. 2015*b*, Muro et al. 2016, Cohen et al. 2018).

Satellite-derived data may be particularly useful for wetland conservation. Globally, wetland extent declined by 64–71% during the 20<sup>th</sup> century (Davidson 2014) and by 53% during the past 200 years in the U.S. (Dahl 2011). Wetland loss is detrimental for wetland-dependent animals and a large number of wetland-dependent species are listed as threatened or endangered in the United States (Gibbs 2000). Furthermore, wetlands are highly dynamic, sensitive to anthropogenic disturbance, and frequently inaccessible. Hence, wetlands need frequent monitoring but doing so can present insurmountable challenges.

Despite several recent examples of satellite remote sensing techniques and associated data informing conservation, significant challenges still hinder the wider application of these techniques in conservation planning. For one, using satellite-derived data often requires expertise in remote sensing techniques, access to expensive (and complicated) analytical tools, and ability to manage large datasets (e.g., numerous satellite images). Further, practitioners (e.g., managers, policy-makers, etc.) must somehow select the appropriate tools and datasets for their desired application from an overwhelming number of possibilities (e.g., satellite sensors, datasets, and data manipulation processes). Finally, many efforts to use satellite-derived data to inform conservation produce static maps or environmental assessments that may quickly become antiquated.

Our goal was to develop an efficient and effective method to document temporal and spatial variation in habitat suitability throughout the range of an endangered marsh bird using satellite-derived data. We aimed to develop a method that was both accessible to managers and easy to update on an annual basis, thereby facilitating habitat monitoring and conservation decision making. We addressed many of the traditional challenges of using satellite-derived data by using Google Earth Engine. Google Earth Engine is a cloud-based platform that facilitates large-scale analyses of geospatial data by providing a multi-petabyte catalog of publicly available data and leveraging Google's computational infrastructure. The imagery is pre-processed and analysis-ready (i.e., radiometrically calibrated and geometrically corrected), easy to access, and simple to manage (Gorelick et al. 2017). Indeed, the user does not need to download and organize massive datasets, thereby alleviating a host of data handling and management challenges. Further, Google Earth Engine offers a suite of prepackaged analytical algorithms and allows users to build user-defined functions and algorithms (Gorelick et al. 2017). Finally, Google Earth Engine users can share image processing and data analysis scripts, making it a potentially powerful tool for conservation planners.

We developed our methods for the endangered Yuma Ridgway's rail (*Rallus obsoletus yumanensis*) because it typifies many of the challenges facing the recovery of species of conservation concern. This rare bird inhabits emergent wetlands throughout the Lower Colorado River Basin in California, Arizona, Nevada, and Mexico. As a wetland-dependent bird in a desert region, the Yuma Ridgway's rail occupies an extremely limited geographic range with patches of habitat embedded within a landscape of inhospitable non-habitat. The rail's dependence on isolated emergent wetland patches in an arid region is considered a primary hurdle to successful recovery (U.S. Fish and Wildlife Service 2010). As such, land management agencies spend considerable resources securing adequate water supplies for extant marshes and implementing habitat management to maintain a mosaic of

early-successional marsh conditions for this rare bird (U.S. Fish and Wildlife Service 2010). These habitat management actions (e.g., prescribed fire or mechanical disturbance) are expensive and logistically complicated to implement at a spatial scale that will aid recovery throughout the species' range. A process to optimize habitat restoration efforts over space and time would help managers maximize benefits to Yuma Ridgway's rails.

We sought to use satellite-derived data to inform conservation actions to benefit recovery of this endangered bird. Specifically, we sought to:

- 1) Use satellite-derived metrics to model abundance of Yuma Ridgway's rails;
- 2) Map habitat suitability throughout the U.S. range of the Yuma Ridgway's rail;
- 3) Determine whether satellite imagery can accurately detect changes in marsh conditions wrought by management actions.

Satellite-derived data may serve as a viable surrogate to exhaustive field data collection to guide management decisions if we can use satellite-derived data to: 1) model heterogeneity in rail abundance, 2) predict habitat suitability at a regional scale, and 3) detect changes in marsh condition associated with disturbances. The Yuma Ridgway's rail is just one of many endangered species whose habitat has been reduced or fragmented. Hence, successful protection and recovery of most endangered species will likely require efficient allocation of limited conservation funds to maintain quality habitat. The ability to link local species abundance with satellite-derived metrics of habitat condition and accurately detect habitat disturbances will help prioritize management actions at spatial scales that can potentially recover and de-list endangered species.

## METHODS

### Study system

Our study focused on 6 locations throughout the U.S. range of the Yuma Ridgway's rail, including 4 locations along the Lower Colorado River (i.e., Havasu National Wildlife Refuge, Cibola National Wildlife Refuge, Imperial National Wildlife Refuge, and Mittry Lake Wildlife Area); 1 location along the Lower Gila River in Arizona; and 1 location along the Salton Sea, California (i.e., Sonny Bono Salton Sea National Wildlife Refuge; Fig. 1). These 6 study locations represent some of the largest populations of Yuma Ridgway's rails in the U.S., yet each location is characterized by a unique set of environmental and climatic conditions (see Appendix A for more details about the 6 study locations).

The Lower Colorado River typifies a large river substantially altered by humans. Annual spring floods once pulsed through the Colorado River watershed supplying water across wide floodplains in the lower basin and sustaining a diverse assemblage of wetland types and successional stages (Ohmart et al. 1988, Carriquiry and Sánchez 1999, Tiegs and Pohl 2005). The annual spring floods from snowmelt throughout the upper Colorado River basin created new oxbows and pocket marshes in the lower river basin, and flushed out decadent vegetation, cycled nutrients, and reset succession in extant wetlands (Ohmart et al. 1988, Christensen and Lettenmaier 2007, Conway et al. 2010). However, river regulation, water control structures, and water diversion has eliminated this annual flood cycle. Indeed, the Colorado River has become one of the most regulated and over-allocated rivers in the world during the past 150 years (Carriquiry and Sánchez 1999, Christensen and Lettenmaier 2007, Glenn et al. 2008).

Without the annual spring floods, new emergent marshes are not created in the Lower Colorado River floodplain and extant marshes senesce (e.g., accumulate decadent vegetation and are encroached by woody vegetation; Ohmart et al. 1988, Glenn et al. 2008, Hinojosa-Huerta et al. 2008). Moreover, bank stabilization and stream channelization have cut off many of the areas within the lower floodplain that once supported emergent marsh vegetation (e.g., backwaters, meanders, and side channels) from the main river channel. Consequently, extant emergent wetlands are rare and restricted to the main channel or to backwaters managed for mitigation (Glenn et al. 2008, Hinojosa-Huerta et al. 2008, U.S Fish and Wildlife Service 2010, Mexicano et al. 2013).

The Lower Gila River faces many of the same challenges as the Lower Colorado River. Water from the Lower Gila River is largely diverted for municipal and agricultural use and consequently, the river is nearly dewatered (Huckleberry 1994, Cohen et al. 2001, Glenn et al. 2008). Wetland parcels are generally small and separated by large expanses of dry river bed or salt cedar (*Tamarix spp.*) thickets. Furthermore, extant wetlands along the Lower Gila River often depend solely on recycled agricultural water, ephemeral seeps, and mitigation efforts. As such, emergent wetland vegetation is dynamic along the Lower Gila River, expanding and contracting in response to water availability.

The Sonny Bono (S.B.) Salton Sea National Wildlife Refuge is on the shores of the Salton Sea, California and includes 334 ha of wetlands in irrigated units (69 of the 334 ha are explicitly managed as Yuma Ridgway's rail habitat). New emergent marshes have expanded recently along the shores of the Salton Sea (mainly off refuge) and these unmanaged wetlands are fed entirely by recycled water (e.g., agricultural run-off) from the New and Alamo Rivers (Barnum et al. 2017).

Recent surveys suggest the rails are expanding into these unmanaged marshes (U.S. Fish and Wildlife Service, unpublished data), but it is unknown if these wetlands: 1) provide quality habitat for rails, or 2) how long the unmanaged marshes will persist given decreasing water levels at the Salton Sea (Barnum et al. 2017).

Yuma Ridgway's rail populations are negatively impacted by the loss of wetlands and, importantly, the senescence of extant wetlands (Conway et al. 2010). Rails in senescent marshes with dense mats of dead vegetation may face higher predation risk as they are forced to walk over the mats of dead vegetation. Moreover, dense layers of decadent vegetation may impede foraging by restricting access to the soil substrate, as well as hindering rail movement through the marsh (Conway et al. 2010).

Yuma Ridgway's rails respond positively to habitat management actions that reset marsh succession. Abundance of Yuma Ridgway's rails increased in years following wetland fires along the Lower Colorado River (Conway et al. 2010). A similar pattern was observed in the Colorado River Delta, where rail abundance was higher in recently burned wetlands compared to undisturbed wetlands (Gomez-Sapiens 2014). Management actions (e.g., prescribed fire and mechanical mowing) flush out decadent vegetation, return nutrients to the soil, and facilitate regrowth of emergent vegetation; such changes may improve foraging efficiency, reduce predation risk, and enhance the reproductive success of Yuma Ridgway's rails. As such, managers have effective management tools, but they are unable to prioritize the application of those effective management actions in space and time on a scale that will lead to recovery of the species.

#### Yuma Ridgway's rail survey data

Land management agencies conduct annual marsh bird surveys throughout the range of the Yuma Ridgway's rail. Survey methods follow the North American standardized marsh bird survey protocol (Conway 2011) and the resulting data are housed on the Avian Knowledge Network. Surveys include a passive segment and a call-broadcast segment to increase marsh bird response rates (Conway and Gibbs 2011, Nadeau et al. 2013). All surveys broadcast Yuma Ridgway's rail vocalizations and are conducted from March – July (as suggested by Conway 2011).

We analyzed marsh bird survey data collected within the 6 locations during a 13-year period, from 2006-2018 (Table 1). Within each location, survey points were grouped into survey routes: spatially clustered survey points that were visited on a single day (Fig. 1). Survey routes were surveyed 1-3 times annually and we included all survey routes in our analyses that met 2 criteria: 1) >1

year of survey data were recorded (so that we could examine trend estimates); and 2) >3 Yuma Ridgway's rail detections were recorded during the entire survey window (2006-2018). We analyzed data from 13,190 surveys conducted at 569 survey points associated with 58 survey routes (Table 1, Fig. 1).

Table 1. We used marsh bird survey data from 6 locations: 4 along the Lower Colorado River, 1 along the Lower Gila River, and 1 at the Salton Sea. Survey points were grouped into survey routes (i.e., clusters of points that were visited on the same morning). NWR = National Wildlife Refuge.

Study location	Years surveyed	Survey routes	Survey points
Lower Colorado River			
Havasu NWR	2006-18	11	126
Cibola NWR	2008-17	7	72
Imperial NWR	2006-17	8	53
Mittry Lake Wildlife Area	2006-18	11	139
Outside Lower Colorado River			
Lower Gila River	2006-18	7	93
S.B. Salton Sea NWR	2006-18	14	86

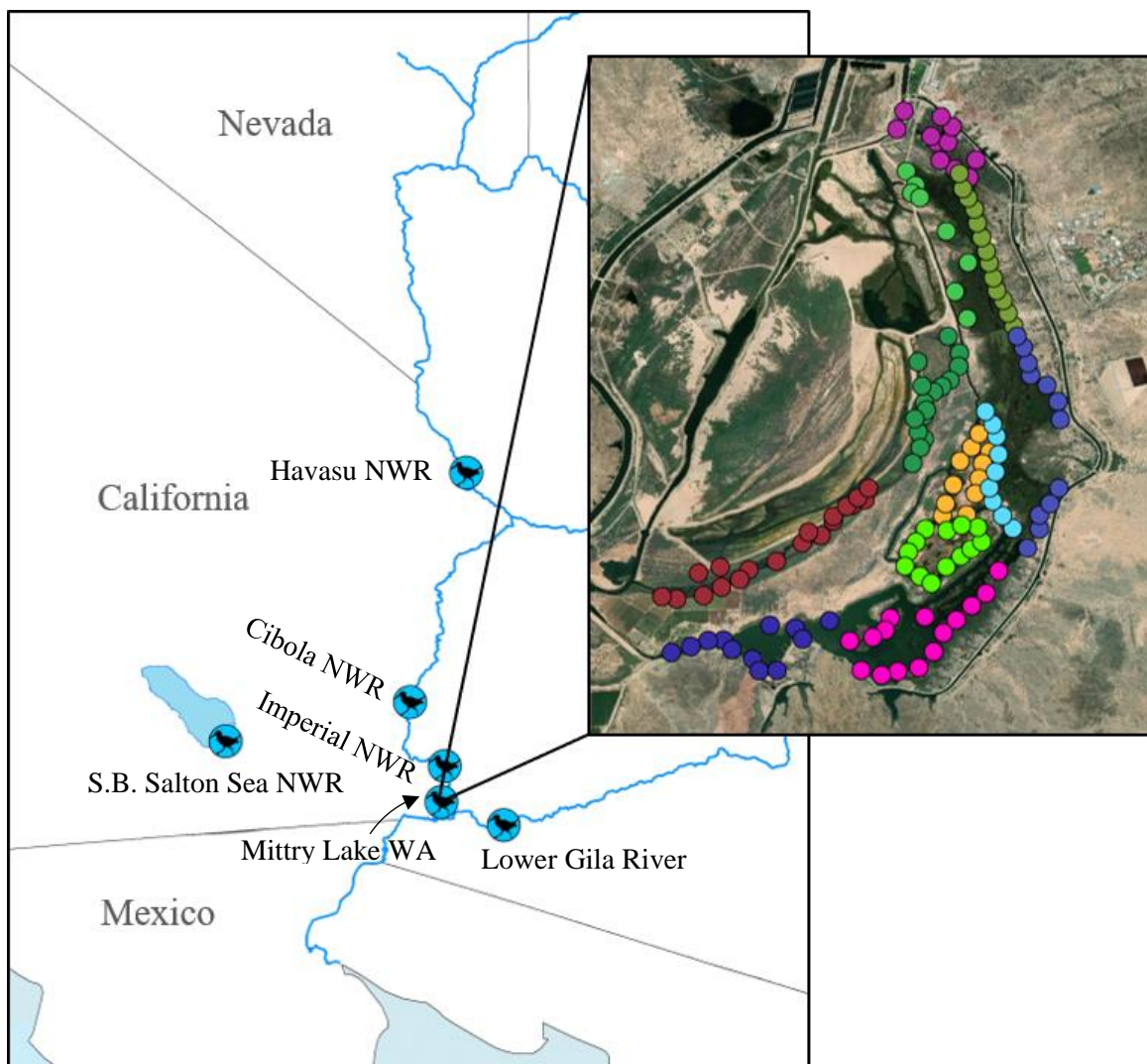


Figure 1. We used marsh bird survey data from 6 locations. Survey points were grouped into survey routes (inset is an example of Mittry Lake Wildlife Area; colors represent unique routes). All points on a route were surveyed on the same day. NWR = National Wildlife Refuge and WA = Wildlife Area.

#### Satellite data

The temporal and spatial resolution make Landsat imagery well suited to the needs of our study (i.e., long-term habitat monitoring and detection of major vegetation disturbances). Landsat is a joint initiative between the U.S. Geological Survey and National Aeronautics and Space Administration that continuously collects global earth observations in the visible and near infra-red wavelengths at a spatial resolution of 30 m (Lang et al. 2015, U.S. Geological Survey 2016). Landsat satellites collect imagery every 8–16 days and the entire Landsat archive (several decades of imagery) was made public in 2009 (Pettorelli et al. 2014, U.S. Geological Survey 2016). Satellite sensors with

finer spatial resolution (e.g., QuickBird with spatial resolution <1 m) or finer temporal resolution (e.g., MODIS with daily imagery) exist, but no product combines the spatio-temporal resolution and accessibility of Landsat imagery (the entire Landsat archive is easily accessible via Google Earth Engine; Turner et al. 2015, Gorelick et al. 2017).

### Spectral indices

Spectral indices are unique combinations of satellite bands designed to highlight specific earth features. The normalized difference vegetation index (NDVI) is arguably the most commonly used spectral index for ecological studies and applications (Kerr and Ostrovsky 2003, Pettorelli et al. 2011). However, many other spectral indices exist to monitor vegetation dynamics (Xue and Su 2017) and they can be loosely grouped into 2 categories: 1) those designed to measure vegetation greenness, and 2) those designed to measure vegetation moisture content. Greenness indices are sensitive leaf pigments (chlorophyll), photosynthetic capacity, and vegetation density (Tucker 1979, DeVries et al. 2015b, Schultz et al. 2016). Moisture indices correlate with vegetation moisture content, canopy structure, and productivity (Kauth and Thomas 1976, Gao 1996, Wilson and Sader 2002). We evaluated the ability of several spectral indices to: 1) predict rail abundance, and 2) detect major wetland disturbances that setback succession.

### Satellite imagery acquisition and processing

We acquired and processed all Landsat imagery on the Google Earth Engine platform (Gorelick et al. 2017). We followed a 9-step workflow to process all imagery and derive monthly measurements of vegetation condition for all study sites.

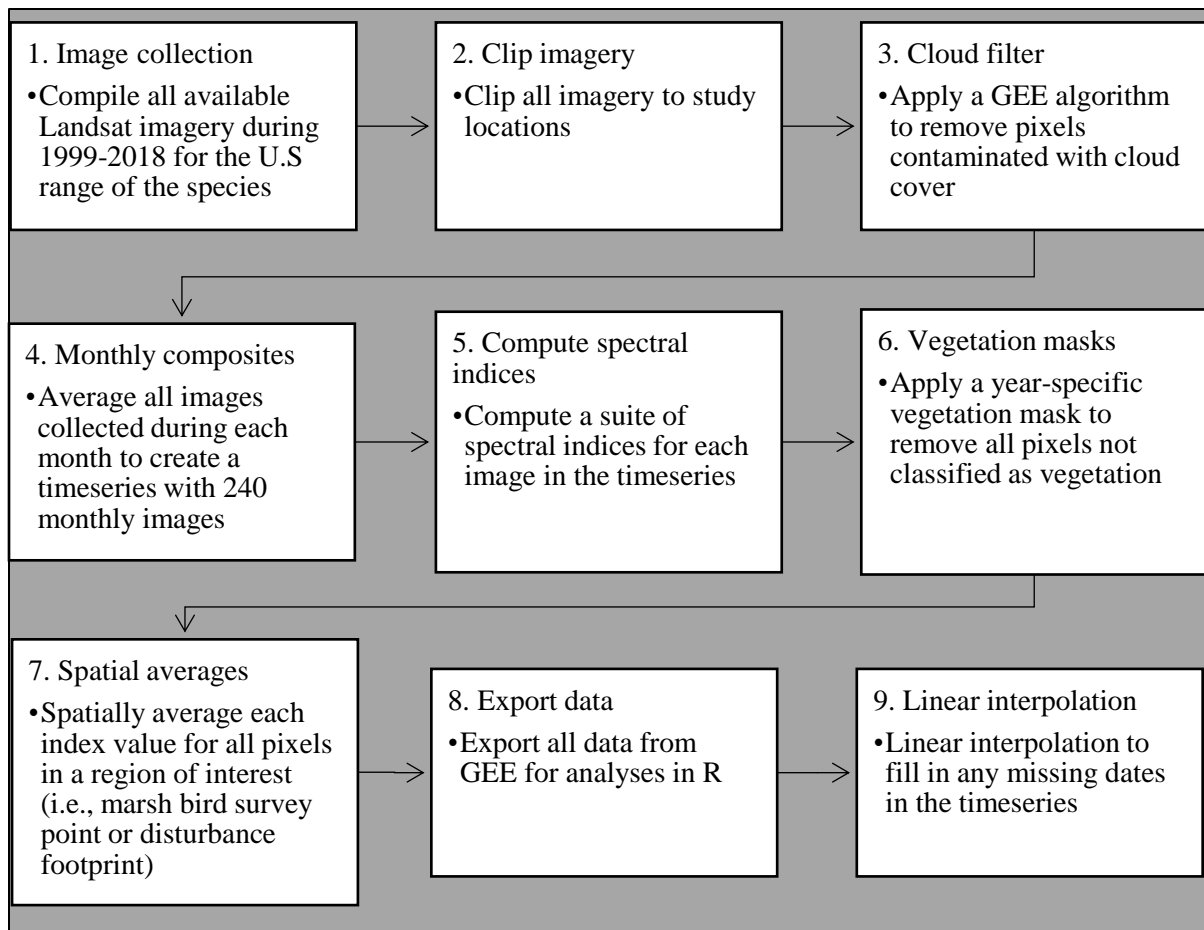


Figure 2. Landsat imagery processing workflow that we used to generate timeseries of spectral indices. GEE = Google Earth Engine. See Appendix B for a detailed description of our image processing workflow.

The spatial scale at which animals respond to their environment is an important consideration for spatially explicit efforts to model habitat suitability (Johnson 1980, McGarigal et al. 2016). Recent Yuma Ridgway’s rail occupancy models identified 224 m as a useful scale for modeling the response of rails to habitat variables (Glisson et al. 2017). Moreover, 96.3% of all Yuma Ridgway’s rails detected during surveys were estimated to be  $\leq 225$  m of the survey point. Therefore, we measured all marsh covariates in a 224-m buffer around the survey points. That is, we spatially averaged all the pixels within a 224-m buffer of each survey point and used these point estimates to derive marsh condition covariates (see Appendix B for more details).

### Satellite-derived metrics of marsh condition

Decadent vegetation, sedimentation, and woody vegetation increases over time within wetlands (in the absence of disturbance) and these successional changes negatively affect Yuma Ridgway's rails (Conway et al. 2010). We therefore derived covariates from spectral indices that would correlate with marsh condition and seral stage (and thus rail habitat suitability). In defining covariates of marsh condition, we sought to identify: 1) metrics of marsh condition that best reflected rail habitat suitability (e.g., annual vegetation greenness); 2) the most appropriate temporal scale at which to measure marsh condition (e.g., are marsh condition metrics measured during the breeding season more informative than those measured over the whole year?); and 3) suitable spectral indices with which to measure important marsh condition metrics. Spectral indices vary in their sensitivity to noise (e.g., atmospheric interference), and thus in their ability to document and monitor vegetation condition (Huete 1988, Gao 1996, Xue and Su 2017, Healey et al. 2018). Hence, we considered several spectral indices that are widely used to measure vegetation greenness or vegetation moisture content, and a fused index designed to capture variation in both vegetation greenness and moisture (Table 2). Our goal was to identify the most appropriate marsh condition covariates with which to model heterogeneity in relative abundance of rails (Table 3).

Table 2. Spectral indices that we used to detect wetland disturbances. Formula refers to combination of bands and coefficients used to calculate each spectral index. Color of index label refers to: green = greenness index, blue = vegetation moisture index, and purple = fused index. See Appendix A for additional index descriptions.

Index	Name	Formula	Justification	Key Citations
NDVI	Normalized Difference Vegetation Index	$\frac{NIR - Red}{NIR + Red}$	NDVI is the most commonly used vegetation index for ecological studies. It correlates with vegetation greenness and primary productivity.	(Tucker 1979, Pettorelli et al. 2005)
TCG	Tasseled Cap Greenness	$-0.3344 * Blue + -0.3544 * Green + -0.4556 * Red + 0.6966 * NIR - 0.0242 * SWIR - 0.2630 * SWIR2$	Correlates with vegetation density and greenness	(Kauth and Thomas 1976)
NDMI	Normalized Difference Moisture Index	$\frac{NIR - SWIR}{NIR + SWIR}$	Correlates with vegetation moisture	(Gao 1996, Wilson and Sader 2002)
TCW	Tasseled Cap Wetness	$0.2626 * Blue + 0.2141 * Green + 0.0926 * Red + 0.0656 * NIR - 0.7629 * SWIR - 0.5388 * SWIR2$	Correlates with vegetation moisture and soil moisture	(Kauth and Thomas 1976, Crist 1985)
NVMI	NDVI fused with NDMI	$NDVI + NDMI$	Fused index designed to describe variation in vegetation moisture and greenness	(Kennedy et al. 2018)

Table 3. We considered several metrics for each marsh condition covariate to help quantify spatio-temporal variation in Yuma Ridgway's rail habitat condition. Predicted direction of rail response indicates the hypothesized relationship between the marsh condition covariate and rail abundance. The final 2 columns detail the different temporal scales at which we calculated marsh condition covariates and the indices used to measure each covariate. Index colors: green = vegetation greenness indices, blue = vegetation moisture indices, and purple = the fused index, NVMI. Proportion of vegetation (final row) does not have associated indices. See Appendix A for additional covariate descriptions.

Marsh condition covariates	Justification	Predicted rail response	Temporal scales considered	Index
Maximum vegetation greenness or moisture	As decadent vegetation increases, maximum vegetation greenness and moisture should decrease	+	Current full year Current breeding season Previous full year Previous breeding season	NDVI TCG NDMI TCW NVMI
Minimum vegetation greenness	Non-native phragmites may inflate minimum greenness values	-	Current full year Current breeding season Previous full year Previous breeding season	NDVI TCG NVMI
Minimum vegetation moisture	Phragmites and decadent vegetation mats may inflate minimum vegetation moisture values	-	Current full year Current breeding season Previous full year Previous breeding season	NDMI TCG NVMI
Rate of vegetation growth	Decadent vegetation may suppress emergent vegetation growth rates and late seral stage marshes may show more gradual annual vegetation green-up than early successional emergent marshes	+	Current full year Current breeding season Previous full year Previous breeding season	NDVI TCG NDMI TCW NVMI
Change in vegetation greenness or moisture	Seasonality (the amount of annual change) may be negatively correlated with decadent vegetation	+	Current full year Current breeding season Previous full year Previous breeding season	NDVI TCG NDMI TCW NVMI
Accumulated vegetation greenness or moisture	Accumulated greenness and moisture should inform marsh condition through time and should be negatively correlated with wetland seral stage	+	5-year accumulated sum 3-year accumulated sum 2-year accumulated sum	NDVI TCG NDMI TCW NVMI
Instantaneous vegetation greenness or moisture	Greenness and moisture values at the time of surveys should reflect marsh condition at the time of surveys	+	Concurrent with survey	NDVI TCG NDMI TCW NVMI
Proportion vegetated	Proportion of vegetation within 224-m buffer of survey points will reflect the amount of habitat	+	Current full year	NA

## Statistical modeling

Counts of animals are frequently used as indices of abundance (Krebs 2001). We used counts of Yuma Ridgway's rails detected during each survey to address questions regarding the effects of marsh condition on relative rail abundance. We investigated these questions with generalized linear mixed models (GLMM). We used a 4-step model selection process to identify a final model because of the large number of potential predictor variables, the multiple plausible statistical distributions for modeling counts (e.g., Poisson, Negative Binomial), and the spatio-temporal structure of our observed data. The 4 steps included: 1) reduce the list of candidate predictor variables hypothesized a priori to create a final, reduced set of most useful covariates, and therefore a global fixed-effects model; 2) identify the most appropriate statistical distribution for modeling the count data; 3) identify an appropriate random-effects structure that captures the spatio-temporal dependence of counts; and 4) conduct fixed-effects model selection (conditional on #1-3 above) to identify a final, parsimonious GLMM for making inferences about effects of marsh condition on relative rail abundance (Fig. 3). We used Akaike's Information Criterion (AIC) for all stages of model selection, which we describe in detail below.

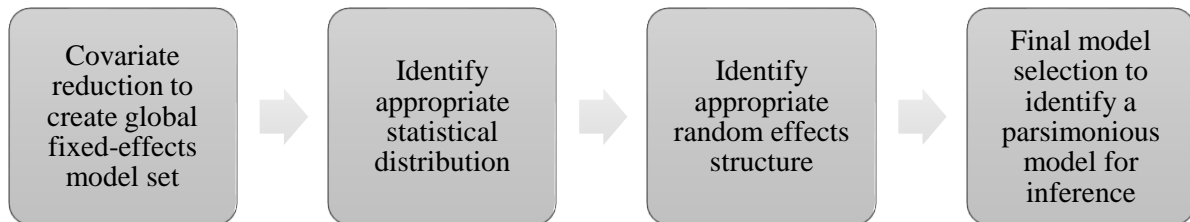


Figure 3. A conceptual diagram of the 4-step model selection process that we followed in our analyses.

### Covariate reduction to create a global fixed-effects model set

*Detection probability* – Imperfect detection complicates efforts to understand how environmental condition affects species occurrence and abundance (Royle 2004, Sauer and Link 2011). Ignoring imperfect detection when modeling abundance or occurrence data can bias estimates and cause incorrect inferences (Fiske and Chandler 2011). We controlled for variation in detection by including nuisance fixed-effects covariates in the count model. Such an approach allowed us to model changes in relative rail abundance as a function of marsh condition covariates while also accounting for imperfect detection during call-broadcast surveys (see Sauer and Link 2011, Barker et al. 2018).

We included covariates known to affect rail detectability: time of day and date of survey (Conway and Gibbs 2011, Glisson et al. 2017). We included time of day as minutes after sunrise and survey date as the Julian day of the year. We used a fixed-effects negative binomial regression (with only detection covariates) to fit all possible combinations of detection covariates and used AIC to identify the most appropriate detection covariates to include in subsequent analyses.

*Marsh condition covariates* – We considered 116 candidate marsh condition variables because we sought to identify: 1) the marsh condition metrics that best predicted relative rail abundance (e.g., maximum annual vegetation greenness vs maximum annual vegetation moisture), 2) the most suitable temporal scale at which to measure those metrics (e.g., current breeding season vs previous breeding season), and 3) the best spectral index with which to measure important marsh condition metrics. As such, we took 3 steps to reduce the list of candidate marsh condition covariates: 1) temporal-scale optimization, 2) category-specific scale-optimized covariate reduction, and 3) all category scale-optimized variable reduction. We fit negative binomial regression models (including the detection covariates identified above) and a single marsh condition covariate (separately for each variable) and used AIC to rank models.

1) *Temporal scale optimization* – We selected the most appropriate temporal scale separately for each spectral index. For example, we fit models (as described above) with maximum NDVI calculated at all 4 temporal scales and selected the most parsimonious model. We repeated this process with 6 marsh condition covariates (top 6 rows of Table 3). We derived instantaneous greenness and moisture and proportion of vegetation for the current year only, and thus did not need to select the optimal temporal scale for these variables.

2) *Category-specific scale-optimized covariate reduction* – Once we selected the appropriate temporal scale for each covariate, we then assessed collinearity of all covariates within each category (i.e., vegetation greenness, vegetation moisture, and fused index). We dropped the weaker (larger AIC in univariate analyses) of any pair of covariates with a correlation coefficient  $>0.7$ . Collinearity increases the variance of parameter estimates but typically must be quite strong ( $\geq 0.8$ ) to substantively affect precision of parameter estimation (Fox 2015).

3) *All category scale-optimized covariate reduction* – Finally, we grouped all remaining covariates (regardless of category) and again dropped the weaker of any pair of covariates with a correlation coefficient  $>0.7$ . We included the reduced set of marsh condition covariates in all

subsequent model selection steps until the final stage, when we selected the most parsimonious fixed-effects model structure.

Identify appropriate statistical distribution

*Accounting for overdispersion* – Count data are commonly modeled as arising from a Poisson process (Lynch et al. 2014), but ecological count data commonly violate the Poisson assumption of equi-dispersion (i.e., equal mean and variance) and are thus overdispersed (i.e., the observed variance is greater than the mean; Rhodes 2015). Overdispersion can be caused by ecological processes, such as clustering of individuals in high-quality habitat, or sampling processes such as imperfect detection (Martin et al. 2005, Lindén and Mäntyniemi 2011). When the equi-dispersion assumption of the Poisson distribution is violated, the negative binomial distribution is commonly used to model count data (Hilbe 2011, Lindén and Mäntyniemi 2011, Irwin et al. 2013). The negative binomial distribution uses one or more additional parameters to describe the mean-variance relationship (Lindén and Mäntyniemi 2011), where the variance is often modeled as a quadratic function of the mean ( $\mu$ ), but alternative parameterizations are available (Hilbe 2011, Lindén and Mäntyniemi 2011). To accommodate the possibility of overdispersion in rail counts we considered 3 candidate distributions that are commonly used to model count data:

- 1) Poisson, where  $Var = \mu = \lambda$ ,
- 2) Negative Binomial<sub>1</sub> (NB1), where  $Var = \mu(1 + \theta)$ , and
- 3) Negative Binomial<sub>2</sub> (NB2), where  $Var = \mu(1 + \mu/\theta)$ .

Thus, the parameter  $\theta$  governs the magnitude of overdispersion, where the NB1 and NB2 distributions assume the variance increased linearly and quadratically with the mean, respectively.

Even with flexible distributions like the NB1 and NB2, the base models described above assume the variance-mean relationship, and thus the amount and form of overdispersion, is unchanging in space and time. However, the variance-mean relationship may not be static in space and time. In such a situation, the above distributions may not adequately capture the overdispersion present in the data. We can model the mean-variance relationship beyond what is specified by the distributions above by using generalize regression to directly model heterogeneity in  $\theta$  (Brooks et al. 2017). For example, we hypothesized that rail vocalization behavior and likelihood of vocalizing in response to the call-broadcast would change across the breeding season and be either: 1) more erratic at the end of the breeding season compared to earlier (i.e., a linear effect), or 2) more erratic during both the early and late stages of the breeding season but less so during the peak of breeding activities (i.e., a

quadratic effect). Whereas the survey date is already included in the model as a nuisance detection covariate affecting mean counts, both overdispersion models above (i.e., NB1 and NB2) would imply the magnitude of the variance changes consistently with the mean. For example, if average detection probability decreased later in the breeding season due to less frequent vocalization, the variance would decrease as well. In contrast, here we are suggesting that even as mean counts change over the breeding season due to changes in calling frequency, we expect the variance of those counts to remain high or possibly increase because the calling behavior of individual birds may also become more variable (either late in the season or early and late). Hence, we considered statistical models where  $\theta$  was modeled directly as a function of survey date using log-linear regression, and tested whether a linear, quadratic, or no effect was most supported:

$$\log(\theta_{i,j,s,t}) = \gamma_0 + \gamma_1 \times DOY_{i,j,s,t}$$

$$\log(\theta_{i,j,s,t}) = \gamma_0 + \gamma_1 \times DOY_{i,j,s,t} + \gamma_2 \times DOY_{i,j,s,t}^2,$$

where  $\gamma$ 's are regression coefficients, DOY is the Julian day,  $i$  is point,  $j$  is route,  $s$  is survey, and  $t$  is year.

*Accounting for zero-inflation* – Counts of animals (especially rare species) often contain more zeros than would be expected under the specified statistical model (Martin et al. 2005). If the prevalence of zero observations is high, researchers can use zero-inflated count models to more accurately model the frequency of zeros in the data (Warton 2005). Zero-inflated models are mixture models where observed data are generated from two distinct distributions: a point mass at 0 that generates so-called structural zeros (i.e., counts that cannot be non-zero), and count distributions with a mean  $> 0$  (i.e., counts that can include sampling zeros but can also include non-zero integers; Martin et al. 2005, Rhodes 2015). Zero-inflated models thus allow researchers to account for excess zeros in the data and also make inferences about the processes that produce both structural zeros and non-zero counts using generalized regression (Martin et al. 2005, Rhodes 2015). For example, counts of rails may depend on habitat suitability- unsuitable sites result in structural zeros, whereas counts at sampled sites that are suitable may be  $\geq 0$  and affected by different sets of processes (e.g., greenness or senescence of a marsh, etc.). Therefore, we can model both the probability a site is suitable, and then given it is suitable, model the relative number of rails as a function of covariates.

Just as with the dispersion parameter in a negative binomial distribution, we can model the zero-inflation probability as a function of covariates to make inferences about the processes underlying

the observed rail counts. In our study system, the proportion of routes that fall in suitable habitat varies among the 6 locations; some locations have proportionally more routes in habitat that is ephemeral and thus may be frequently unsuitable (e.g., the Lower Gila River). Thus, we expect the background prevalence of rails in such locations (i.e., the fraction of the study location that is occupied) to be lower, resulting in a higher proportion of structural zeros in the data observed at those sites. We also expected the proportion of routes passing through suitable habitat to vary annually because of the ephemerality of some wetlands, especially, along the Lower Gila River and Salton Sea where water levels are more dynamic than along the Lower Colorado River. As such, we tested 3 candidate zero-inflation models for each of our 7 candidate distributions described above: constant zero-inflation probability, zero-inflation as a function of study location, and zero-inflation as a function of study location with a location-specific random intercept for year. Specifically, we compared the following 3 zero-inflation models:

- 1) constant zero-inflation probability across all locations

$$\text{logit}(p^{(ZI)}) = \phi_0,$$

- 2) zero-inflation probability varies by location

$$\text{logit}(p^{(ZI)}) = \phi_0 + \phi_{\text{location}_j},$$

- 3) zero-inflation varies by location and includes a location-specific random intercept

$$\text{logit}(p^{(ZI)}) = \phi_0 + \phi_{\text{location}_j} + r_{j,t},$$

where  $\phi$ 's are regression coefficients,  $p^{(ZI)}$  is the zero-inflation probability (i.e., the probability a 0 was a structural zero that arose from a point mass on zero),  $r$  is the location-specific annual intercept,  $j$  is study location, and  $t$  is year.

In all, we tested 28 candidate models to find the most appropriate statistical distribution for the data (Table 4; see Table A.18 for a complete list). The global model structure for both the fixed and random effects was used for determining the most appropriate statistical distribution.

Table 4. Summary of the candidate models we evaluated to identify the most appropriate statistical distribution with which to model rail counts. We considered each combination of dispersion parameterizations and zero-inflation parameterizations. This resulted in 12 possible NB1 models, 12 possible NB2 models, and 4 possible Poisson models. NB = negative binomial.

Distribution	Dispersion		Zero-inflation		
	Date	Date <sup>2</sup>	Constant	Location	Location-specific annual intercept
NB1	x	x	x	x	x
NB2	x	x	x	x	x
Poisson	NA	NA	x	x	x

*Identify appropriate random effects structure*

After specifying the optimal statistical distribution with which to model the rail counts, we selected a random effects structure to best account for the spatio-temporal structure of the data. The rail counts were spatially structured with survey points grouped into routes and routes grouped within the 6 study locations and we sought to address 4 sources of variation in rail counts via random effects: 1) route-level (spatial) variation, 2) broad-scale annual variation (i.e., a year effect shared by all rail populations), 3) local, route-specific annual variation, and 4) route-specific random time trend slopes (over the study duration). In other words, we considered random intercepts for routes and years, an annual random intercept at the route level, and a random slope for time trends by route (Fig. 4). We fit the global model (i.e., all fixed-effects and the optimal statistical distribution described above) with 7 plausible combinations of the random effects and used AIC to select the best random effects structure (Table A.19).

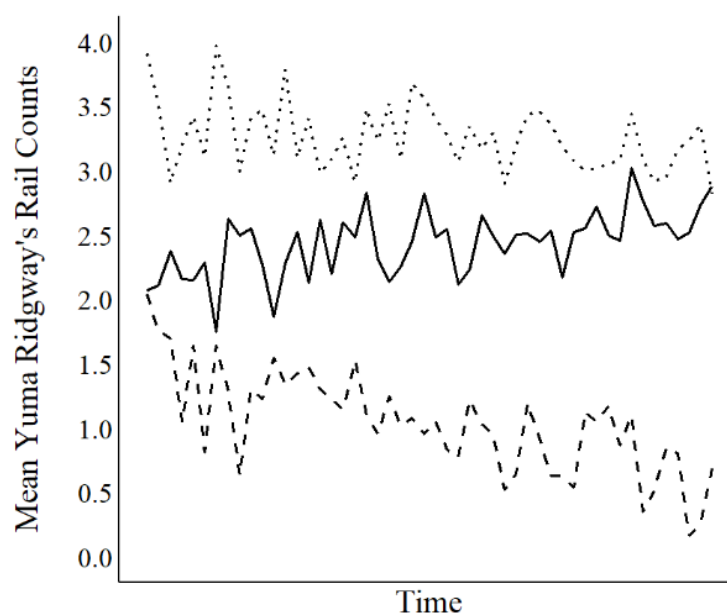


Figure 4. Hypothetical depiction of multiple sources of variance in Yuma Ridgway's rail count data. Line types represent 3 hypothetical routes. The rail counts at each route show 1) spatial variation, 2) route-specific annual variation, 3) broad-scale annual variation shared among sites (partially masked by route-specific annual variation), and 4) route-specific temporal trends (slopes).

### Final model selection

Once we identified the optimal distribution and random effects structure, we compared 27 models with unique combinations of marsh condition covariates and used AIC to identify the most parsimonious model (Table A.20). We visualized the relationship between expected rail counts and the suite of fixed-effect covariates in the final model by generating partial-effect plots. We used the final model to generate predictions of expected rail counts under a range of values for each predictor while holding all other predictors at their mean observed value. For example, we investigated the relationship between rail counts and accumulated vegetation moisture by predicting rail counts under the full range of observed accumulated vegetation moisture values while holding all other predictors at their means. Finally, we generated confidence intervals around all estimated coefficients using nonparametric bootstrap sampling. We iteratively sampled our data 1000 times and refit our top model to the resampled data. We extracted the model coefficients at each iteration and used these to estimate

95% confidence intervals. All GLMM models were fit in R using the glmmTMB package (Brooks et al. 2017).

### Predictive maps of habitat suitability

We used coefficients for marsh condition covariates in the top model to generate predictive maps of relative habitat suitability (in terms of predicted relative rail abundance) throughout the range of the Yuma Ridgway's rail (Fig.5). We generated raster layers in Google Earth Engine of all the top marsh condition covariates and applied their associated coefficients to create maps of predicted relative abundance of Yuma Ridgway's rails. We used predicted relative rail abundance as a measure of relative habitat suitability. We used the National Wetland Inventory emergent wetland layer (clipped to the U.S. range of the Yuma Ridgway's rail) to constrain predictions. That is, we clipped all marsh condition rasters to the emergent wetland layer to limit predictions of habitat suitability to emergent wetland areas. Finally, we held all nuisance detectability covariates at their mean.

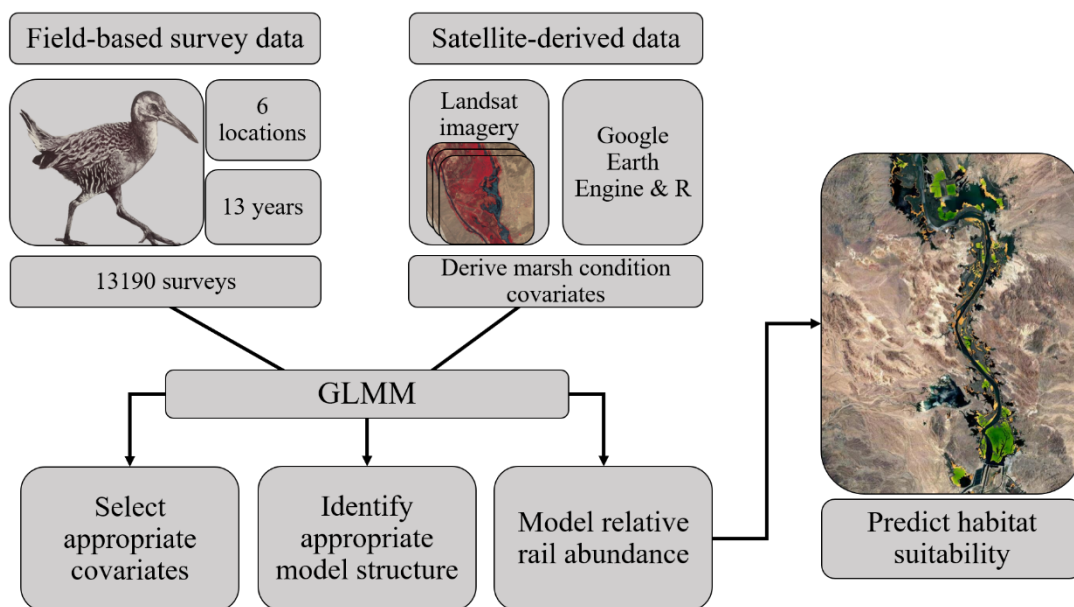


Figure 5. A conceptual diagram of our complete modeling process.

### Wetland disturbance detection

#### Reference disturbance data

Some land management agencies use prescribed fire and mechanical means to periodically reset succession of marsh vegetation, reduce decadent vegetation and remove woody vegetation in marshes (Conway et al. 2010, U.S Fish and Wildlife Service 2010). We compiled a list of the dates

and locations of prescribed fires (n=24), mechanical clearing of marsh vegetation (n=1), and natural fires >10 ha (n=3) at Imperial National Wildlife Refuge, S.B. Salton Sea National Wildlife Refuge, and Mittry Lake Wildlife Area. We used these 28 marsh “disturbances” to document how well Landsat imagery can detect and document such disturbances. Marsh disturbance data from other areas within the rail’s range were poorly recorded and were often missing important reference information (i.e., date and specific location of marsh disturbance events).

For each disturbance, we defined a “disturbance footprint.” Management actions were always associated with a managed marsh parcel, and thus we delineated the disturbance footprint of management actions as the perimeter of the associated marsh parcel. Some marsh parcels were associated with multiple management actions. We obtained fire perimeter shapefiles for the 3 natural fires from the Bureau of Land Management.

### Landsat timeseries

Landsat imagery has been used to detect and characterize disturbances in a wide range of plant communities, including forested ecosystems (Wilson and Sader 2002, DeVries et al. 2015b) and grasslands (Hutchinson et al. 2015). The detection of disturbances in wetlands is complicated because wetlands tend to be highly dynamic systems with a mixture of vegetation, saturated soils, and fluctuating water levels. These wetland characteristics can cause substantial variation in the spectral characteristics of Landsat imagery (Gallant 2015). Such variation has complicated traditional change detection approaches (e.g., image differencing, comparison of classified images through time) because any one image may show significant difference based solely on the dynamics of the wetland. However, since the opening of the Landsat image archive to the public in 2009, change detection techniques using dense timeseries (e.g., monthly images) have gained popularity (Verbesselt et al. 2010b, Forkel et al. 2013, Cohen et al. 2018). Temporally dense timeseries allow one to account for variation in a highly dynamic system (e.g., wetlands), thereby facilitating the detection of disturbances (Wei et al. 2017, Cohen et al. 2018).

We extracted monthly spectral index values from 1999-2018 for each disturbance footprint to create 20-year timeseries with 240 monthly spectral index values to ensure we had imagery representing all reference disturbances (the earliest disturbance occurred February 2001). We followed explicit steps for acquiring and processing the Landsat imagery (Appendix B).

### Spectral indices for wetland disturbance detection

Efforts to detect substantive changes in vegetation (i.e. disturbances) via spectral indices often rely on a single band or spectral index. For example, researchers have used NDVI to detect changes in forests (Verbesselt et al. 2010a), coastal mangroves (Alatorre et al. 2016), and grasslands (Hutchinson et al. 2015). The normalized difference moisture index (NDMI) is an index of vegetation moisture content (Gao 1996) and has also been widely used to detect disturbances in vegetated systems (Wilson and Sader 2002, Hislop et al. 2018). The Normalized Burn Ratio (NBR) was developed to highlight changes in soil moisture and vegetation condition after fires and has been used in a diversity of systems to detect fire-related disturbances (Key and Benson 2005, Fornacca et al. 2018). Finally, disturbance detection in wetland systems has relied on a range of indices, including NDVI, NDMI, and Tasseled Cap Wetness (Fickas et al. 2016, Wei et al. 2017).

The ability to detect disturbances with a Landsat timeseries can be hindered by “noise” in the imagery (e.g., atmospheric interference, vegetation phenology). Single indices vary in their sensitivity to these sources of noise (Kennedy et al. 2010, Cohen et al. 2018) and, hence, researchers have recently relied on multiple indices (Cohen et al. 2017, 2018, Healey et al. 2018, Hislop et al. 2018) and fused indices (i.e., multiple indices merged to capture more spectral variation; Kennedy et al. 2018) to detect disturbances with greater sensitivity and accuracy. To this end, we evaluated the ability of 14 spectral indices to detect changes in wetland vegetation associated with disturbance events (i.e., management actions and natural fires; Table 5).

Table 5. Spectral indices used to detect wetland disturbances in our study. Formula refers to combination of bands and coefficients used to calculate each spectral index.

Index	Name	Formula	Justification	Key citations
NDVI	Normalized Difference Vegetation Index	$\frac{NIR - Red}{NIR + Red}$	NDVI is the most commonly used vegetation index for ecological studies. It correlates with vegetation greenness.	(Tucker 1979, Pettorelli et al. 2005)
EVI	Enhanced Vegetation Index	$2.5 * \frac{NIR - Red}{NIR + 6 * Red - 7.5 * Blue + L}$	Corrects NDVI for both soil and atmospheric effects, more sensitive to changes in areas of high biomass	(Huete et al. 1994, 1997, 2002)
SAVI	Soil Adjusted Vegetation Index	$(1 + L) * \frac{NIR - Red}{NIR + Red + L}$	Improves sensitivity of NDVI by including a soil adjustment term, L.	(Huete 1988)

NDMI	Normalized Difference Moisture Index	$\frac{NIR - SWIR}{NIR + SWIR}$	Correlates with plant water content, widely used to detect disturbances in vegetated systems	(Gao 1996, Wilson and Sader 2002)
NDWBI	Normalized Difference Water Body Index	$\frac{Green - NIR}{Green + NIR}$	Highlights water. Commonly used to delineate open water features	(McFeeters 1996)
NDSI	Normalized Difference Soil Index	$\frac{SWIR2 - Green}{SWIR2 + Green}$	Correlates with plant water content, sensitive to drought. Also used to highlight changes in soil composition.	(Ji et al. 2009, Chakraborty and Sehgal 2010, Deng et al. 2015)
NBR	Normalized Burn Ratio	$\frac{SWIR2 - NIR}{SWIR2 + NIR}$	Sensitive to changes to vegetation and soil moisture induced by fire	(Key and Benson 2005)
TCW	Tasseled Cap Wetness	$0.2626 * Blue + 0.2141 * Green + 0.0926 * Red + 0.0656 * NIR - 0.7629 * SWIR - 0.5388 * SWIR2$	Correlates with vegetation moisture content and soil moisture	(Kauth and Thomas 1976, Crist 1985)
TCG	Tasseled Cap Greenness	$-0.3344 * Blue + -0.3544 * Green + -0.4556 * Red + 0.6966 * NIR - 0.0242 * SWIR - 0.2630 * SWIR2$	Correlates with vegetation density and greenness	(Kauth and Thomas 1976)
TCB	Tasseled Cap Brightness	$0.3561 * Blue + 0.3972 * Green + 0.3904 * Red + 0.6966 * NIR + 0.2286 * SWIR + 0.1596 * SWIR2$	Correlates with soil moisture and brightness	(Kauth and Thomas 1976)
TC_Fused	TC combination band	TCG + TCB + TCW	Combination index attempting to describe most of the spectral variation of an image	(Cohen et al. 2018)
NDVINBR	NDVI fused with NBR	NDVI + NBR	Combination index designed to leverage the sensitivity of NIR to changes in vegetation condition	(Kennedy et al. 2018)
NVWI	NDVI fused with NDMI	NDVI + NDMI	Combination aimed at describing variation in vegetation moisture content and greenness	(Kennedy et al. 2018)
NVWBI	NDVI fused with NDWBI	NDVI + NDWBI	Index designed to capture vegetation greenness and open water presence	(Kennedy et al. 2018)

### Disturbance detection algorithm

Changes in vegetation dynamics can be described on 3 scales: 1) interannual changes in seasonal phenology (e.g., those due to subtle changes in annual rainfall and climate fluctuations), 2) gradual temporal trends (e.g., declines in greenness as marshes senesce), and 3) abrupt change (e.g., disturbances). To accurately detect abrupt changes associated with disturbance in a timeseries, one must account for these first two sources of variation. We used the Breaks For Additive Seasonal and Trend (BFAST) algorithm to detect changes in marsh condition associated with wetland disturbances (Verbesselt et al. 2010b, a). BFAST decomposes a timeseries into 3 components: 1) a seasonal (harmonic) model, 2) a trend model, and 3) a remainder (residual) component (Verbesselt et al. 2010a). After decomposition, the algorithm uses an ordinary least-squares moving sum approach to test for significant “breaks” (i.e., changes in slope and intercept) in the trend component of the model. If breaks in the trend component are detected, the algorithm repeatedly decomposes the timeseries and estimates the location and size of the breaks until agreement on the location and size of breaks between iterations is achieved. Hence, the algorithm provides a robust approach to objectively and systematically estimate the timing and size of changes (both abrupt and gradual) in a timeseries. The general form of the timeseries model is:

$$Y_t = T_t + S_t + e_t \quad (t = 1, \dots, n),$$

where  $Y_t$  is the observed data at time  $t$ ,  $T_t$  is the trend component at time  $t$ ,  $S_t$  is the seasonal component at time  $t$ , and  $e_t$  is the remaining variation beyond that which is described by the trend and seasonal components.

The trend component is built of  $m + 1$  linear segments where  $m$  is the number of breaks. Each segment is described with a specific intercept,  $\alpha_i$ , and slope,  $\beta_i$ , where  $i = 1, \dots, m$ . The magnitude and direction of abrupt changes in the trend component can be calculated from the segment-specific intercepts and slopes. The seasonal component is described by a first order harmonic model that estimates the phase (i.e., timing of cycles) and amplitude (i.e., size of change) of seasonal phenology (Fig. 6).

The BFAST algorithm has been used to detect disturbance in temperate forests (Verbesselt et al. 2010a, Schultz et al. 2016), tropical forests (DeVries et al. 2015b) and arid environments (Watts and Laffan 2014, Hutchinson et al. 2015). However, this is one of the first studies to assess whether BFAST can be used to detect vegetation disturbances in wetland systems (also see Wei et al. 2017).

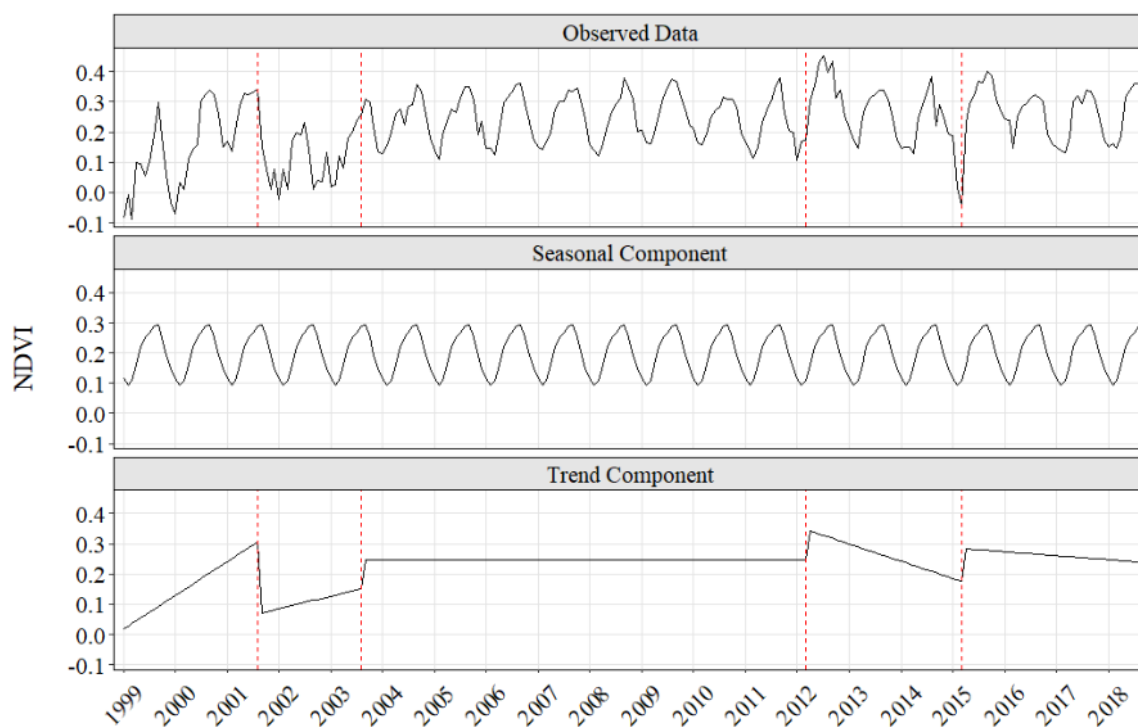


Figure 6. Example of BFAST decomposition of an NDVI timeseries. Top panel represents the observed timeseries, the second panel represents the fitted seasonal model, and the bottom panel shows the fitted trend line. Dotted red lines represent estimated breaks (i.e., changes) in the slope and intercept of the trend line. Changes in slope and intercept between trend segments can be used to estimate the magnitude of abrupt changes.

### Detecting wetland disturbance

We applied the BFAST algorithm to 308 timeseries (22 disturbance footprints  $\times$  14 candidate indices) to evaluate our ability to detect changes in wetland condition associated with management actions. The BFAST algorithm includes 95% confidence intervals around breaks in the trend component and wide confidence intervals suggest considerable uncertainty around the detected break. We considered confidence intervals  $>5$  months as too large to be certain that the corresponding reference disturbance caused the break. We therefore ignored all estimated breaks associated with confidence intervals  $>5$  months. We assessed the accuracy of each index-specific BFAST algorithm by comparing the timing of the estimated breaks (those with confidence intervals  $\leq 5$  months) with

reference disturbances (e.g., prescribed fires) in the marsh parcels. We considered a break to be accurate if the 95% confidence intervals overlapped the true date of an actual disturbance.

We ranked indices by omission error rates (i.e., failure to detect known disturbances) instead of commission error rates (i.e., detected breaks that did not correspond with known disturbances) because we did not always have complete disturbance histories for each marsh parcel. Indeed, commission errors may correspond with subtle changes in marsh phenology brought on by climatic conditions or small-scale management actions that were not reported.

For each break that corresponded with a known disturbance we extracted the magnitude of change (separately for each index). We calculated the magnitude of change by differencing the trend segment before and after each break. We used the magnitude of change for each index to help characterize the change in marsh condition wrought by management actions.

#### Range-wide approach

We considered indices with omission rates  $< 0.5$  (i.e., those indices that detected more than 50% of the reference disturbances) for a range-wide disturbance detection exercise. We applied the BFAST algorithm to Landsat timeseries extracted for all marsh bird survey points to document significant changes in marsh condition. We used a suite of indices to increase the likelihood of detecting significant changes in marsh condition and to provide a mechanism to filter out spuriously detected changes or disturbances. We filtered all estimated breaks with a two-step process:

- 1) We removed all breaks with confidence intervals  $> 5$  months.
- 2) We applied a magnitude threshold to filter out spurious breaks. We calculated the smallest magnitude of change associated with a reference disturbance for each index and used this value as a filtering threshold. That is, we ignored all breaks with a change magnitude smaller than the minimum change associated with the reference disturbances.

Finally, we merged BFAST outputs from all indices to create a single disturbance history for each study location. Index-specific BFAST algorithms often estimated breaks at similar, but not equal, times and we considered all breaks detected within 5 months of each other to represent the same disturbance or change in marsh condition. As such, we created 20-year disturbance histories for each marsh bird survey point.

## RESULTS

### Modeling Yuma Ridgway's rail relative abundance

Average Yuma Ridgway's rail counts reflected the rarity of this endangered species. Across all years and surveys, the average number of rails detected during a survey at a given point ranged from 0.20 rails at the Lower Gila River to 1.92 rails at the S.B. Salton Sea National Wildlife Refuge (Figs. 7 and 8). Moreover, the proportion of observed zero counts during all surveys ranged from 0.87 at the Lower Gila River to 0.40 at the S.B. Salton Sea National Wildlife Refuge (Fig. 9).

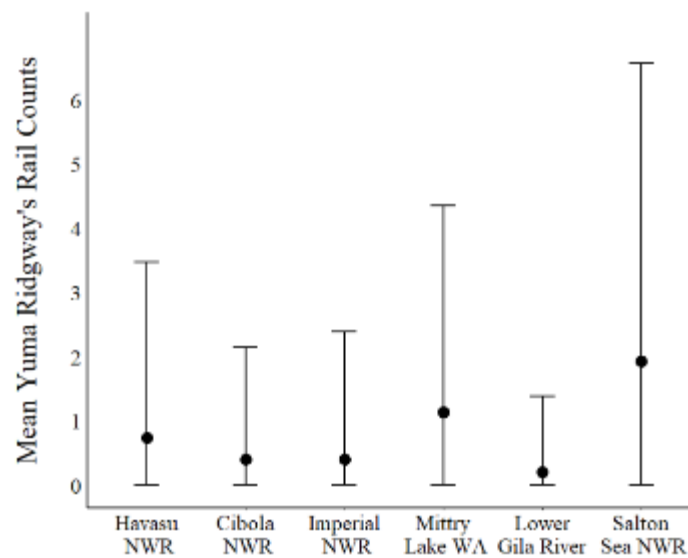


Figure 7. Mean Yuma Ridgway's rail counts for all surveys conducted within each location during 2006-2018. NWR = National Wildlife Refuge and WA = Wildlife Area.

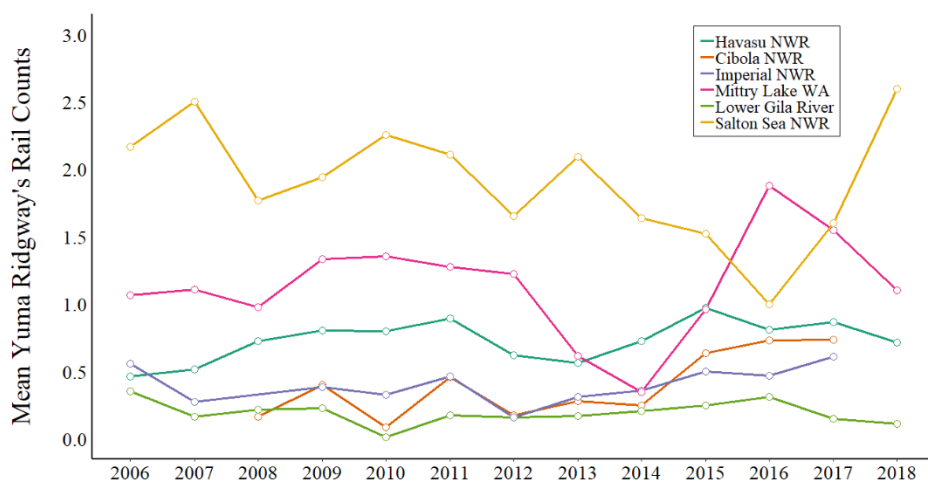


Figure 8. Temporal trends of mean Yuma Ridgway's rail counts for each of the 6 study locations. Means were calculated for all points and surveys within a given region. NWR = National Wildlife Refuge and WA = Wildlife Area.

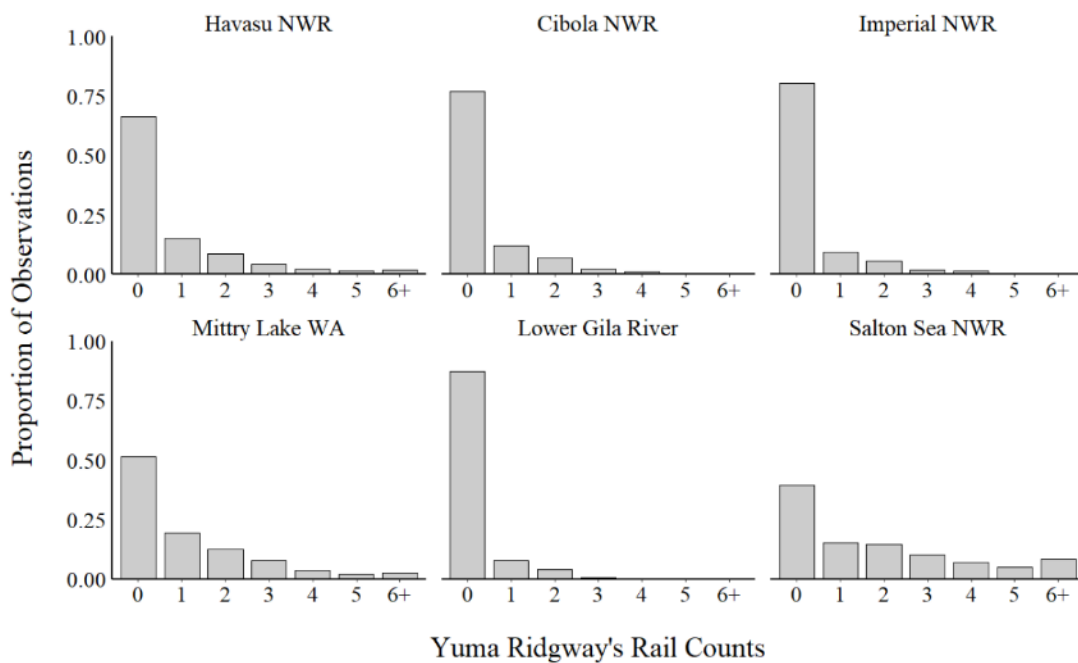


Figure 9. Distribution of Yuma Ridgway's rail counts at each of 6 locations for all surveys conducted from 2006-2018. NWR = National Wildlife Refuge and WA = Wildlife Area.

### Statistical modeling

#### *Covariate reduction to create a global fixed-effects model set*

Yuma Ridgway's rail counts were influenced by both the time and date of surveys and the top model included linear and quadratic effects for date of survey, time of survey, as well as the 2-way interactions (Table A.1). In addition to the detectability covariates, we selected 12 candidate marsh condition covariates through the multi-step covariate reduction process (Table A.17, see Appendix A for extended modeling results).

#### *Identify appropriate statistical distribution*

The fully parameterized NB1 (i.e., a zero-inflated negative binomial distribution with a linear mean-variance relationship) was the most supported distribution in our model selection exercises (Table 6). Zero-inflation probability showed a strong location (spatial) effect and location-specific annual variation. The Lower Gila River had the highest zero-inflation probability, whereas Havasu National Wildlife Refuge, Mittry Lake Wildlife Area and S.B. Salton Sea National Wildlife Refuge had the lowest zero-inflation probability though this varied annually (Table 7, Fig. A.2). Furthermore, the dispersion parameter increased quadratically with survey date at all locations, and thus the data became more overdispersed as the breeding season progressed (Fig. A.3).

Table 6. A truncated list of model structures considered for our analyses. An x indicates the inclusion of an attribute in the structure of the final model. The top model included zero-inflation (with fixed and random effects in the zero-inflation model), a quadratic relationship between the dispersion parameter and survey date, and the full set of random effects considered in the expected count component of the model. Only the top 2 models were competitive, but more models are included for illustrative purposes. Dist refers to the underlying distribution. NB1 = negative binomial, where  $Var = \mu(1 + \theta)$ , NB2 = negative binomial where  $Var = \mu(1 + \mu/\theta)$ , Pois = Poisson where  $Var = \mu$ , and  $\theta$  is the dispersion parameter.

Dist	Dispersion		Zero-inflation		Random effects				Delta AIC	df
	Date	Date <sup>2</sup>	Location	Location annual intercept	Route intercept	Route-annual intercept	Broad-scale annual intercept	Route-time slope		
NB1	x	x	x	x	x	x	x	x	0	42
NB1	x		x	x	x	x	x	x	1.17	41
NB1			x	x	x	x	x	x	12.85	40
NB1	x	x	x	x	x	x	x		12.91	41
NB2	x	x	x	x	x	x	x	x	144.04	42
Pois			x	x	x	x	x	x	321.20	40

Table 7. Estimated zero-inflation probability for each of 6 locations (estimates do not include annual variation). NWR = National Wildlife Refuge.

Location	Zero-inflation probability
Lower Colorado River	
Havasu NWR	0.05
Cibola NWR	0.20
Imperial NWR	0.41
Mittry Lake Wildlife Area	0.08
Outside Lower Colorado River	
Lower Gila River	0.48
S.B. Salton Sea NWR	0.06

*Identify appropriate random effects structure*

The random effects structure included in our top model reflected spatio-temporal variation in rail abundance and detection relationships, and contained 1) a random spatial intercept by route; 2) a random intercept for year, indicating population-wide fluctuations in rail numbers across years; 3) a random intercept for route-specific annual effects, suggesting that counts varied annually with local-scale variation at the route-level (in addition to broad-scale population fluctuations); and 4) a random temporal trend for each route, suggesting that temporal trends in expected rail counts varied among routes (Table 6, Fig. 10).

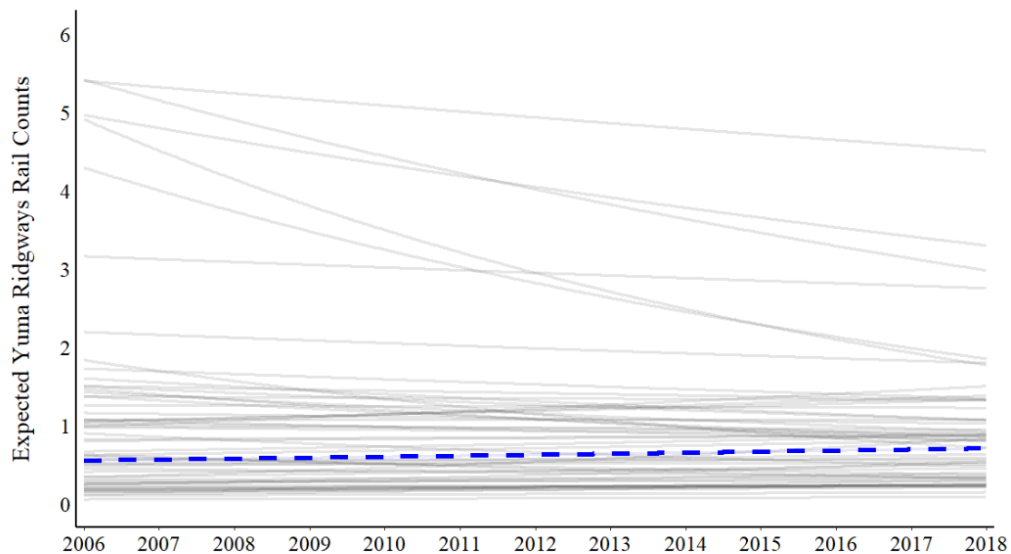


Figure 10. Temporal trends in expected Yuma Ridgway's rail counts. Blue dashed line represents the population-level average temporal trend in expected counts, and light grey lines represent route specific temporal trends.

### Model performance

Model predictions to the observed counts produced good fit across all sites and years (Fig. 11). The model under-predicted 0's and over-predicted 1's at all study locations except the Lower Gila River, but the differences were subtle at most sites (Fig. 11).

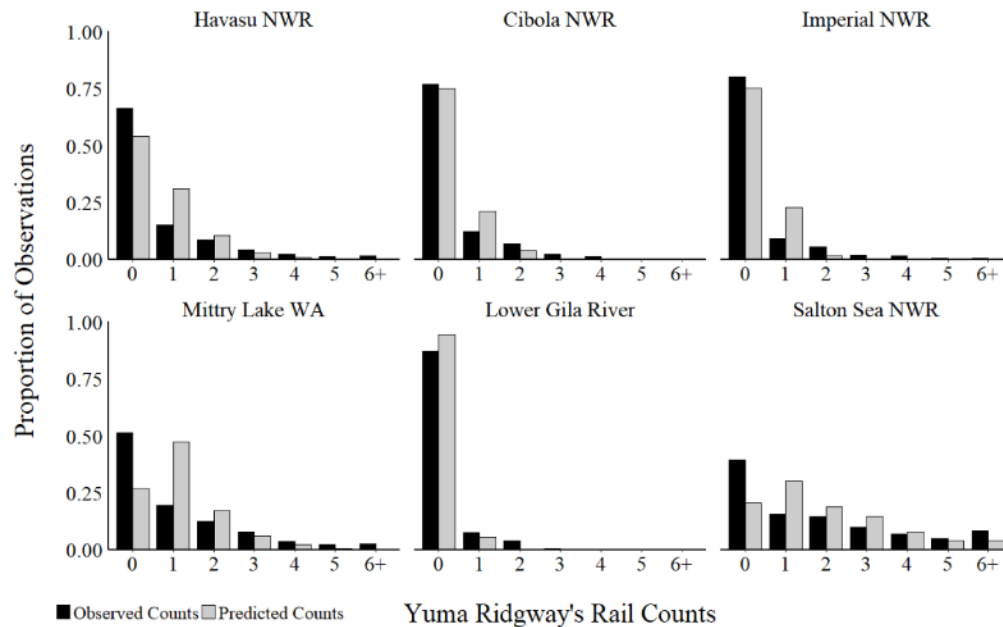


Figure 11. Location-specific predicted and observed Yuma Ridgway's rail counts for all years. NWR= National Wildlife Area and WA = Wildlife Area.

Global root mean squared error (RMSE) was 1.18, indicating that the top model over or under-predicted the number of rails by an average of 1.18 individuals. However, prediction accuracy varied across locations and RMSE was lowest at Lower Gila River and highest at the S.B. Salton Sea National Wildlife Refuge (Table 8).

Table 8. Root Mean Squared Error of the top model calculated for each study location. NWR = National Wildlife Area and WA = Wildlife Area.

Havasu NWR	Cibola NWR	Imperial NWR	Mittry Lake WA	Lower Gila River	S.B. Salton Sea NWR
1.05	0.77	0.88	1.33	0.58	1.86

### Final marsh condition covariates

Relative abundance of Yuma Ridgway's rails (as measured by expected counts) was associated with vegetation moisture covariates; 3 of the 6 final marsh condition covariates reflected

measures of vegetation moisture content. Relative abundance of Yuma Ridgway's rails was also associated with measures of vegetation greenness, but those relationships were weaker. Accumulated greenness (5-year) was the only measure of vegetation greenness to appear in the top model and it showed a weaker correlation than the other 5 marsh condition covariates (Table 9). Finally, relative rail abundance was influenced by marsh condition covariates measured at multiple temporal scales, including the current breeding season, the prior year, as well as a 5-year accumulated marsh condition metric.

Quadratic relationships best described associations between relative rail abundance and the amount of change in vegetation moisture content during the current breeding season, the amount of change in marsh condition (measured with the fused index) during the previous year, and the proportion of vegetation within 224 m of the survey point (Table 9; Fig. 12). Relative rail abundance was highest when 65-85% of the buffer area was vegetated and decreased above and below that range. Finally, relative rail abundance was negatively correlated with minimum vegetation moisture content during the breeding season and 5-year accumulated vegetation moisture content (Table 9; Fig. 12)

Table 9. Standardized parameter estimates from the top model. Covariates are grouped as "Detectability Covariates" and "Marsh Condition Covariates". Bold text indicates parameter estimate with a 95% confidence interval that does not overlap 0. NVMI = the fused index (NDVI+NDMI). Year is continuous variable included to incorporate route-specific temporal trends (random slopes).

Parameter	Mean	SE
Intercept	<b>-0.465</b>	0.142
Detectability Covariates		
Time of Survey	<b>-0.673</b>	0.035
Time of Survey <sup>2</sup>	<b>0.108</b>	0.009
Survey Date	<b>0.101</b>	0.016
Survey Date <sup>2</sup>	-0.024	0.014
Time of Survey : Survey Date	<b>0.125</b>	0.025
Survey Date <sup>2</sup> : Time of Survey <sup>2</sup>	<b>-0.031</b>	0.010
Survey Date : Time of Survey <sup>2</sup>	0.0002	0.010
Time of Survey : Survey Date <sup>2</sup>	0.038	0.022
Marsh Condition Covariates		
min NDMI-breeding	<b>-0.067</b>	0.032
5-y Accumulated NDMI	<b>-0.304</b>	0.033
5-y Accumulated TCG	0.045	0.025
deltaNDMI-breeding	<b>0.164</b>	0.032
deltaNDMI <sup>2</sup> -breeding	<b>-0.052</b>	0.015
deltaNVMI-previous year	<b>0.203</b>	0.028
deltaNVMI <sup>2</sup> -previous year	<b>-0.079</b>	0.016
Proportion Vegetated	<b>0.099</b>	0.024
Proportion Vegetated <sup>2</sup>	<b>-0.149</b>	0.019
Year	0.074	0.054

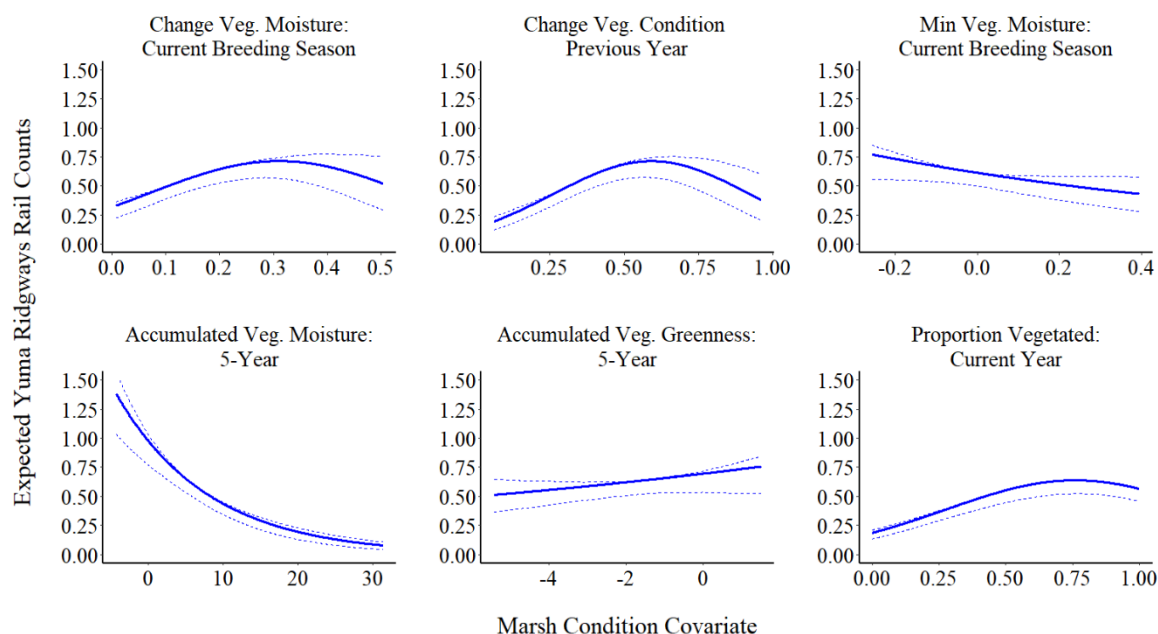


Figure 12. Expected counts of Yuma Ridgway's rails as a function of 6 marsh condition covariates in the top model. Dashed lines represent 95% confidence intervals.

### Index performance

We sought to identify spectral indices best suited to predict variation in relative rail abundance, and thus measure rail habitat suitability. NDMI outperformed TCW (both are measures of vegetation moisture content) as predictors of rail counts in our models. In our covariate reduction exercise, NDMI covariates frequently showed lower AIC scores than analogous TCW covariates and no covariates derived from TCW remained in the top model (Table 9; and Tables A.2-A.16).

Among the measures of greenness that we assessed, NDVI and TCG were equally good predictors of rail counts based on our covariate reduction exercises. Greenness covariates based on both NDVI and TCG appeared in our initial set of 12 candidate marsh condition variables, but only 5-year accumulated greenness (measured by TCG) remained in the top model. Covariates measured with NVMI (i.e., the fused index designed to capture variation in both vegetation greenness and moisture content) was also a good predictor of rail counts based on the covariate reduction exercises. NVMI covariates consistently performed better than greenness covariates, but worse than moisture covariates (Tables A.2-A.16).

## Wetland disturbance detection

We detected 82% (23 of 28) of the reference disturbances with BFAST algorithms. Moreover, we accurately identified 80 % (20 of 25) of the reference management actions and 67% (2 of 3) of the reference wildfires. The BFAST algorithm failed to detect 1 wildfire at Mittry Lake Wildlife Area, 1 prescribed wetland fire at S.B. Salton Sea National Wildlife Refuge, and 3 prescribed wetland fires at Imperial National Wildlife Refuge. NBR had lowest omission rates of any individual index, followed by 2 vegetation moisture indices, NDMI and NDSI (Table 10). Vegetation greenness indices (TCG, EVI, NDVI, and SAVI) performed poorly. Finally, 75% (3 of 4) of the composite indices performed worse than the individual indices from which they were built. Only NVWBI performed better than the indices from which it was built (NDWBI and NDVI). The BFAST algorithm detected no more than 71% of the known disturbances when fit to a single index, but we reduced omission error rates by merging outputs from BFAST algorithms fit to multiple spectral indices. We achieved a maximum accuracy by merging BFAST outputs from NBR and TCW (Table 11).

Table 10. Performance of BFAST algorithms fit with different spectral indices. Disturbances detected refers to the number of the 28 reference disturbances detected by the index-specific BFAST algorithm. Accuracy was calculated by dividing the number of detected disturbances by the total number of reference disturbances (n=28). Mean and median C.I.s indicate the precision with which indices detected disturbances.

Index	Disturbances Detected	Omission Rate	Mean C.I.	Median C.I.
NBR	20	0.29	3.25	3
NDMI	19	0.32	2.53	2
NDSI	18	0.36	2.72	2.5
NVMI	18	0.36	2.94	3
NDVINBR	17	0.39	3.12	3
TCW	17	0.43	2.38	2
TC_Fused	14	0.5	2.71	2
TCB	11	0.61	3.27	3
TCG	11	0.61	3.27	3
NVWBI	10	0.64	3.00	3
EVI	5	0.82	3.80	3
NDWBI	5	0.82	3.40	3
NDVI	4	0.86	3.00	2.5
SAVI	2	0.93	4.00	4

Table 11. Best performing index sets. We minimized omission error rates by merging BFAST outputs from TCW and NBR spectral indices.

Index set	Number of detected disturbances	Omission rate
NBR	20	0.29
NBR, NDSI	22	0.23
NBR, NDMI	22	0.23
NBR, TCW	23	0.18

Breaks associated with reference disturbances generally had greater change magnitudes than those breaks not associated with any known disturbances (Fig. 13). Moreover, the change magnitude associated with known disturbances tended to be strictly negative or positive (depending on the index), whereas those changes not associated with known disturbances showed both positive and negative change magnitudes.

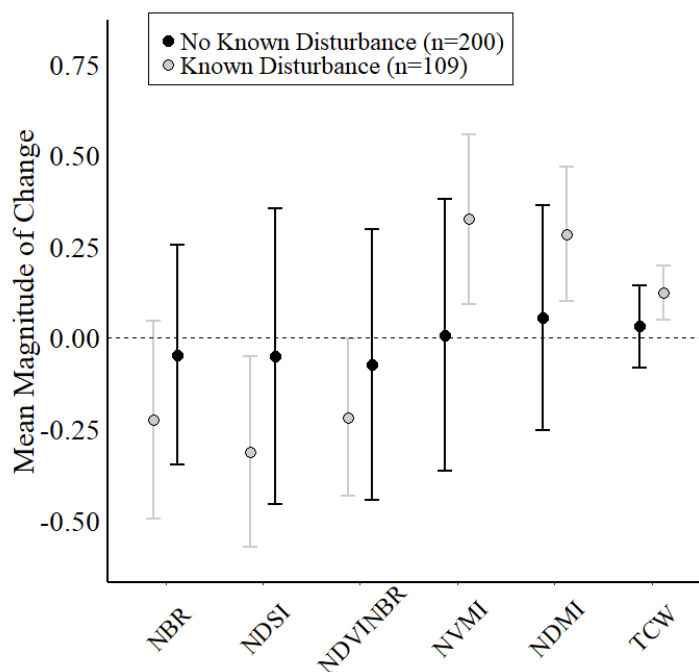


Figure 13. Average change magnitudes of BFAST breaks associated with reference disturbances (grey) and not associated with any known disturbances (black). Only the 6 best indices are shown here. Disturbances were associated with negative changes in the left 3 indices, and positive changes in the right 3 indices. Points represent means and error bars show 95% confidence intervals.

We considered all indices with omission rates  $<0.50$  in our range-wide disturbance detection exercises. We applied the BFAST algorithm to timeseries for each of these “good” spectral indices for each survey point and filtered out all detected breaks below the magnitude threshold as well as those with confidence intervals  $>5$  months. After break filtering, we detected  $1.93 \pm 0.06$  (range 0-8) breaks with change magnitudes at least as great as those change magnitudes produced by the reference disturbances at each survey point during the previous 20 years (Fig. 14).

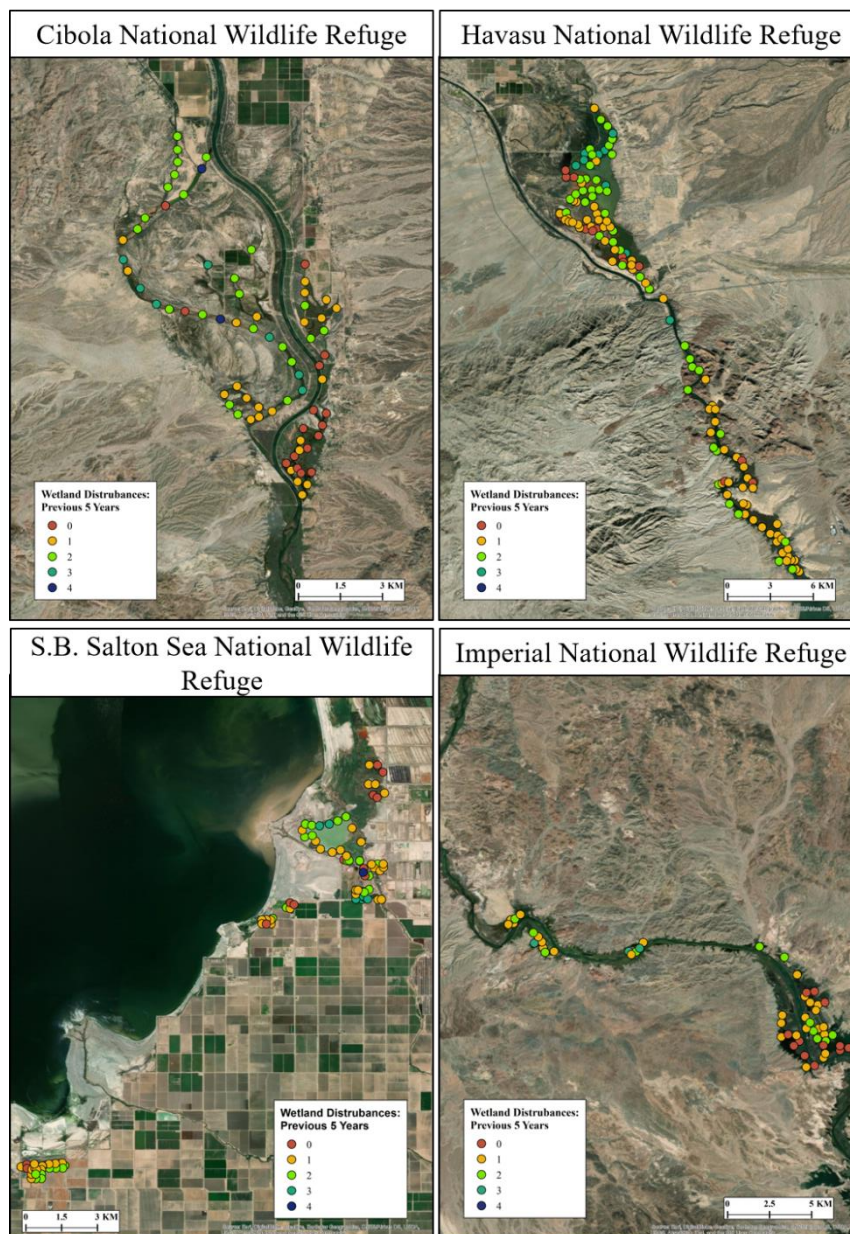


Figure 14. Maps showing the number of significant breaks detected with the BFAST algorithm at survey points within 4 study locations during the previous 5 years.

## DISCUSSION

### Modeling relative abundance of Yuma Ridgway's rails

We linked Landsat-derived metrics of marsh condition with the relative abundance of Yuma Ridgway's rails while accounting for the spatio-temporal dynamics of a fragmented and stochastic emergent marsh ecosystem. By doing so, we created a powerful method to efficiently document habitat suitability of the endangered rail at fine-scale resolution and broad spatial extent (i.e., the entire U.S. range of the species). Moreover, the products of our modeling efforts can provide a useful tool to guide management decisions and facilitate the allocation of resources towards effective conservation.

We generated range-wide predictive maps of habitat suitability at a fine spatial grain (30 m resolution; Fig. 15). Such maps can help spatially and temporally target management actions throughout the range of this endangered bird. Indeed, marshes predicted by our models to have relatively low rail abundance that were predicted to have high rail abundance in prior years may be best suited for management actions. The predictive maps also illuminate the status of Yuma Ridgway's rail habitat throughout their range and may highlight opportunities for habitat acquisition or future restoration efforts.

The predictive maps suggest that much of the most suitable rail habitat is already protected. Indeed, 70.5% of all wetland areas in the 85<sup>th</sup> percentile of predicted habitat suitability falls on lands currently managed as National Wildlife Refuges or Wildlife Areas. Moreover, 59.1% of all the wetland areas in the 15<sup>th</sup> percentile of predicted habitat suitability (i.e., lowest quality habitat) falls on unmanaged or private lands. These results highlight several important points: 1) national wildlife refuges are stewards of majority of high-quality habitat for Yuma Ridgway's rails in the U.S.; 2) nearly 30% of the best habitat (as predicted by our models) is currently unprotected or unmanaged and these wetlands may be excellent targets for future land acquisitions; and 3) roughly 40% of the least suitable rail habitat falls on managed lands and these wetlands may present opportunities for management or restoration actions to improve rail habitat to help delist or down-list the species.

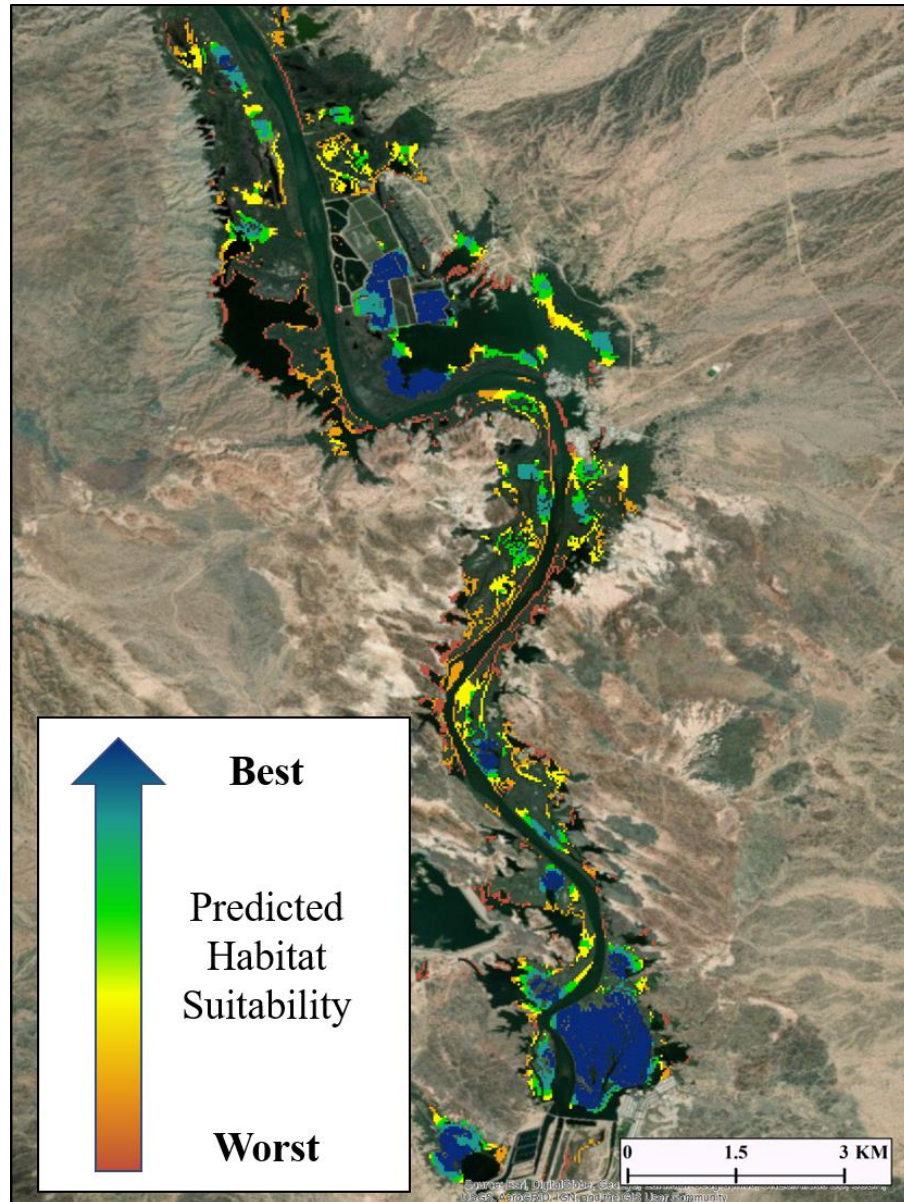


Figure 15. Map of predicted habitat suitability along the Lower Colorado River near Imperial National Wildlife Refuge.

Importantly, these predictive maps provide a mechanism to monitor changes in relative habitat suitability throughout the range of the Yuma Ridgway's rail. We can use the maps of predicted habitat suitability to assess how habitat conditions change through time and throughout the species range, and how habitat suitability changes in response to the application of management actions. For example, we can assess how relative habitat suitability changed at Imperial National Wildlife Refuge in response to

prescribed wetland fire (Fig. 16). Further, we can update these maps in future years to continually assess changes in habitat suitability, thereby identifying areas for targeted restoration.

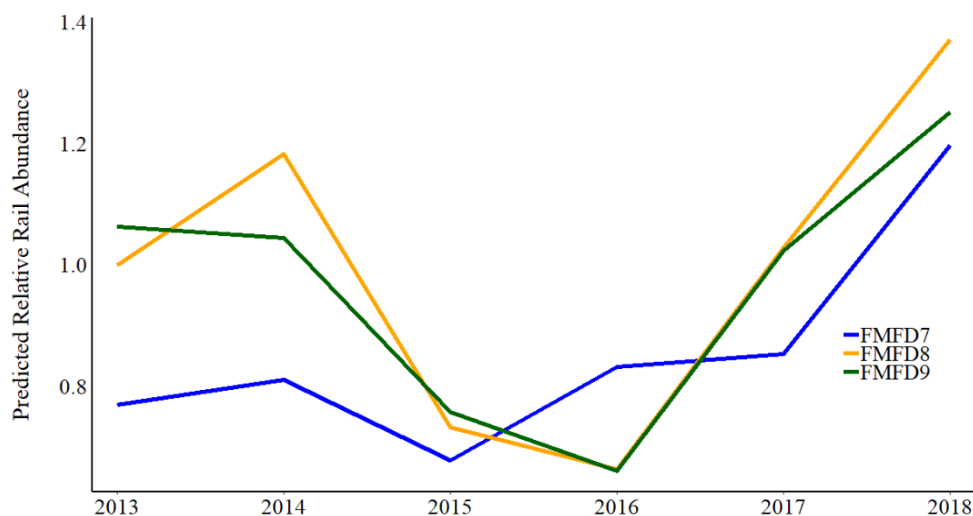


Figure 16. Average predicted relative abundance of Yuma Ridgway's rails in three managed marsh parcels within Imperial National Wildlife Refuge. All 3 managed units (represented by line colors) were burned in February 2015 and showed an increase in predicted relative rail abundance soon after the burn.

We built the predictive maps on Google Earth Engine and this presents a powerful opportunity to make these maps accessible to managers and policy-makers. The maps are shareable, interactive, and do not require access to expensive software. Indeed, one needs only an internet connection to access these maps of rail habitat suitability, making them useful tools for managers to assess habitat suitability for regions and time-frames of interest. Furthermore, these maps will be easy to update in future years, thereby facilitating: 1) effective habitat monitoring, 2) identification of marshes for restoration efforts, and 3) rapid assessment of the effects of restoration efforts through time.

We identified several important marsh condition relationships for Yuma Ridgway's rails. Relative rail abundance was positively correlated with the seasonality of marsh vegetation during year<sub>t</sub> and year<sub>t-1</sub>. We measured seasonality as the amount of change in marsh condition during a given time window (breeding season or full year). Seasonality of marsh vegetation is likely affected by vegetation structure and composition and may thus affect rail abundance through a variety of mechanisms. First, non-native phragmites (*Phragmites australis*) readily encroaches emergent wetlands, creates dense monotypic stands, and generally creates poor rail habitat (Eddleman 1989, Eddleman and Conway 1994). Importantly, phragmites remains green through the winter, whereas many emergent vegetation

species associated with high-quality rail habitat go dormant (turn brown) in the winter (Mexicano et al. 2012). Thus, marshes with abundant phragmites may show increased winter vegetation greenness and moisture content (compared to early successional emergent marshes) and exhibit smaller seasonal fluctuations.

Second, Yuma Ridgway's rails prefer marshes interspersed with shallow open water pools and moderate vegetation densities (Conway et al. 1993). Water and saturated soils will likely be more exposed in such early successional marshes than in dense marshes filled with decadent vegetation. Water absorbs light at a wide range of wavelengths, and thus exposed water in early successional marshes may have a greater impact on spectral indices (water will depress values). Dense marsh vegetation and decadent marsh vegetation likely mask the effects of water and result in smaller seasonal fluctuations in spectral indices. We hypothesized this relationship may be quadratic because of the possible effects of marsh disturbance. Disturbances that clear marsh vegetation may result in extremely low spectral values and thus result in large differences between minimum and maximum seasonal index values. As such, large seasonal changes may indicate disturbances and rail abundance may not increase until the marsh vegetation has rebounded (6 months – 1 year after wetland fire; Conway et al. 2010).

Relative Yuma Ridgway's rail abundance was negatively correlated with 5-year accumulated vegetation moisture content and minimum vegetation moisture content during the breeding season. Both negative relationships may be explained by the same mechanisms describing the relationship between rail abundance and marsh vegetation seasonality. Dense marsh vegetation, the accumulation of decadent vegetation, and the encroachment of phragmites and woody vegetation (i.e., processes that degrade rail habitat quality) may inflate winter vegetation moisture values and thus indicate poor habitat suitability for Yuma Ridgway's rails.

Yuma Ridgway's rails prefer emergent marsh vegetation interspersed with open water or mudflats and this likely explains the positive quadratic relationship we observed between rail abundance and the proportion of vegetation within a 224-m buffer of survey points. This result corroborates prior local habitat studies and species accounts which have noted that rails prefer these same habitat conditions (Conway 1990, 1995, Eddleman and Conway 1994, 2018). Yuma Ridgway's rail home ranges averaged 7.22 ha during the breeding season (Conway et al. 1993) and the 224-m buffers cover 15.78 ha. As such, fully vegetated buffers may present poorer habitat than buffers

interspersed with water or mudflats. Indeed, relative rail abundance decreased at survey points with  $\geq 75\%$  vegetation in the 224-m buffer surrounding the point.

We identified spectral indices well suited to predict relative abundance of Yuma Ridgway's rails and monitor rail habitat suitability. Measures of vegetation moisture content outperformed (i.e., resulted in better model fit) measures of vegetation greenness. Importantly, NDVI performed poorly in relative rail abundance modeling (NDVI-based metrics were not in any of the top rail abundance models). NDVI is arguably the most widely used spectral index for vegetation monitoring, but our results suggest that other spectral indices may be better than NDVI. A myriad of spectral indices exists and studies that identify the index most appropriate to their study objectives (as we did here) will likely improve predictive accuracy of models.

We used a generalized linear regression approach because it provided a flexible modeling framework to investigate the effects of marsh conditions on rails. We accounted for variable survey-level detection probabilities by including "nuisance" detectability covariates directly in the conditional model (i.e., fixed-effects on the condition mean). Failing to account for spatial and temporal variation in detection probability has been a criticism of many past ecological studies (Fiske and Chandler 2011, Barker et al. 2018). Numerous sampling approaches exist to estimate detection probability so that investigators can link observed counts to true abundance; however, these approaches require collecting auxiliary data in the field (e.g., mark-recapture methods, distance sampling, or double observer sampling). Absent such auxiliary data, N-mixture models (Royle 2004) are a popular approach to estimate abundance in the face of imperfect detection because they simultaneously estimate abundance ( $N$ ) and detection probability ( $p$ ). To make such estimates, N-mixture models rely on several restrictive assumptions (e.g., constant  $p$ , animals were not double counted, and populations remained closed during survey periods) and N-mixture models are very sensitive to violations of these assumptions (Barker et al. 2018, Link et al. 2018). We could not separately estimate  $N$  and  $p$  with generalized linear regression (as is possible with N-mixture models), therefore we could make inferences only about relative rail abundance (instead of true abundance). However, generalized linear regression provides a powerful and flexible framework to evaluate processes affecting relative abundance (Sauer and Link 2011, Barker et al. 2018).

#### Wetland disturbance detection

Detecting abrupt vegetation changes in wetland systems is particularly challenging because of the heterogeneity of many wetland systems and their dynamic water levels (Dahl 2006, Guo et al.

2017, Wei et al. 2017). We demonstrated that applying the BFAST algorithm to temporally dense Landsat timeseries is a robust way to detect wetland disturbances, despite the inherent heterogeneity of emergent wetlands. Moreover, we reduced omission rates by fitting BFAST algorithms to multiple spectral indices and merging the outputs. Such ensemble approaches have been effective for detecting disturbances in temperate and tropical forests (Schultz et al. 2016, Cohen et al. 2018, Healey et al. 2018), but we are unaware of previous studies that have done so in wetlands.

The BFAST algorithm detected 82% (23 of 28) of known wetland disturbances. The 5 omissions (4 prescribed fires and 1 natural fire) may have resulted from low fire intensities. Magnitude of disturbance influences the ability to detect the signal of a disturbance (i.e., a change in the imagery) through the noise of the timeseries (DeVries et al. 2015*b*, Cohen et al. 2018, Healey et al. 2018). Wetland fires do not always burn hotly or cover the full extent of the marsh. As such, low intensity wetland fires may not generate enough disturbance in the vegetation to be detected with precision by the BFAST algorithm. Indeed, if we included imprecise breaks (i.e., breaks with estimated confidence intervals >5 months), we detected 3 of the 5 omitted fires. However, the average estimated confidence intervals around those detections was 14.6 months.

The best performing indices were all derived from the short-wave infrared (SWIR) bands. Our results mirror studies in forested systems where SWIR-based indices were most sensitive to deforestation and forest disturbance (Wilson and Sader 2002, DeVries et al. 2015*a*, Cohen et al. 2018). SWIR bands are sensitive to vegetation moisture content and canopy structure (Baig et al. 2014, Schultz et al. 2016) and they may better reflect changes in marsh condition wrought by disturbances. In our system, the poor performance of greenness indices may be due (in part) to the timing of management actions and the response of marsh vegetation. Most of the known disturbances (25 of 28) occurred during the winter months (management actions typically occur during the winter to minimize impacts on the rail breeding season and avoid times of highest fire intensities) and wetland vegetation regrows quickly after management actions. Indeed, marsh vegetation was abundant within 6 months of management action, and burned marshes were difficult to distinguish visually from unburned marshes after only 2 years (Conway et al. 2010). As such, winter disturbances may not affect the annual cycle of greenness values enough to generate a disturbance signal. That is, low greenness values will still occur in the winter (just lower than normal because of the burned vegetation) and high greenness values will still occur in the summer. Moisture content of vegetation may take longer to recover after wetland disturbance, and thus moisture indices (those derived from SWIR bands) may better detect changes in the structure and density of marsh vegetation after such disturbances.

We ranked indices based on the omission error rate. We did not use commission rates (false positives) because we did not know the full history of the management units in question. Indeed, management actions are not always reported and subtle changes in the irrigation regimes may cause changes in marsh condition which are detected by the BFAST algorithms.

We estimated 1.93 (range 0-8) breakpoints per survey point with change magnitudes  $\geq$  the change magnitudes from the 28 known (reference) disturbances. While most of the estimated breaks did not correspond with known disturbances (e.g., management actions or wildfires), they still reflect significant changes in the condition and phenology of marsh vegetation. Such information can help inform the dynamics and frequency of wetland disturbance throughout the range of Yuma Ridgway's rails. We can use these results to highlight those marshes where disturbances are infrequent and perhaps overdue.

Finally, we applied the BFAST algorithm to spatially (and temporally) averaged spectral index values for each disturbance footprint and survey point buffer. Such an approach facilitated the exploration of different indices, while reducing the computational intensity of the analyses (compared to a pixel-based approach). However, spatially averaging all pixels within the disturbance footprint may mask the signal (i.e., deviations in spectral index values) of a disturbance, especially for low intensity disturbances. A pixel-based change detection approach would be a valuable continuation of this work. We have identified the optimal indices for wetland change detection and our results demonstrate that the BFAST algorithm can be effective, hence we could apply our same disturbance detection techniques at a pixel scale. A pixel-based approach would also allow us to better estimate the spatial accuracy of the BFAST algorithm (Schultz et al. 2016). We could compare the timing and location of "disturbed" pixels to known disturbance footprints to evaluate our ability to estimate the extent as well as timing of wetland disturbances. Such information would greatly facilitate prioritizing management actions throughout the region.

Our work attempts to address some of the challenges facing the spatial and temporal prioritization of habitat management actions. We used publicly available Landsat data to predict relative habitat suitability at a fine spatial grain throughout the U.S. range of an endangered species. Moreover, we developed a reliable way to detect wetland disturbances, which may further help spatially and temporally prioritize management actions. Our work also highlights the importance of identifying appropriate spectral indices to match the study objectives of any research effort. We implemented our predictive maps of relative habitat suitability on the web-based Google Earth Engine

platform, thereby creating an informative and accessible tool for land management agencies. Importantly, by implementing our modeling efforts on Google Earth Engine, our predictive maps may be updated readily to monitor habitat condition through time. Our work focused on the endangered Yuma Ridgway's rails, but our modeling approaches that apply Landsat imagery to elucidate relationships between local species abundance and habitat conditions and predict habitat suitability could readily be applied to other species of conservation concern.

## LITERATURE CITED

- Alatorre, L. C., S. Sánchez-Carrillo, S. Miramontes-Beltrán, R. J. Medina, M. E. Torres-Olave, L. C. Bravo, L. C. Wiebe, A. Granados, D. K. Adams, E. Sánchez, and M. Uc. 2016. Temporal changes of NDVI for qualitative environmental assessment of mangroves: Shrimp farming impact on the health decline of the arid mangroves in the Gulf of California (1990-2010). *Journal of Arid Environments* 125:98–109.
- Baig, M. H. A., L. Zhang, T. Shuai, and Q. Tong. 2014. Derivation of a Tasseled Cap Transformation based on Landsat 8 at-satellite reflectance. *Remote Sensing Letters* 5:423–431.
- Baker, C., R. L. Lawrence, C. Montagne, and D. Patten. 2007. Change detection of wetland ecosystems using Landsat imagery and change vector analysis. *Wetlands* 27:610–619.
- Barker, R. J., M. R. Schofield, W. A. Link, and J. R. Sauer. 2018. On the reliability of N-mixture models for count data. *Biometrics* 74:369–377.
- Barnum, D. A., T. Bradley, M. Cohen, B. Wilcox, and G. Yanega. 2017. State of the Salton Sea—A science and monitoring meeting of scientists for the Salton Sea. U.S. Geological Survey Open-File Report 2017–1005.
- Bottrill, M. C., L. N. Joseph, J. Carwardine, M. Bode, C. Cook, E. T. Game, H. Grantham, S. Kark, S. Linke, E. McDonald-Madden, R. L. Pressey, S. Walker, K. A. Wilson, and H. P. Possingham. 2008. Is conservation triage just smart decision making? *Trends in Ecology and Evolution* 23:649–654.
- Brooks, M. E., K. Kristensen, K. J. van Benthem, A. Magnusson, C. W. Berg, A. Nielsen, H. J. Skaug, M. Mächler, and B. M. Bolker. 2017. glmmTMB balances speed and flexibility among packages for zero-inflated generalized linear mixed modeling. *The R Journal* 9:378–400.
- Carrquiry, J. D., and A. Sánchez. 1999. Sedimentation in the Colorado River delta and Upper Gulf of California after nearly a century of discharge loss. *Marine Geology* 158:125–145.
- Chakraborty, A., and V. K. Sehgal. 2010. Assessment of agricultural drought using MODIS derived Normalized Difference Water Index. *Journal of Agricultural Physics* 10:28–36.
- Christensen, N. S., and D. P. Lettenmaier. 2007. A multimodel ensemble approach to assessment of climate change impacts on the hydrology and water resources of the Colorado River Basin. *Hydrology and Earth System Sciences Discussions* 11:1417–1434.

- Cohen, M. J., C. Henges-Jeck, and G. Castillo-Moreno. 2001. A preliminary water balance for the Colorado River delta, 1992-1998. *Journal of Arid Environments* 49:35–48.
- Cohen, W. B., S. P. Healey, Z. Yang, S. V. Stehman, C. K. Brewer, E. B. Brooks, N. Gorelick, C. Huang, M. J. Hughes, R. E. Kennedy, T. R. Loveland, G. G. Moisen, T. A. Schroeder, J. E. Vogelmann, C. E. Woodcock, L. Yang, and Z. Zhu. 2017. How similar are forest disturbance maps derived from different Landsat time series algorithms? *Forests* 8:1–19.
- Cohen, W. B., Z. Yang, S. P. Healey, R. E. Kennedy, and N. Gorelick. 2018. A LandTrendr multispectral ensemble for forest disturbance detection. *Remote Sensing of Environment* 205:131–140.
- Conway, C. J. 1990. Seasonal changes in movements and habitat use by three sympatric species of rails. Thesis. University of Wyoming, Laramie, Wyoming, USA.
- Conway, C. J. 1995 Virginia rail (*Rallus limicola*). in A. Poole and F. Gill, editors. *The birds of North America*. The Academy of Natural Sciences, Philadelphia, Pennsylvania and The American Ornithologists' Union, Washington, D.C., USA.
- Conway, C. J. 2011. Standardized North American marsh bird monitoring protocol. *Waterbirds* 34:319–346.
- Conway, C. J., W. R. Eddleman, S. H. Anderson, and L. R. Hanebury. 1993. Seasonal changes in Yuma clapper rail vocalization rate and habitat use. *Journal of Wildlife Management* 57:282–290.
- Conway, C. J., and J. P. Gibbs. 2011. Summary of intrinsic and extrinsic factors affecting detection probability of marsh birds. *Wetlands* 31:403–411.
- Conway, C. J., C. P. Nadeau, and L. Piest. 2010. Fire helps restore natural disturbance regime to benefit rare and endangered marsh birds endemic to the Colorado River. *Ecological Applications* 20:2024–2035.
- Cordell, S., E. J. Questad, G. P. Asner, K. M. Kinney, J. M. Thaxton, A. Uowolo, S. Brooks, and M. W. Chynoweth. 2017. Remote sensing for restoration planning: How the big picture can inform stakeholders. *Restoration Ecology* 25:S147–S154.
- Crist, E. P. 1985. A TM Tasseled Cap equivalent transformation for reflectance factor data. *Remote Sensing of Environment* 17:301–306.

- Dahl, T. E. 2006. Remote sensing as a tool for monitoring wetland habitat change. in C. Aguirre-Bravo, P. J. Pellicane, P. D. Burns, and S. Draggan, editors. Monitoring science and technology symposium: Unifying knowledge for sustainability in the Western Hemisphere. Proceedings RMRS-P-42CD. Fort Collins, Colorado: U.S. Department of Agriculture, Forest Service, Rocky Mountain Research Station, Denver, Colorado, USA
- Dahl, T. E. 2011. Status and trends of wetlands in the conterminous United States 2004 to 2009. U.S. Department of the Interior; Fish and Wildlife Service, Washington, D.C., USA.
- Davidson, N. C. 2014. How much wetland has the world lost? Long-term and recent trends in global wetland area. *Marine and Freshwater Research* 65:934–941.
- Deng, Y., C. Wu, M. Li, and R. Chen. 2015. RNDSI: A ratio normalized difference soil index for remote sensing of urban/suburban environments. *International Journal of Applied Earth Observation and Geoinformation* 39:40–48.
- DeVries, B., M. Decuyper, J. Verbesselt, A. Zeileis, M. Herold, and S. Joseph. 2015a. Tracking disturbance-regrowth dynamics in tropical forests using structural change detection and Landsat time series. *Remote Sensing of Environment* 169:320–334.
- DeVries, B., J. Verbesselt, L. Kooistra, and M. Herold. 2015b. Robust monitoring of small-scale forest disturbances in a tropical montane forest using Landsat time series. *Remote Sensing of Environment* 161:107–121.
- Eddleman, W. R. 1989. Biology of the Yuma Clapper Rail in Southwestern U.S. and Northwestern Mexico. Final Report July 1989. Fish and Wildlife Service Contract 4-AA-30-02060.
- Eddleman, W. R., and C. J. Conway. 1994. Clapper Rail. Pages 167–179 in T. C. Tacha and C. E. Braun, editors. Migratory shore and upland game bird management in North America. International Association of Fish and Wildlife Agencies. Washington, D.C., USA
- Eddleman, W. R., and C. J. Conway. 2018. Ridgway's Rail (*Rallus obsoletus*). in P. G. Rodewald, editor. *The Birds of North America Online*.
- Fickas, K. C., W. B. Cohen, and Z. Yang. 2016. Landsat-based monitoring of annual wetland change in the Willamette Valley of Oregon, USA from 1972 to 2012. *Wetlands Ecology and Management* 24:73–92.

- Fiske, I., and R. Chandler. 2011. unmarked: An R package for fitting hierarchical models of wildlife occurrence and abundance. *Journal of Statistical Software* 43:1-23
- Forkel, M., N. Carvalhais, J. Verbesselt, M. D. Mahecha, C. S. R. Neigh, and M. Reichstein. 2013. Trend change detection in NDVI time series: Effects of inter-annual variability and methodology. *Remote Sensing* 5:2113–2144.
- Fornacca, D., G. Ren, and W. Xiao. 2018. Evaluating the best spectral indices for the detection of burn scars at several post-fire dates in a mountainous region of Northwest Yunnan, China. *Remote Sensing* 10:1–21
- Fox, J. 2015. *Applied regression analysis and generalized linear models*. Sage Publications. Thousand Oaks, California, USA.
- Gallant, A. L. 2015. The challenges of remote monitoring of wetlands. *Remote Sensing* 7:10938–10950.
- Gao, B. 1996. NDWI—A normalized difference water index for remote sensing of vegetation liquid water from space. *Remote Sensing of Environment* 58:257–266.
- Geerken, R. A. 2009. An algorithm to classify and monitor seasonal variations in vegetation phenologies and their inter-annual change. *ISPRS Journal of Photogrammetry and Remote Sensing* 64:422–431.
- Geerken, R., B. Zaitchik, and J. P. Evans. 2005. Classifying rangeland vegetation type and coverage from NDVI time series using Fourier Filtered Cycle Similarity. *International Journal of Remote Sensing* 26:5535–5554.
- Gibbs, J. P. 2000. Wetland loss and biodiversity conservation. *Conservation Biology* 14:314–317.
- Glenn, E. P., K. Hucklebridge, O. Hinojosa-Huerta, P. L. Nagler, and J. Pitt. 2008. Reconciling environmental and flood control goals on an arid-zone river: Case study of the Limitrophe region of the Lower Colorado River in the United States and Mexico. *Environmental Management* 41:322–335.
- Glisson, W. J., C. J. Conway, C. P. Nadeau, and K. L. Borgmann. 2017. Habitat models to predict wetland bird occupancy influenced by scale, anthropogenic disturbance, and imperfect detection. *Ecosphere* 8:1-18

- Gomez-Sapiens, M. M. 2014. Linking shorebird and marsh bird habitat use to water management in anthropogenic and natural wetlands in the Colorado River Delta. Dissertation. University of Arizona, Tucson, Arizona, USA.
- Goodwin, N. R., N. C. Coops, M. A. Wulder, S. Gillanders, T. A. Schroeder, and T. Nelson. 2008. Estimation of insect infestation dynamics using a temporal sequence of Landsat data. *Remote Sensing of Environment* 112:3680–3689.
- Gorelick, N., M. Hancher, M. Dixon, S. Ilyushchenko, D. Thau, and R. Moore. 2017. Google Earth Engine: Planetary-scale geospatial analysis for everyone. *Remote Sensing of Environment* 202:18–27.
- Guo, M., J. Li, C. Sheng, J. Xu, and L. Wu. 2017. A review of wetland remote sensing. *Sensors (Switzerland)* 17:1–36.
- Healey, S. P., W. B. Cohen, Z. Yang, C. K. Brewer, E. B. Brooks, N. Gorelick, A. J. Hernandez, C. Huang, M. J. Hughes, R. E. Kennedy, T. R. Loveland, G. G. Moisen, T. A. Schroeder, S. V. Stehman, J. E. Vogelmann, C. E. Woodcock, L. Yang, and Z. Zhu. 2018. Mapping forest change using stacked generalization: An ensemble approach. *Remote Sensing of Environment* 204:717–728.
- Hilbe, J. M. 2011. *Negative Binomial Regression*. Second edition. Cambridge University Press, Cambridge, Massachusetts, USA.
- Hinojosa-Huerta, O., J. J. Rivera-Díaz, H. Iturribarría-Rojas, and A. Calvo-Fonseca. 2008. Population trends of Yuma clapper rails in the Colorado River delta, Mexico. *Studies in Avian Biology* 37:69–73.
- Hislop, S., S. Jones, M. Soto-Berelov, A. Skidmore, A. Haywood, and T. H. Nguyen. 2018. Using Landsat spectral indices in time-series to assess wildfire disturbance and recovery. *Remote Sensing* 10:1–17.
- Holben, B. N. 1986. Characteristics of maximum-value composite images from temporal AVHRR data. *International Journal of Remote Sensing* 7:1417–1434.
- Huang, C., B. Wylie, L. Yang, C. Homer, and G. Zylstra. 2002. Derivation of a Tasseled Cap Transformation Based on Landsat 7 At-Satellite Reflectance.

- Huang, X., Q. Lu, L. Zhang, and A. Plaza. 2014. New postprocessing methods for remote sensing image classification: A systematic study. *IEEE Transactions on Geoscience and Remote Sensing* 52:7140–7159.
- Huckleberry, G. 1994. Contrasting channel response to floods on the middle Gila River, Arizona. *Geology* 22:1083–1086.
- Huete, A. R. 1988. A soil-adjusted vegetation index (SAVI). *Remote Sensing of Environment* 25:295–309.
- Huete, A. R., K. Didan, T. Miura, E. P. Rodriguez, X. Gao, and L.G. Ferreira. 2002. Overview of the radiometric and biophysical performance of the MODIS vegetation indices. *Remote Sensing of Environment* 83:195–213.
- Huete, A. R., C. Justice, and H. Liu. 1994. Development of vegetation and soil indices for MODIS-EOS. *Remote Sensing of Environment* 49:224–234.
- Huete, A. R., H. Q. Liu, K. Batchily, and W. van Leeuwen. 1997. A comparison of vegetation indices over a global set of TM images for EOS-MODIS. *Remote Sensing of Environment* 59:440–451.
- Hutchinson, J. M. S., A. Jacquin, S. L. Hutchinson, and J. Verbesselt. 2015. Monitoring vegetation change and dynamics on U.S. Army training lands using satellite image time series analysis. *Journal of Environmental Management* 150:355–366.
- Irwin, B. J., T. Wagner, J. R. Bence, M. V. Kepler, W. Liu, and D. B. Hayes. 2013. Estimating spatial and temporal components of variation for fisheries count data using negative binomial mixed models. *Transactions of the American Fisheries Society* 142:171–183.
- Ji, L., L. Zhang, and B. K. Wylie. 2009. Analysis of dynamic thresholds for the normalized difference water index. *Photogrammetric Engineering and Remote Sensing* 75:1307–1317.
- Johnson, D. H. 1980. The comparison of usage and availability measurements for evaluating resource preference. *Ecology* 61:65–71.
- Kauth, R. J., and G. S. Thomas. 1976. The Tasseled Cap - A graphic description of the spectral-temporal development of agricultural crops as seen by Landsat. *Proceedings of the Symposium on Machine Processing of Remotely Sensed Data, West Lafayette, Indiana, USA, 29 June-1 July 1976* 41–51.

- Kayastha, N., V. Thomas, J. Galbraith, and A. Banskota. 2012. Monitoring wetland change using inter-annual Landsat time-series data. *Wetlands* 32:1149–1162.
- Kennedy, R. E., Z. Yang, and W. B. Cohen. 2010. Detecting trends in forest disturbance and recovery using yearly Landsat time series: 1. LandTrendr - Temporal segmentation algorithms. *Remote Sensing of Environment* 114:2897–2910.
- Kennedy, R. E., Z. Yang, N. Gorelick, J. Braaten, L. Cavalcante, W. B. Cohen, and S. Healey. 2018. Implementation of the LandTrendr algorithm on Google Earth Engine. *Remote Sensing* 10:1–10.
- Kerr, J. T., and M. Ostrovsky. 2003. From space to species: Ecological applications for remote sensing. *Trends in Ecology and Evolution* 18:299–305.
- Key, C. H., and N. C. Benson. 2005. Landscape assessment: remote sensing of severity, the normalized burn ratio and ground measure of severity, the composite burn index. FIREMON: Fire effects monitoring and inventory system Ogden, Utah: USDA Forest Service, Rocky Mountain Research Station. Ogden, Utah, USA
- Krebs, C. J. 2001. *Ecology: The experimental analysis of distribution and abundance*. Benjamin Cummings. San Francisco, California, USA.
- Lahoz-Monfort, J. J., G. Guillera-Arroita, E. J. Milner-Gulland, R. P. Young, and E. Nicholson. 2010. Satellite imagery as a single source of predictor variables for habitat suitability modelling: How Landsat can inform the conservation of a critically endangered lemur. *Journal of Applied Ecology* 47:1094–1102.
- Lang, M. W., S. Purkis, V. V Klemas, and R. W. Tiner. 2015. Promising developments and future challenges for remote sensing of wetlands. Pages 381–402 in R. Tiner, M. W. Lang, and V. V Klemas, editors. *Remote Sensing of Wetlands: Applications and Advances*. Volume 10.
- Lillesand, T. M., and R. W. Kiefer. 1994. *Remote sensing and photo interpretation*. John Wiley and Sons: New York, New York, USA.
- Lindén, A., and S. Mäntyniemi. 2011. Using the negative binomial distribution to model overdispersion in ecological count data. *Ecology* 92:1414–1421.
- Link, W. A., M. R. Schofield, R. J. Barker, and J. R. Sauer. 2018. On the robustness of N-mixture models. *Ecology* 99:1547–1551.

- Lynch, H. J., J. T. Thorson, and A. O. Shelton. 2014. Dealing with under- and over-dispersed count data in life history, spatial, and community ecology. *Ecology* 95:3173–3180.
- Martin, T. G., B. A. Wintle, J. R. Rhodes, P. M. Kuhnert, S. A. Field, S. J. Low-Choy, A. J. Tyre, and H. P. Possingham. 2005. Zero tolerance ecology: Improving ecological inference by modelling the source of zero observations. *Ecology Letters* 8:1235–1246.
- McFeeters, S. K. 1996. The use of the Normalized Difference Water Index (NDWI) in the delineation of open water features. *International Journal of Remote Sensing* 17:1425–1432.
- McGarigal, K., H. Y. Wan, K. A. Zeller, B. C. Timm, and S. A. Cushman. 2016. Multi-scale habitat selection modeling: a review and outlook. *Landscape Ecology* 31:1161–1175.
- Mexicano, L., E. P. Glenn, O. Hinojosa-Huerta, J. Garcia-Hernandez, K. Flessa, and A. Hinojosa-Corona. 2013. Long-term sustainability of the hydrology and vegetation of Cienega de Santa Clara, an anthropogenic wetland created by disposal of agricultural drain water in the delta of the Colorado River, Mexico. *Ecological Engineering* 59:111–120.
- Mexicano, L., P. L. Nagler, F. Zamora-Arroyo, and E. P. Glenn. 2012. Vegetation dynamics in response to water inflow rates and fire in a brackish *Typha domingensis* Pers. marsh in the delta of the Colorado River, Mexico. *Ecological Engineering* 59:167–175.
- Muro, J., M. Canty, K. Conradsen, C. Hüttich, A. A. Nielsen, H. Skriver, F. Remy, A. Strauch, F. Thonfeld, and G. Menz. 2016. Short-term change detection in wetlands using Sentinel-1 time series. *Remote Sensing* 8:1–14.
- Nadeau, C. P., C. J. Conway, L. Piest, and W. P. Burger. 2013. Multi-species call-broadcast improved detection of endangered Yuma clapper rail compared to single-species call-broadcast. *Wetlands* 33:699–706.
- Ohmart, R. D., B. W. Anderson, and W. C. Hunter. 1988. The ecology of the Lower Colorado River from Davis Dam to the Mexico-United States International Boundary: A community profile. Biological Report. U.S. Department of the Interior: Fish and Wildlife Service. Washington, D.C. USA.
- Pau, S., T. W. Gillespie, and E. M. Wolkovich. 2012. Dissecting NDVI-species richness relationships in Hawaiian dry forests. *Journal of Biogeography* 39:1678–1686.

- Pettorelli, N., W. F. Laurance, T. G. O'Brien, M. Wegmann, H. Nagendra, and W. Turner. 2014. Satellite remote sensing for applied ecologists: Opportunities and challenges. *Journal of Applied Ecology* 51:839–848.
- Pettorelli, N., S. Ryan, T. Mueller, N. Bunnefeld, B. Jedrzejewska, M. Lima, and K. Kausrud. 2011. The Normalized Difference Vegetation Index (NDVI): Unforeseen successes in animal ecology. *Climate Research* 46:15–27.
- Pettorelli, N., J. O. Vik, A. Mysterud, J. M. Gaillard, C. J. Tucker, and N. C. Stenseth. 2005. Using the satellite-derived NDVI to assess ecological responses to environmental change. *Trends in Ecology and Evolution* 20:503–510.
- R Core Team. 2018. R: A language and environment for statistical computing. R Foundation for Statistical Computing. Vienna, Austria. <https://www.R-project.org/>.
- Rhodes, J. R. 2015. Chapter 12: Mixture models for overdispersed data. in. G. A. Fox, S. Negrete-Yankelevich, and V. J. Sosa, editors *Ecological Statistics: Contemporary Theory and Application*. Oxford University Press, USA
- Royle, J. A. 2004. N-mixture models for estimating population size from spatially replicated counts. *Biometrics* 60:108–115.
- Salvia, M., D. Ceballos, F. Grings, H. Karszenbaum, and P. Kandus. 2012. Post-fire effects in wetland environments: Landscape assessment of plant coverage and soil recovery in the Parana River delta marshes, Argentina. *Fire Ecology* 8:17–37.
- Sauer, J. R., and W. A. Link. 2011. Analysis of the North American breeding bird survey using hierarchical models. *The Auk* 128:87–98.
- Schultz, M., J. G. P. W. Clevers, S. Carter, J. Verbesselt, V. Avitabile, H. V. Quang, and M. Herold. 2016. Performance of vegetation indices from Landsat time series in deforestation monitoring. *International Journal of Applied Earth Observation and Geoinformation* 52:318–327.
- Tiegs, S. D., and M. Pohl. 2005. Planform channel dynamics of the lower Colorado River: 1976-2000. *Geomorphology* 69:14–27.
- Tucker, C. J. 1979. Red and photographic infrared linear combinations for monitoring vegetation. *Remote Sensing of Environment* 8:127–150.

- Turner, W., C. Rondinini, N. Pettorelli, B. Mora, A. K. Leidner, Z. Szantoi, G. Buchanan, S. Dech, J. Dwyer, M. Herold, L. P. Koh, P. Leimgruber, H. Taubenboeck, M. Wegmann, M. Wikelski, and C. Woodcock. 2015. Free and open-access satellite data are key to biodiversity conservation. *Biological Conservation* 182:173–176.
- Turner, W., S. Spector, N. Gardiner, M. Fladeland, E. Sterling, and M. Steininger. 2003. Remote sensing for biodiversity science and conservation. *Trends in Ecology and Evolution* 18:306–314.
- U.S. Fish and Wildlife Service. 2017. Environmental Conservation Online System. <<http://ecos.fws.gov/ecp0/reports/box-score-report>>. Accessed 5 Jan 2017.
- U.S. Fish and Wildlife Service. 2010. Yuma clapper rail (*Rallus longirostris yumanensis*) recovery plan. Draft First Revision. U.S. Fish and Wildlife Service, Southwest Region, Albuquerque, New Mexico.
- U.S. Geological Survey. 2016. Landsat—Earth observation satellites (ver. 1.1, August 2016): U.S. Geological Survey Fact Sheet 2015–3081.
- Verbesselt, J., R. Hyndman, G. Newnham, and D. Culvenor. 2010a. Detecting trend and seasonal changes in satellite image time series. *Remote Sensing of Environment* 114:106–115.
- Verbesselt, J., R. Hyndman, A. Zeileis, and D. Culvenor. 2010b. Phenological change detection while accounting for abrupt and gradual trends in satellite image time series. *Remote Sensing of Environment* 114:2970–2980.
- Wang, R., J. A. Gamon, R. A. Montgomery, P. A. Townsend, A. I. Zyguelbaum, K. Bitan, D. Tilman, and J. Cavender-Bares. 2016. Seasonal variation in the NDVI-species richness relationship in a prairie grassland experiment (cedar creek). *Remote Sensing* 8.
- Warton, D. I. 2005. Many zeros does not mean zero inflation: Comparing the goodness-of-fit of parametric models to multivariate abundance data. *Environmetrics* 16:275–289.
- Watts, L. M., and S. W. Laffan. 2014. Effectiveness of the BFAST algorithm for detecting vegetation response patterns in a semi-arid region. *Remote Sensing of Environment* 154:234–245.
- Wei, J., D. Lu, X. Shao, D. Li, and M. Wu. 2017. Examining land cover and greenness dynamics in Hangzhou Bay in 1985–2016 using Landsat time-series data. *Remote Sensing* 10:32.

Wilén, B. O., and M. K. Bates. 1995. The US Fish and Wildlife Service's National Wetlands Inventory Project. *Vegetatio* 118:153–169.

Wilson, E. H., and S. A. Sader. 2002. Detection of forest harvest type using multiple dates of Landsat TM imagery. *Remote Sensing of Environment* 80:385–396.

Xue, J., and B. Su. 2017. Significant remote sensing vegetation indices: A review of developments and applications. *Journal of Sensors* 2017.

## APPENDIX A: YUMA RIDGWAY'S RAIL RELATIVE ABUNDANCE MODELING: ADDITIONAL INFORMATION

### Study location descriptions

Each of the 6 study locations supported Yuma Ridgway's rails and was characterized by a unique set of climatic and environmental conditions. We attempted to account for such differences in the structure of our model (i.e., zero-inflation probability and random effects).

1) *Havasu National Wildlife Refuge* (Mohave County, Arizona and San Bernardino County, California): Havasu National Wildlife Refuge protects 48 river km of the Colorado River, including one of the last remaining natural reaches through the Topock Gorge. Emergent wetland parcels are scattered along the Topock Gorge in small backwaters and side channels, but most emergent wetland vegetation is concentrated in the Topock Marsh. This 1600 ha marsh is dominated by cattails (*Typha spp*), bulrush (*Schoenoplectus spp*), and increasingly, the invasive salt cedar (Young et al. 2015). Marsh bird survey points are distributed across Topock Marsh and in emergent marsh parcels throughout Topock Gorge. The approximate elevation of Havasu National Wildlife Refuge is 159 m and annual precipitation averages 11.8 cm.

2) *Cibola National Wildlife Refuge* (La Paz County, Arizona and Riverside County, CA): This National Wildlife Refuge was established in 1964 to mitigate the effects of river regulation, channelization, and straightening. The refuge maintains 566 ha of marshes, meanders, and backwaters for migrating waterfowl and other wetland-dependent wildlife. Cattails and bulrushes are the dominant wetland species in most marshes. Marsh bird survey points are located primarily within the managed marshes, but several routes traverse less heavily managed backwaters and old river channel. The approximate elevation of Cibola National Wildlife Refuge is 67 m and annual rainfall averages 9.7 cm.

3) *Imperial National Wildlife Refuge* (Yuma County, Arizona and Imperial County, CA): This refuge protects a mosaic of marshes, backwaters, and the last un-channelized stretch of the Colorado River north of the Mexico border. The refuge maintains 60 ha of marshes as habitat for Yuma Ridgway's rails. These marshes are periodically burned to reset marsh succession (Conway 2010). A single survey route meanders through the managed marsh units, whereas remaining routes are distributed throughout backwaters and along the main channel of the Colorado River. Average elevation of Imperial National Wildlife Refuge is 59 m and annual rainfall averages 8.5 cm.

4) *Mittry Lake Wildlife Area* (Yuma County, Arizona): Located just south of the Imperial Dam, this wildlife area protects more than 480 ha of marsh for waterfowl and wetland-dependent species (National Audubon Society, 2019). Much of the marsh area is concentrated in an expansive cattail and bulrush marsh with meandering waterways and pools. Most survey routes are located within this main marsh parcel; however, several routes traverse smaller, isolated marsh parcels scattered throughout the wildlife area. Wetland fires (prescribed and natural) frequent Mittry Lake Wildlife Area, which is jointly managed by the Bureau of Land Management, Bureau of Reclamation, and Arizona Game and Fish Department. Average elevation of Mittry Lake Wildlife Area is 56 m and annual rainfall averages 8.5 cm.

5) *Lower Gila River* (Yuma County and Maricopa County, Arizona): Marsh bird survey routes are widely distributed along the Lower Gila River from south of Yuma, Arizona to Phoenix, Arizona. Water from the Lower Gila River is largely diverted for municipal and agricultural use and consequently, the river is nearly dewatered (Huckleberry 1994, Cohen et al. 2001, Glenn et al. 2008). Wetland parcels are generally small and separated by large expanses of dry river bed or salt cedar thickets. Furthermore, extant wetlands along the Lower Gila River often depend on recycled agricultural water, natural seeps, and mitigation efforts. As such, emergent wetland vegetation can be quite ephemeral and temporally dynamic along the Lower Gila River, expanding and contracting in response to water availability. Elevation along the Lower Gila River ranges from 43 m near Yuma, Arizona to 331 m outside of Phoenix, Arizona. Annual total rainfall averages 8.5 cm near Yuma, Arizona and 20.3 cm around Phoenix, Arizona.

6) *Sonny Bono Salton Sea National Wildlife Refuge* (Imperial County, California): Created along the shores of the Salton Sea, this national wildlife refuge provides 334 ha of wetland area in irrigated units, although only 69 ha are managed as Yuma Ridgway's rail habitat. Emergent wetlands have expanded recently along the shores of the Salton Sea and these unmanaged wetlands are fed entirely by recycled water (e.g., agricultural run-off) from the New and Alamo Rivers (Barnum et al. 2017). Most of the survey points are distributed along the managed wetland parcels, but additional routes cover unmanaged marshes on the southeast side of the Sea, and isolated reclamation wetland units adjacent to the main refuge. Average elevation at the Salton Sea is -69 m and annual rainfall averages 8.4 cm.

## Satellite-derived metrics of marsh condition: Descriptions and justification

Our goal was to identify the most appropriate satellite-derived metrics of marsh condition with which to model heterogeneity in relative abundance of rails. We derived marsh condition metrics from vegetation greenness and vegetation moisture content indices as well as a fused (greenness + moisture content) index. For each year of the survey period (2006-2018) we calculated the following marsh condition covariates:

1) *Maximum vegetation greenness and moisture* – Marshes fill with decadent vegetation as they senesce, and this decadent vegetation may suppress annual growth of new emergent vegetation. Therefore, measurements of vegetation greenness and moisture content should decrease as marshes senesce. We calculated the maximum greenness and moisture content values for each survey point during each year of the survey period. We predicted that expected rail counts would correlate positively with measures of maximum vegetation greenness and moisture.

2) *Minimum vegetation greenness and moisture* – The non-native phragmites grows in dense monotypic stands along Lower Colorado River riparian areas (Glenn et al. 1996, 2008). Phragmites readily encroaches into emergent wetland in the absence of disturbance, and negatively affect rail habitat (Eddleman 1989). Furthermore, phragmites stays green through the winter, whereas many emergent wetland plant species go dormant in the winter. As such, the presence of phragmites in marshes may inflate minimum vegetation greenness and vegetation moisture content. We predicted that expected rail counts would be negatively correlated with minimum vegetation greenness and moisture content.

3) *Change in vegetation greenness or moisture (annual max - annual min)* – This is a measure of the seasonality of marsh vegetation. We hypothesized that the magnitude of change in vegetation greenness and/or moisture decreases as wetlands senesce (e.g., fill with decadent vegetation or are encroached by phragmites). Yuma Ridgway's rails prefer early successional emergent marshes which may show greater seasonality than late seral stage marshes. We therefore predicted that expected rail counts would correlate positively with the seasonality of marsh vegetation.

4) *Rate of vegetation growth* – We calculated rate of growth (i.e., slope) for each index during the Yuma Ridgway's rail breeding season (March – August; Eddleman and Conway 2018). We considered slope as an informative covariate because the rate of vegetation growth (and thus green-up and accumulation of vegetation moisture) in the spring is likely suppressed by decadent vegetation in

senescent marshes. We predicted that expected rail counts would correlate positively with rates of vegetation change in the spring.

5) *Instantaneous vegetation greenness or moisture* – Measurements of vegetation greenness and moisture content concurrent with marsh bird surveys should reflect marsh condition at the time of a given survey. We predicted that expected rail counts would correlate positively with instantaneous vegetation greenness and moisture content.

5) *Accumulated greenness and moisture* – We considered that accumulated marsh greenness or moisture content may reflect multi-annual variation in marsh condition. We therefore calculated accumulated condition measures by summing all monthly index (e.g., greenness) values during 2, 3, and 5-year time intervals preceding surveys. For example, we calculated 5-year accumulated greenness for a given survey by summing the 60 preceding monthly greenness measurements for that survey point.

6) *Proportion vegetated* – We predicted that the expected number of rails would be positively correlated with the amount of vegetation within the 224-m point buffers. As such, we included the proportion of vegetation of each point buffer as a covariate in our rail abundance models. We estimated the proportion of vegetation within each point buffer (separately for each year) by calculating the area of each buffer classified as vegetation and dividing by the total area of the buffer (15.78 ha).

#### Spectral indices for relative rail abundance modeling

We sought to identify the most appropriate spectral index with which measure the important marsh condition covariates in the models of relative Yuma Ridgway's rail abundance. We evaluated several indices commonly used to measure vegetation greenness and moisture content:

1) *Normalized difference vegetation index (NDVI)* – NDVI reflects differences in leaf pigments (e.g., chlorophyll) and is widely used to estimate vegetation condition and primary productivity (Tucker 1979, Pettorelli et al. 2011).

2) *Tasseled Cap Greenness (TCG)* – Tasseled Cap Transformations leverage all Landsat spectral bands to create principal component bands that are sensitive to various earth features (Kauth and Thomas 1976). TCG is one such principal component that correlates with the presence and density of vegetation (Kauth and Thomas 1976). TCG has been used to track green biomass, detect change in

forested systems, and assist with landcover classification (Baker et al. 2007, Fickas et al. 2016, Schultz et al. 2016, Tang et al. 2016).

3) *Normalized difference moisture index (NDMI)* – This index reflects vegetation moisture content and correlates strongly with vegetation productivity (Gao 1996). NDMI has been used to monitor vegetation condition (Hislop et al. 2018), detect disturbances in forested systems (Wilson and Sader 2002, DeVries et al. 2015b, Schultz et al. 2016), and monitor flooding in riverine wetlands (Guo et al. 2017).

4) *Tasseled Cap Wetness (TCW)* – TCW reflects vegetation moisture content and correlates with vegetation productivity (Kauth and Thomas 1976). TCW is used in wetland classification (Tana et al. 2013) as well as change detection applications (Cohen et al. 2018).

5) *NDVINDMI (NVMI)* – We fused NDVI and NDMI to create a new index of wetland condition that incorporates variation in vegetation moisture and greenness.

#### Extended modeling results

We performed multiple stages of covariate reduction and model selection to identify 1) the optimal set of covariates to control for variable survey-level detection probability, 2) the most appropriate marsh condition covariates to include in the models, and 3) the most appropriate model structure (i.e., statistical distribution and random effects structure). We first identified the optimal set of detectability covariates (Table A.1).

Table A.1. Detectability models included linear and quadratic effects for survey date and time of day. Interactions involved both linear and quadratic effects when applicable. The second and third best models were not competitive and are included only for illustrative purposes.

Model	Parameters					Delta AIC	df
	Survey date: Linear	Time of day: Linear	Survey date: Quadratic	Time of day: Quadratic	Interaction		
Detect_1	x	x	x	x	x	0	10
Detect_2	x	x		x	x	13.13	7
Detect_3	x	x	x	x		15.69	6
Detect_4	x	x		x		20.66	5
Detect_5		x		x		105.82	4
Detect_6	x	x	x		x	147.84	7
Detect_7	x	x			x	191.12	5
Detect_8	x	x	x			219.77	5
Detect_9	x					283.64	3
Detect_10	x		x			446.19	4
Detect_11	x					446.93	3

We considered 116 candidate marsh condition covariates because we sought to identify: 1) the most informative marsh condition covariates for relative Yuma Ridgway's rail abundance models, 2) the most appropriate temporal scale at which to measure the marsh condition covariates, and 3) the most appropriate spectral index with which to measure marsh condition for rail abundance modeling. We first selected the optimal temporal scale for each marsh covariate (Tables A.2–A.16).

Table A.2. Temporal-scale optimization of accumulated greenness covariates. All models were fit with negative binomial regression and included the optimal detectability covariates. Delta AIC was calculated against the single best marsh covariate.

Category	Index	Temporal scale	Delta AIC	df
Greenness	TCG	5-year	434.89	11
Greenness	TCG	3-year	443.71	11
Greenness	TCG	2-year	451.83	11
Greenness	NDVI	3-year, breeding	454.21	11
Greenness	NDVI	5-year	454.35	11
Greenness	TCG	2-year, breeding	455.09	11
Greenness	NDVI	2-year, breeding	455.39	11
Greenness	TCG	3-year, breeding	455.41	11
Greenness	NDVI	5-year, breeding	455.77	11
Greenness	NDVI	3-year	455.77	11
Greenness	TCG	5-year, breeding	455.93	11
Greenness	NDVI	2-year	456.00	11

Table A.3. Temporal-scale optimization of accumulated vegetation moisture covariates. All models were fit with negative binomial regression and included the optimal detectability covariates. Delta AIC was calculated against the single best marsh covariate.

Category	Index	Temporal scale	Delta AIC	df
Moisture	NDMI	5-year	137.91	11
Moisture	NDMI	3-year	142.47	11
Moisture	NDMI	2-year	204.04	11
Moisture	NDMI	5-year, breeding	352.54	11
Moisture	NDMI	3-year, breeding	367.63	11
Moisture	TCW	5-year	383.43	11
Moisture	TCW	3-year	385.54	11
Moisture	NDMI	2-year, breeding	386.53	11
Moisture	TCW	2-year	404.09	11
Moisture	TCW	5-year, breeding	444.90	11
Moisture	TCW	3-year, breeding	445.85	11
Moisture	TCW	2-year, breeding	449.92	11

Table A.4. Temporal-scale optimization of accumulated marsh condition derived from the fused index. All models were fit with negative binomial regression and included the optimal detectability covariates. Delta AIC was calculated against the single best marsh covariate.

Category	Index	Temporal scale	Delta AIC	df
Fused	NVMI	5-year	250.42	11
Fused	NVMI	3-year	276.54	11
Fused	NVMI	2-year	326.18	11
Fused	NVMI	5-year, breeding	418.29	11
Fused	NVMI	3-year, breeding	429.47	11
Fused	NVMI	2-year, breeding	432.71	11

Table A.5. Temporal-scale optimization of change in vegetation covariates. All models were fit with negative binomial regression and included the optimal detectability covariates. Delta AIC was calculated against the single best marsh covariate.

Category	Index	Temporal scale	Delta AIC	df
Greenness	TCG	Current breeding season	428.92	11
Greenness	TCG	Previous breeding season	431.06	11
Greenness	NDVI	Previous breeding season	437.26	11
Greenness	NDVI	Current breeding season	446.00	11
Greenness	NDVI	Previous full year	449.72	11
Greenness	TCG	Current full year	451.47	11
Greenness	TCG	Previous full year	451.95	11
Greenness	NDVI	Current full year	455.72	11

Table A.6. Temporal-scale optimization of change in vegetation moisture covariates. All models were fit with negative binomial regression and included the optimal detectability covariates. Delta AIC was calculated against the single best marsh covariate.

Category	Index	Temporal scale	Delta AIC	df
Moisture	TCW	Current breeding season	171.18	11
Moisture	TCW	Previous breeding season	183.00	11
Moisture	TCW	Current full year	254.14	11
Moisture	NDMI	Current breeding season	267.39	11
Moisture	TCW	Previous full year	272.41	11
Moisture	NDMI	Previous breeding Season	328.32	11
Moisture	NDMI	Current full year	351.16	11
Moisture	NDMI	Previous full year	362.98	11

Table A.7. Temporal-scale optimization of change in vegetation condition covariates derived from the fused index. All models were fit with negative binomial regression and included the optimal detectability covariates. Delta AIC was calculated against the single best marsh covariate.

Category	Index	Temporal scale	Delta AIC	df
Fused	NVMI	Current breeding season	383.57	11
Fused	NVMI	Previous breeding season	390.99	11
Fused	NVMI	Previous full year	426.79	11
Fused	NVMI	Current full year	440.23	11

Table A.8. Temporal-scale optimization of rate of change of vegetation greenness. All models were fit with negative binomial regression and included the optimal detectability covariates. Delta AIC was calculated against the single best marsh covariate.

Category	Index	Temporal scale	Delta AIC	df
Greenness	NDVI	Previous breeding season	425.65	11
Greenness	NDVI	Current full year	430.07	11
Greenness	TCG	Previous breeding season	431.13	11
Greenness	TCG	Previous full year	443.95	11
Greenness	TCG	Current breeding season	444.42	11
Greenness	NDVI	Current breeding season	446.11	11
Greenness	NDVI	Previous full year	454.10	11
Greenness	TCG	Current full year	455.67	11

Table A.9. Temporal-scale optimization of rate of change of vegetation moisture content. All models were fit with negative binomial regression and included the optimal detectability covariates. Delta AIC was calculated against the single best marsh covariate.

Category	Index	Temporal scale	Delta AIC	df
Moisture	TCW	Current breeding season	310.16	11
Moisture	NDMI	Current breeding season	350.04	11
Moisture	NDMI	Previous breeding season	369.84	11
Moisture	TCW	Previous breeding season	374.57	11
Moisture	TCW	Previous full year	423.59	11
Moisture	TCW	Current full year	429.71	11
Moisture	NDMI	Current full year	444.07	11
Moisture	NDMI	Previous full year	446.64	11

Table A.10. Temporal-scale optimization of rate of change of fused vegetation condition covariates. All models were fit with negative binomial regression and included the optimal detectability covariates. Delta AIC was calculated against the single best marsh covariate.

Category	Index	Temporal scale	Delta AIC	df
Fused	NVMI	Previous full year	375.40	11
Fused	NVMI	Previous breeding season	386.27	11
Fused	NVMI	Current breeding season	396.11	11
Fused	NVMI	Current full year	419.77	11

Table A.11. Temporal-scale optimization of maximum vegetation moisture content covariates. All models were fit with negative binomial regression and included the optimal detectability covariates. Delta AIC was calculated against the single best marsh covariate.

Category	Index	Temporal scale	Delta AIC	df
Moisture	NDMI	Current full year	375.30	11
Moisture	NDMI	Previous full year	386.33	11
Moisture	NDMI	Previous breeding season	392.06	11
Moisture	NDMI	Previous full year	401.55	11
Moisture	TCW	Current breeding season	450.11	11
Moisture	TCW	Previous breeding season	451.80	11
Moisture	TCW	Current full year	453.23	11
Moisture	TCW	Previous full year	453.80	11

Table A.12. Temporal-scale optimization of maximum vegetation greenness covariates. All models were fit with negative binomial regression and included the optimal detectability covariates. Delta AIC was calculated against the single best marsh covariate.

Category	Index	Temporal scale	Delta AIC	df
Greenness	NDVI	Current full year	449.45	11
Greenness	TCG	Current breeding season	452.63	11
Greenness	NDVI	Previous full year	453.76	11
Greenness	TCG	Current full year	453.83	11
Greenness	NDVI	Current breeding season	454.13	11
Greenness	NDVI	Previous breeding season	456.08	11
Greenness	TCG	Previous full year	456.08	11
Greenness	TCG	Previous breeding season	456.08	11

Table A.13. Temporal-scale optimization of maximum fused marsh condition covariates. All models were fit with negative binomial regression and included the optimal detectability covariates. Delta AIC was calculated against the single best marsh covariate.

Category	Index	Temporal scale	Delta AIC	df
Fused	NVMI	Current full year	432.27	11
Fused	NVMI	Previous breeding season	432.81	11
Fused	NVMI	Previous full year	434.95	11
Fused	NVMI	Current breeding season	438.97	11

Table A.14. Temporal-scale optimization of minimum vegetation greenness covariates. All models were fit with negative binomial regression and included the optimal detectability covariates. Delta AIC was calculated against the single best marsh covariate.

Category	Index	Temporal scale	Delta AIC	df
Greenness	TCG	Previous breeding season	417.39	11
Greenness	NDVI	Previous breeding season	435.42	11
Greenness	TCG	Current breeding season	444.75	11
Greenness	TCG	Previous full year	448.96	11
Greenness	NDVI	Current full year	451.21	11
Greenness	NDVI	Current breeding season	453.02	11
Greenness	NDVI	Previous full year	455.25	11
Greenness	TCG	Current full year	455.87	11

Table A.15. Temporal-scale optimization of minimum vegetation moisture covariates. All models were fit with negative binomial regression and included the optimal detectability covariates. Delta AIC was calculated against the single best marsh covariate.

Category	Index	Temporal scale	Delta AIC	df
Moisture	NDMI	Current breeding season	0	11
Moisture	NDMI	Current full year	98.06	11
Moisture	NDMI	Previous breeding season	103.61	11
Moisture	NDMI	Previous full year	165.19	11
Moisture	TCW	Current full year	268.23	11
Moisture	TCW	Current breeding season	270.61	11
Moisture	TCW	Previous full year	294.97	11
Moisture	TCW	Previous breeding season	301.43	11

Table A.16. Temporal-scale optimization of the minimum fused vegetation condition covariates. All models were fit with negative binomial regression and included the optimal detectability covariates. Delta AIC was calculated against the single best marsh covariate.

Category	Index	Temporal scale	Delta AIC	df
Fused	NVMI	Current breeding season	171.61	11
Fused	NVMI	Previous breeding season	174.68	11
Fused	NVMI	Previous full year	287.21	11
Fused	NVMI	Current full year	314.25	11

After temporal scale optimization, we further reduced the list of candidate marsh condition variables by dropping the weaker (as judged by AIC) of any pair of colinear variables with a correlation coefficient greater than 0.7 (Fig. A.1). We selected 12 candidate marsh condition covariates, which we included in all model structure selection exercises (Table A.17).

Table A.17. The reduced set of marsh condition covariates included in the global fixed-effects model. Covariate refers to the type of measurement and Temporal scale indicates at what timeframe the covariate was derived. "Breeding season" refers to March – August. "Full" indicates covariates were derived from the full year. Index refers to the index used to estimate the associated marsh condition covariate.

Marsh condition covariate	Temporal scale	Description and justification	Predicted rail response	Index
Accumulated vegetation greenness	5 year	Accumulated greenness over 5 years of a marsh parcel. Increasing values should indicate healthier marshes	+	TCG
Maximum vegetation greenness	Current full year	Decadent vegetation may suppress emergent vegetation growth and therefore reduce maximum annual NDVI values	+	NDVI
Minimum vegetation greenness	Previous full year	Invasive evergreen species may inflate minimum greenness values and thus late seral stage marshes may stay greener in the winter	-	TCG
Minimum vegetation moisture	Current breeding season	NDMI correlates with vegetation moisture content, therefore as minimum values increase, the "dryness" of the habitat increases	-	NDMI

Change in vegetation moisture	Current breeding season	Senescent marshes with abundant decadent vegetation and woody vegetation should show less seasonality than early successional emergent marshes	+	NDMI
Accumulated vegetation moisture	5 year	Accumulated marsh vegetation moisture over 5 years will reflect overall marsh condition through time	+	NDMI
Rate of vegetation moisture change	Current breeding season	The rate of emergent vegetation growth is likely suppressed by decadent vegetation. TCW reflects vegetation moisture content, hence TCW slope values will decrease as marshes senesce	+	TCW
Minimum vegetation moisture	Current year-full	Minimum vegetation moisture will likely increase with the accumulation of senescent vegetation	-	TCW
Change in vegetation moisture	Current year-breeding season	Amount of change in the breeding season should correlate with seral stages, with early successional marshes experiencing greater change in the breeding season	+	TCW
Change in marsh vegetation	Previous full year	NVMI reflects vegetation moisture and greenness. The amount of change in NVMI during the previous breeding season should decrease as marshes senesce	+	NVMI
Instantaneous marsh condition	Concurrent with survey	NVMI reflects vegetation moisture and greenness and breeding season values indicate current marsh condition	+	NVMI
Proportion vegetated	Current year	Proportion of vegetation within the 224-m survey point buffer should correlate with the amount of wetland habitat around a survey point	+	NA

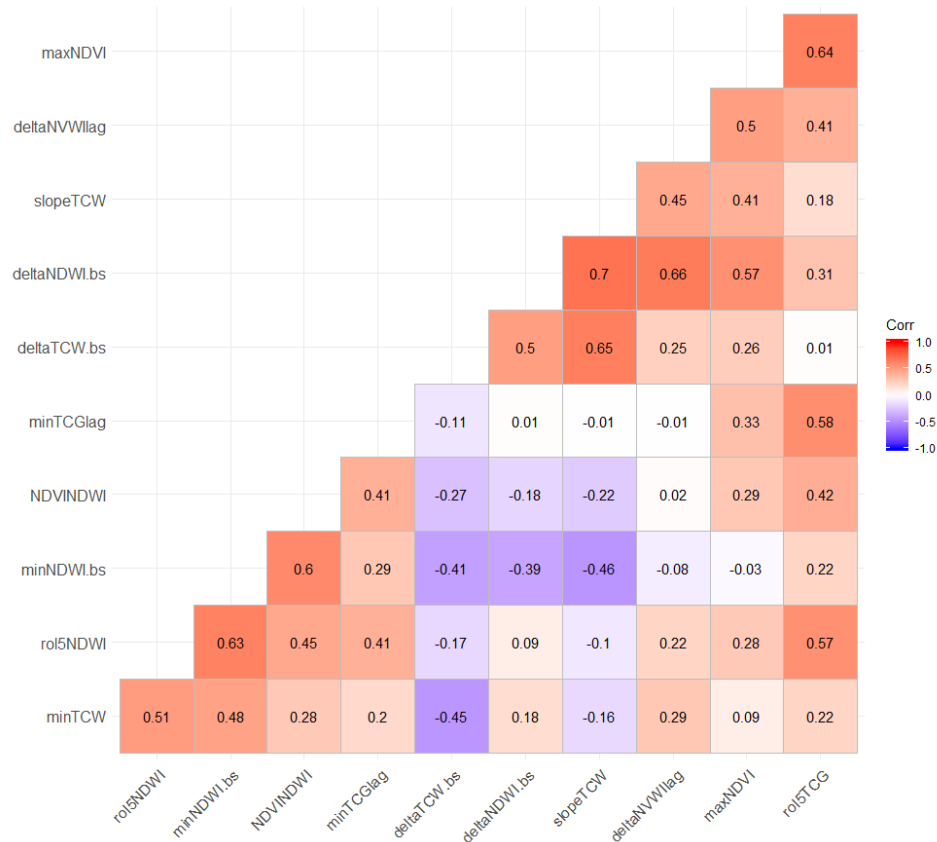


Figure A.1. Correlation plot of final marsh condition covariates. All candidate variables were assessed for collinearity and the weaker of any pair of variables with a correlation coefficient greater than 0.7 was dropped. bs = breeding season, lag = previous year, delta = amount of change, and rol5 = 5-year accumulated covariates.

### Model structure

Once we had identified the optimal set of detectability covariates and the reduced list of candidate marsh condition covariates, we sought to identify the most appropriate model structure to describe the Yuma Ridgway's rail count data. We first identified the optimal distribution (Table A.18). We then selected the optimal random effects structure (Table A.19). We included all detectability and candidate marsh condition covariates in all models during model structure selection.

Table A.18. Statistical distribution selection. The zero-inflated negative binomial distribution with a linear and quadratic effect of survey date on the dispersion parameter was the most supported model. Zero-inflation probability varied by region with a region-specific random intercept. Models based on the NB1 distribution were more supported than those built on the NB2 or Poisson distributions. X's indicate whether the model included an attribute in the structure. NB1 = negative binomial where  $var = \mu(1 + \theta)$ , NB2 = negative binomial where  $var = \mu(1 + \mu/\theta)$ , and  $\theta$  is the dispersion parameter.

Distribution	Dispersion		Zero-inflation			Delta AIC	df
	Date	Date <sup>2</sup>	Constant	Location	Location-annual intercept		
NB1	x	x		x	x	0	42
NB1	x			x	x	1.17	41
NB1				x	x	12.85	40
NB1	x	x		x		37.17	41
NB1	x			x		39.82	40
NB1				x		49.73	39
NB1	x	x	x			72.61	36
NB1	x		x			74.05	35
NB1			x			82.17	34
NB1	x	x				108.60	35
NB1	x					111.66	34
NB1						122.17	33
NB2	x			x	x	143.00	41
NB2	x	x		x	x	144.04	42
NB2				x	x	158.76	40
NB2	x	x		x		198.84	41
NB2	x			x		198.97	40
NB2				x		215.36	39
Poisson				x	x	341.20	39
NB2	x		x			363.56	35
NB2	x	x	x			365.35	36
NB2			x			373.88	34
NB2	x					405.26	34
NB2	x	x				406.60	35
Poisson				x		413.81	38
NB2						421.28	33
Poisson			x			630.65	33
Poisson						1405.88	32

### Random Effects

We then selected the most parsimonious random effects structure (conditional on the identified statistical distribution and set of fixed-effect covariates; Table A.19).

Table A.19. Random effects structure selection. The top model included all hypothesized random effects. All models were based on a zero-inflated negative binomial distribution and included the full set of candidate fixed-effects. We held the distribution constant and only altered the random effects structure. X's indicate inclusion of an attribute in the model. Dist. refers to distribution. NB1 = negative binomial where  $var = \mu(1 + \theta)$ , NB2 = negative binomial where  $var = \mu(1 + \mu/\theta)$ , and  $\theta$  is the dispersion parameter.

Dist.	Dispersion		Zero-inflation		Random effects					Delta AIC	df
	Date	Date <sup>2</sup>	Location	Location -annual intercept	Route intercept	Route-annual intercept	Broad-scale annual intercept	Route-time slope			
NB1	x	x	x	x	x	x	x	x	x	0.0	42
NB1	x	x	x	x	x	x	x			12.91	40
NB1	x	x	x	x	x	x				22.27	39
NB1	x	x	x	x	x			x	x	295.10	41
NB1	x	x	x	x	x				x	332.20	40
NB1	x	x	x	x	x			x		365.08	39
NB1	x	x	x	x	x					410.70	38
NB1	x	x	x	x				x		2291.83	38

### Final model selection

Finally, we compared 26 plausible combinations of marsh condition covariates and 1 model with no marsh condition variables (i.e., a null model) and selected the top model using AIC (Table A.20). All models were fit with the full set of detection covariates and optimal model structure identified from the previous model selection steps.

Table A.20. Final fixed-effect model selection. All models were fit with the full set of detectability covariates as well as the optimal model structure. bs = breeding season, lag = previous year, delta = amount of change, and rol5 = 5-year accumulated values.

Model	Formula	Delta AIC	df
1	<i>Detectability Covariates</i> + minNDMI.bs + rol5NDMI + rol5TCG + deltaNDMI.bs + deltaNDMI.bs <sup>2</sup> + deltaNVMIIag + deltaNVMIIag <sup>2</sup> + PropVeg + PropVeg <sup>2</sup>	0.00	34
2	<i>Detectability Covariates</i> + minNDMI.bs + rol5NDMI * rol5TCG + deltaNDMI.bs + deltaNDMI.bs <sup>2</sup> + deltaNVMIIag + deltaNVMIIag <sup>2</sup> + PropVeg + PropVeg <sup>2</sup>	0.08	35
3	<i>Detectability Covariates</i> + minNDMI.bs + rol5NDMI * rol5TCG + minTCGlag + deltaNDMI.bs + deltaNDMI.bs <sup>2</sup> + deltaNVMIIag + deltaNVMIIag <sup>2</sup> + PropVeg + PropVeg <sup>2</sup>	0.11	36
4	<i>Detectability Covariates</i> + minTCW + minNDMI.bs + rol5NDMI * rol5TCG + minTCGlag + deltaNDMI.bs + deltaNDMI.bs <sup>2</sup> + deltaNVMIIag + deltaNVMIIag <sup>2</sup> + PropVeg + PropVeg <sup>2</sup>	0.16	37
5	<i>Detectability Covariates</i> + minNDMI.bs + rol5NDMI + rol5TCG + minTCGlag + deltaNDMI.bs + deltaNDMI.bs <sup>2</sup> + deltaNVMIIag + deltaNVMIIag <sup>2</sup> + PropVeg + PropVeg <sup>2</sup>	0.45	35
6	<i>Detectability Covariates</i> + minNDMI.bs + rol5NDMI * rol5TCG + minTCW + deltaNDMI.bs + deltaNDMI.bs <sup>2</sup> + deltaNVMIIag + deltaNVMIIag <sup>2</sup> + PropVeg + PropVeg <sup>2</sup>	0.99	36
7	<i>Detectability Covariates</i> + minNDMI.bs + rol5NDMI + deltaNDMI.bs + deltaNDMI.bs <sup>2</sup> + deltaNVMIIag + deltaNVMIIag <sup>2</sup> + PropVeg + PropVeg <sup>2</sup>	1.60	33
9	<i>Detectability Covariates</i> + minTCW + minNDMI.bs + rol5NDMI * rol5TCG + minTCGlag + deltaNDMI.bs + deltaNDMI.bs <sup>2</sup> + deltaNVMIIag + deltaNVMIIag <sup>2</sup> + NVMI + PropVeg + PropVeg <sup>2</sup>	1.66	38
10	<i>Detectability Covariates</i> + minNDMI.bs + rol5NDMI + deltaNDMI.bs + deltaNDMI.bs <sup>2</sup> + deltaNVMIIag + deltaNVMIIag <sup>2</sup> + PropVeg + PropVeg <sup>2</sup>	2.33	32
11	<i>Detectability Covariates</i> + minNDMI.bs + rol5NDMI + deltaNDMI.bs + deltaNDMI.bs <sup>2</sup> + deltaNVMIIag + deltaNVMIIag <sup>2</sup> + maxNDVI + PropVeg + PropVeg <sup>2</sup>	3.38	34
12	<i>Detectability Covariates</i> + minTCW + minNDMI.bs + rol5NDMI * rol5TCG + minTCGlag + deltaNDMI.bs + deltaNDMI.bs <sup>2</sup> + deltaNVMIIag + deltaNVMIIag <sup>2</sup> + maxNDVI + NVMI + PropVeg + PropVeg <sup>2</sup>	3.64	39
13	<i>Detectability Covariates</i> + minNDMI.bs + rol5NDMI + minTCW + deltaNDMI.bs + deltaNDMI.bs <sup>2</sup> + deltaNVMIIag + deltaNVMIIag <sup>2</sup> + PropVeg + PropVeg <sup>2</sup>	3.69	33

14	<i>Detectability Covariates</i> + minNDMI.bs + rol5NDMI + minTCGlag + maxNDVI + deltaNDMI.bs + deltaNDMI.bs <sup>2</sup> + deltaNVMilag + deltaNVMilag <sup>2</sup> + PropVeg + PropVeg <sup>2</sup>	5.18	35
15	<i>Detectability Covariates</i> + deltaTCW.bs + deltaTCW.bs <sup>2</sup> + minNDMI.bs + rol5NDMI * rol5NDVI + minTCW + deltaNDMI.bs + deltaNDMI.bs <sup>2</sup> + deltaNVMilag + deltaNVMilag <sup>2</sup> + NVMI + PropVeg + PropVeg <sup>2</sup>	5.20	38
16	<i>Detectability Covariates</i> + slopeTCW + minTCW + deltaTCW.bs + +minNDMI.bs + rol5NDMI * rol5TCG + minTCGlag + deltaNDMI.bs + deltaNDMI.bs <sup>2</sup> + deltaNVMilag + deltaNVMilag <sup>2</sup> + maxNDVI + NVMI + PropVeg + PropVeg <sup>2</sup>	5.34	41
17	<i>Detectability Covariates</i> + minNDMI.bs + rol5NDMI + deltaNDMI.bs + deltaNDMI.bs <sup>2</sup> + deltaNVMilag + deltaNVMilag <sup>2</sup> + maxNDVI + NVMI + PropVeg + PropVeg <sup>2</sup>	5.36	35
18	<i>Detectability Covariates</i> + minNDMI.bs + rol5NDMI + minTCW + deltaNDMI.bs + deltaNDMI.bs <sup>2</sup> + deltaNVMilag + deltaNVMilag <sup>2</sup> + NVMI + PropVeg + PropVeg <sup>2</sup>	5.68	34
19	<i>Detectability Covariates</i> + slopeTCW + slopeTCW <sup>2</sup> + minTCW + deltaTCW.bs + deltaTCW.bs <sup>2</sup> + +minNDMI.bs + rol5NDMI * rol5TCG + minTCGlag + deltaNDMI.bs + deltaNDMI.bs <sup>2</sup> + deltaNVMilag + deltaNVMilag <sup>2</sup> + maxNDVI + NVMI + PropVeg + PropVeg <sup>2</sup>	6.38	43
20	<i>Detectability Covariates</i> + minTCW + deltaTCW.bs + deltaTCW.bs <sup>2</sup> + +minNDMI.bs + rol5NDMI + deltaNDMI.bs + deltaNDMI.bs <sup>2</sup> + deltaNVMilag + deltaNVMilag <sup>2</sup> + maxNDVI + NVMI + PropVeg + PropVeg <sup>2</sup>	8.80	38
21	<i>Detectability Covariates</i> + deltaTCW.bs + deltaTCW.bs <sup>2</sup> + minNDMI.bs + rol5NDMI + rol5NDVI + minTCW + deltaNDMI.bs + deltaNDMI.bs <sup>2</sup> + deltaNVMilag + deltaNVMilag <sup>2</sup> + NVMI + PropVeg + PropVeg <sup>2</sup>	9.02	37
22	<i>Detectability Covariates</i> + slopeTCW + slopeTCW <sup>2</sup> + minTCW + deltaTCW.bs + deltaTCW.bs <sup>2</sup> + minNDMI.bs + rol5NDMI + deltaNDMI.bs + deltaNDMI.bs <sup>2</sup> + deltaNVMilag + deltaNVMilag <sup>2</sup> + maxNDVI + NVMI + PropVeg + PropVeg <sup>2</sup>	10.03	40
23	<i>Detectability Covariates</i> + minNDMI.bs + rol5NDMI * rol5TCG + minTCGlag + deltaTCW.bs + deltaTCW.bs <sup>2</sup> + deltaNVMilag + deltaNVMilag <sup>2</sup> + PropVeg + PropVeg <sup>2</sup>	27.48	36
24	<i>Detectability Covariates</i> + minNDMI.bs + rol5NDMI + rol5TCG + deltaNDMI.bs + deltaNDMI.bs <sup>2</sup> + deltaTCWlag.bs + deltaTCWlag.bs <sup>2</sup> + PropVeg + PropVeg <sup>2</sup>	47.66	34
25	<i>Detectability Covariates</i> + deltaTCW.bs + minNDMI.bs + rol5NDMI + rol5NDVI + minTCW + deltaNDMI.bs + deltaNVMilag + PropVeg + PropVeg <sup>2</sup>	50.59	33
26	<i>Detectability Covariates</i> + minNDMI.bs + rol5NDMI + minTCGlag + maxNDVI + deltaNDMI.bs + deltaNVMilag + PropVeg + PropVeg <sup>2</sup>	58.06	33
27	<i>Detectability Covariates</i>	756.63	25

Our final model can be represented by the following set of equations:

$$Y_{i,s,t} \sim \text{NB}_1(\mu_{i,j,s,t}, \theta \mid \text{NZI}) \quad (1)$$

$i$  = survey point

$j$  = route

$s$  = survey visit number (within year)

$t$  = year

$\text{NZI}$  = the event the data point was not a structural zero

$\theta$  = dispersion parameter

$$\log(\mu_{i,j,s,t}) = \log(E[Y_{i,j,s,t}]) =$$

$$\beta_0 + \text{DetectabilityCovs.} + \text{MarshConditionCovs.} + a_j + (\lambda + t_j) \times \text{year}_t + b_t + c_{j,t} \quad (2)$$

$\beta_0$  = fixed intercept

$a_j$  = random spatial (route) intercept

$\lambda$  = fixed (average) temporal trend over all regions

$t_j$  = random temporal slope by route

$b_t$  = broad-scale annual random intercept

$c_{j,t}$  = route-specific annual random intercept

$$\text{Var}(Y_{i,s,t} \mid \mu_{i,j,s,t}, \text{NZI}) = \mu_{i,j,s,t}(1 + \theta) \quad (3)$$

$$\log(\theta) = \gamma_0 + \gamma_1 \times \text{DOY}_{i,j,s,t} + \gamma_2 \times \text{DOY}_{i,j,s,t}^2 \quad (4)$$

where  $\gamma$ 's are dispersion regression coefficients and DOY is Julian day of survey,

$$\text{logit}(p^{(ZI)}) = \phi_0 + \phi_{\text{region}_j} + r_{j,t}, \quad (5)$$

where  $\phi$ 's are zero-inflation regression coefficients,  $p^{(ZI)}$ , is the zero-inflation probability and  $r_{j,t}$  is location-specific annual random intercept.

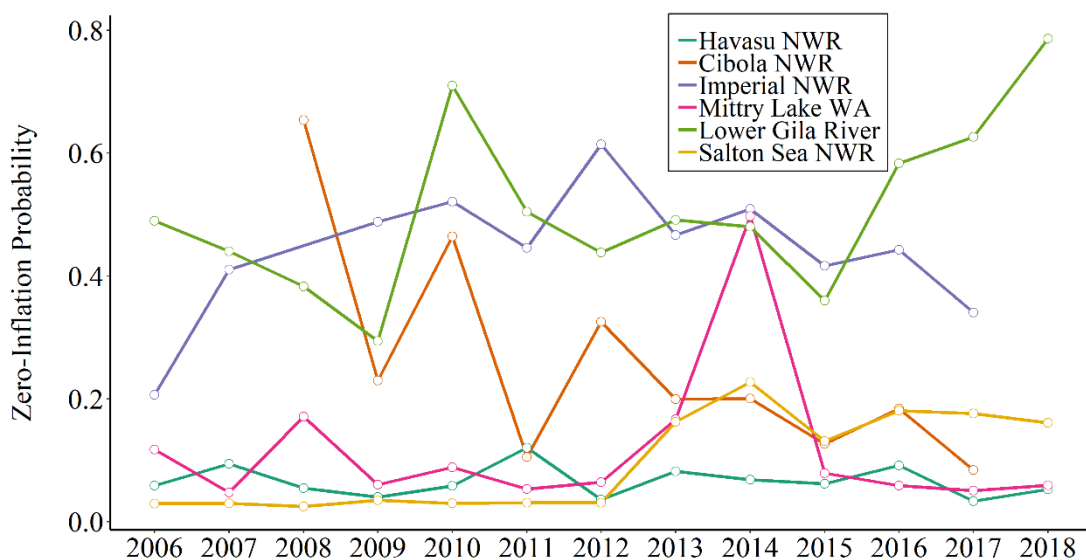


Figure A.2. Zero-inflation probability varied by study location and randomly by year (random location-specific annual intercept).

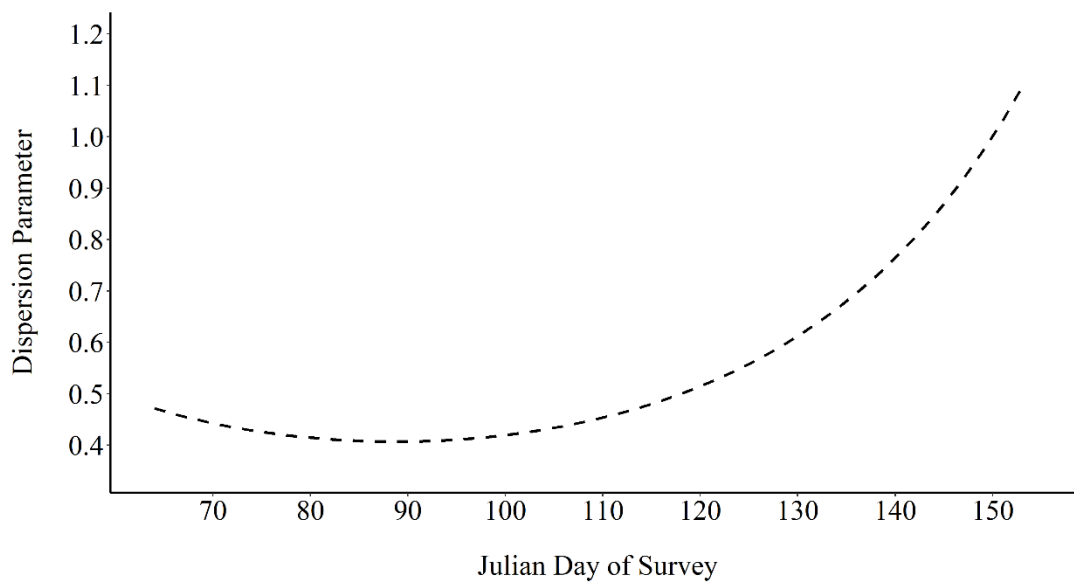


Figure A.3. Estimated relationship between the dispersion parameter and survey date in the top model.

## LITERATURE CITED

- Baker, C., R. L. Lawrence, C. Montagne, and D. Patten. 2007. Change detection of wetland ecosystems using Landsat imagery and change vector analysis. *Wetlands* 27:610–619.
- Barnum, D. A., T. Bradley, M. Cohen, B. Wilcox, and G. Yanega. 2017. State of the Salton Sea—A science and monitoring meeting of scientists for the Salton Sea. U.S. Geological Survey Open-File Report 2017–1005, 20 p
- Cohen, M. J., C. Henges-Jeck, and G. Castillo-Moreno. 2001. A preliminary water balance for the Colorado River delta, 1992-1998. *Journal of Arid Environments* 49:35–48.
- Cohen, W. B., Z. Yang, S. P. Healey, R. E. Kennedy, and N. Gorelick. 2018. A LandTrendr multispectral ensemble for forest disturbance detection. *Remote Sensing of Environment* 205:131–140.
- DeVries, B., J. Verbesselt, L. Kooistra, and M. Herold. 2015. Robust monitoring of small-scale forest disturbances in a tropical montane forest using Landsat time series. *Remote Sensing of Environment* 161:107–121.
- Fickas, K. C., W. B. Cohen, and Z. Yang. 2016. Landsat-based monitoring of annual wetland change in the Willamette Valley of Oregon, USA from 1972 to 2012. *Wetlands Ecology and Management* 24:73–92.
- Gao, B. 1996. NDWI—A normalized difference water index for remote sensing of vegetation liquid water from space. *Remote Sensing of Environment* 58:257–266.
- Glenn, E. P., K. Hucklebridge, O. Hinojosa-Huerta, P. L. Nagler, and J. Pitt. 2008. Reconciling environmental and flood control goals on an arid-zone river: Case study of the Limitrophe region of the Lower Colorado River in the United States and Mexico. *Environmental Management* 41:322–335.
- Guo, M., J. Li, C. Sheng, J. Xu, and L. Wu. 2017. A review of wetland remote sensing. *Sensors (Switzerland)* 17:1–36.
- Hislop, S., S. Jones, M. Soto-Berelov, A. Skidmore, A. Haywood, and T. H. Nguyen. 2018. Using Landsat spectral indices in time-series to assess wildfire disturbance and recovery. *Remote Sensing* 10:1–17.

- Huckleberry, G. 1994. Contrasting channel response to floods on the middle Gila River, Arizona. *Geology* 22:1083–1086.
- Kauth, R. J., and G. S. Thomas. 1976. The Tasseled Cap - A graphic description of the spectral-temporal development of agricultural crops as seen by Landsat. Proceedings of the Symposium on Machine Processing of Remotely Sensed Data, West Lafayette, Indiana, U.S.A, 29 June-1 July 1976 41–51.
- National Audubon Society. 2018. Important bird areas in the U.S.- Mittry Lake State Wildlife Area. <https://netapp.audubon.org/iba/Reports/907>. Accessed 10 March 2019.
- Pettorelli, N., S. Ryan, T. Mueller, N. Bunnefeld, B. Jedrzejewska, M. Lima, and K. Kausrud. 2011. The Normalized Difference Vegetation Index (NDVI): Unforeseen successes in animal ecology. *Climate Research* 46:15–27.
- Schultz, M., J. G. P. W. Clevers, S. Carter, J. Verbesselt, V. Avitabile, H. V. Quang, and M. Herold. 2016. Performance of vegetation indices from Landsat time series in deforestation monitoring. *International Journal of Applied Earth Observation and Geoinformation* 52:318–327.
- Tana, G., H. Letu, Z. Cheng, and R. Tateishi. 2013. Wetlands mapping in North America by decision rule classification using MODIS and ancillary data. *IEEE Journal of Selected Topics in Applied Earth Observations and Remote Sensing* 6:2391–2401.
- Tang, Z., Y. Li, Y. Gu, W. Jiang, Y. Xue, Q. Hu, T. LaGrange, A. Bishop, J. Drahota, and R. Li. 2016. Assessing Nebraska playa wetland inundation status during 1985-2015 using Landsat data and Google Earth Engine. *Environmental Monitoring and Assessment* 188.
- Tucker, C. J. 1979. Red and photographic infrared linear combinations for monitoring vegetation. *Remote Sensing of Environment* 8:127–150.
- Wilson, E. H., and S. A. Sader. 2002. Detection of forest harvest type using multiple dates of Landsat TM imagery. *Remote Sensing of Environment* 80:385–396.
- Young, N., A. West, R. Anderson, and S. Chignell. 2015. Mapping land cover and invasive tamarisk in Havasu National Wildlife Refuge, Arizona. Publication of the Natural Resource Ecology Laboratory in Collaboration with the U.S. Geological Survey. Fort Collins, Colorado, USA.

## APPENDIX B: LANDSAT IMAGERY ACQUISITION AND PROCESSING

We accessed and processed all imagery on Google Earth Engine (Gorelick et al. 2017). Landsat sensor data is regularly processed to either top of atmosphere (TOA) reflectance or surface reflectance (SR). TOA reflectance is sometimes referred to as at-satellite reflectance because it is a measure of all reflectance measured by the satellite. As such, TOA reflectance values include atmospheric effects (e.g., effects of cloud cover and atmospheric aerosols; Holben 1986). SR imagery is typically processed to remove atmospheric effects and represents reflectance from the surface of the earth. We relied on Tasseled Cap Transformations at many stages of these analyses (e.g., image classification, rail abundance modeling) and the coefficients to compute these transformations are only available for TOA imagery (Huang et al. 2002, Baig et al. 2014). To remain consistent in our analyses, we used TOA imagery to calculate all spectral indices. We followed a 9-step workflow to process the Landsat imagery and extract spectral index timeseries for our study locations (Fig. B.1). We detail each step below.

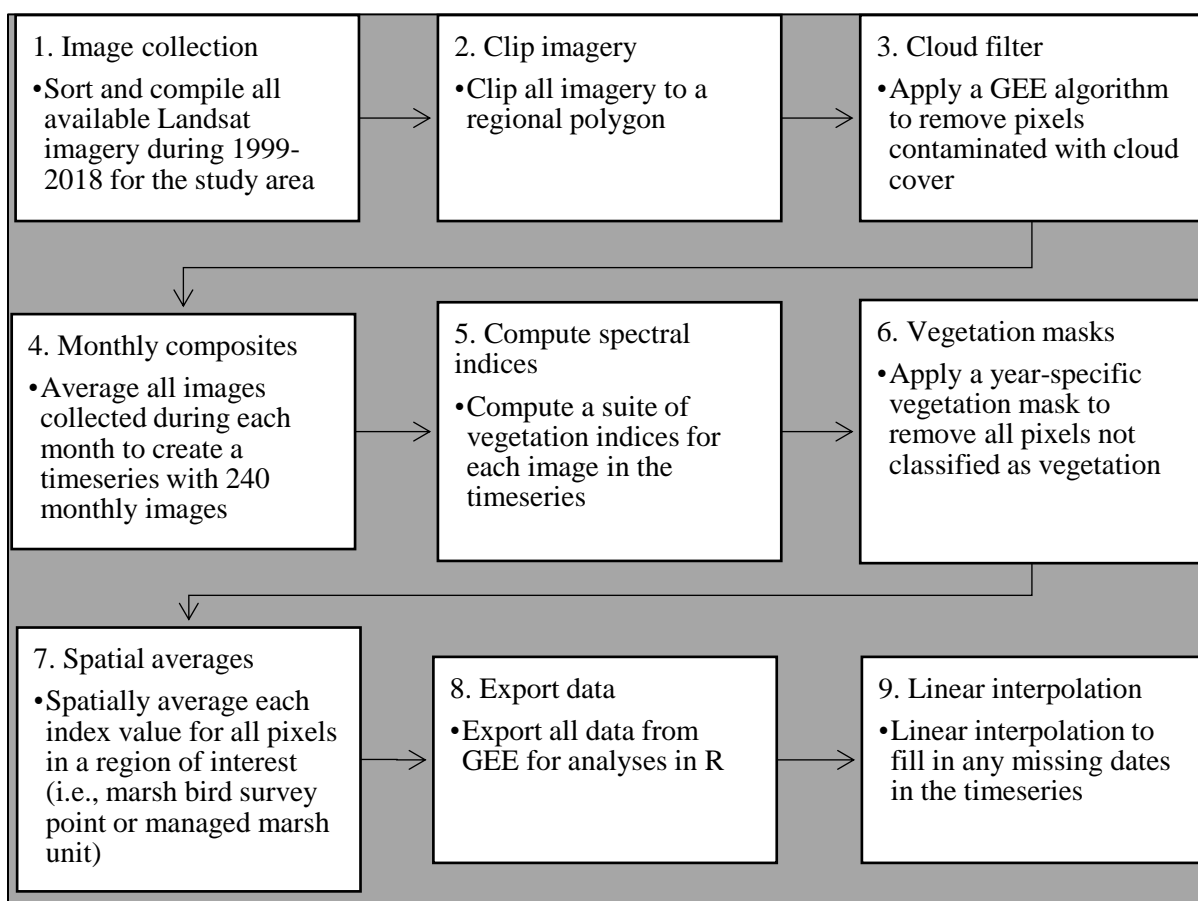


Figure B.1. Landsat imagery processing workflow to generate timeseries of spectral indices. GEE= Google Earth Engine.

### *1. Image collection*

We collected and processed Landsat imagery from 1999-2018 to ensure the BFAST algorithm had  $\geq 2$  years of imagery with which to estimate the seasonal and trend components of the timeseries before a known disturbance (earliest reference disturbance occurred February 2001). We used imagery from Landsat 5 and Landsat 7 satellites to improve the temporal coverage and density of the timeseries.

### *2. Clip imagery*

Our 6 study regions (i.e., Havasu, Cibola, Imperial, and S.B. Salton Sea National Wildlife Refuges, Mittry Lake Wildlife Area, and the Lower Gila River) were separated by wide expanses of non-habitat and we defined 4 general polygons around these 6 sites (instead of creating 1 large polygon to encompass all sites). We clipped all Landsat imagery to these 4 regional polygons to reduce the computational expense of our analyses.

### *3. Cloud filters*

Cloud cover can influence TOA reflectance values. As such, we applied a cloud scoring algorithm in Google Earth Engine to remove pixels contaminated by cloud cover. Google Earth Engine uses thermal bands and pixel brightness to estimate the probability of cloud cover in each pixel of an image (Gorelick et al. 2017). We removed all pixels with a probability of cloud cover greater than 20%.

### *4. Monthly composites*

Landsat imagery is collected with a temporal resolution of 8–16 days. We created monthly images by averaging all images collected within a given month to 1) reduce noise, 2) minimize pixel loss from cloud cover, and 3) create a timeseries with equal time steps (i.e., 12 images per year). As such, we created an image collection with 240 monthly images for each region (20 year  $\times$  12 months).

### *5. Compute spectral indices*

We then computed all desired spectral indices and added them as bands to the monthly images in our image collection (see Table 5 for index descriptions and formulas). In this way, each monthly image had bands for NDVI, NDMI, etc. Adding each index as a band to an image also greatly reduced the dimensions of our image timeseries (we had 240 monthly images with 16 bands each vs 3840 single band images).

## 6. *Vegetation masks*

We calculated spatial averages of all the pixels within a 224-m buffer of the marsh bird survey points, and thus sought to minimize the influence of water and bare areas on these averages. The U.S. Fish and Wildlife Service produces the National Wetland Inventory (NWI) to track the status and quantify the extent of wetlands in U.S. (Wilén and Bates 1995, Dahl 2006). These data are publicly available and a NWI shapefile, detailing the location and extent of all wetlands in the U.S., has been used in a wide range of research applications (e.g., Kayastha et al. 2012, Glisson et al. 2017). The NWI shapefile is logistically complicated and expensive to produce, and thus the NWI shapefile is updated infrequently (Chignell et al. 2018). Moreover, NWI layers have low commission error rates but high omission error rates (Wright and Gallant 2007). Indeed, visual inspection of the NWI layer within our study region showed numerous omission errors, particularly along the Salton Sea and Lower Gila River (NWI layers showed no emergent wetlands along the Lower Gila River). We processed 20 years of imagery for this study and the extent and location of wetlands can vary greatly during such time (even along the heavily regulated Colorado River). Rather than rely on static NWI shapefiles to define the amount of wetland habitat around each marsh bird survey point, we created year-specific vegetation layers to better represent the dynamics of the system. We detail the process through which we derived the vegetation masks below.

### 6.0 *General process*

We created the vegetation masks by classifying images into 3-4 categories, depending on the complexities of the system: 1) water, 2) bare, 3) natural vegetation, and when necessary 4) agriculture. We used Random Forest image classification implemented in GEE to create a yearly classified image within each regional polygon (Fig. B.3). The landscape throughout much of the Lower Colorado River corridor is stark and can reasonably be described with 3 basic landcover types: 1) highly arid desert regions, 2) narrow riparian zones, and 3) water. As such, we classified images into these 3 basic landcover types and achieved >97% classification accuracy at Imperial, Cibola and Havasu National Wildlife Refuges (Table B.1). The Lower Gila River and Salton Sea regions were more heterogeneous and contained much more agriculture, and therefore necessitated a more nuanced classification scheme. For these 2 regions, we classified pixels into 4 categories: 1) water, 2) bare, 3) natural vegetation, and 4) agriculture. We then applied the year-specific classified image to remove all pixels not designated as natural vegetation from subsequent analyses (Fig. B.3). We describe each step in more detail below.

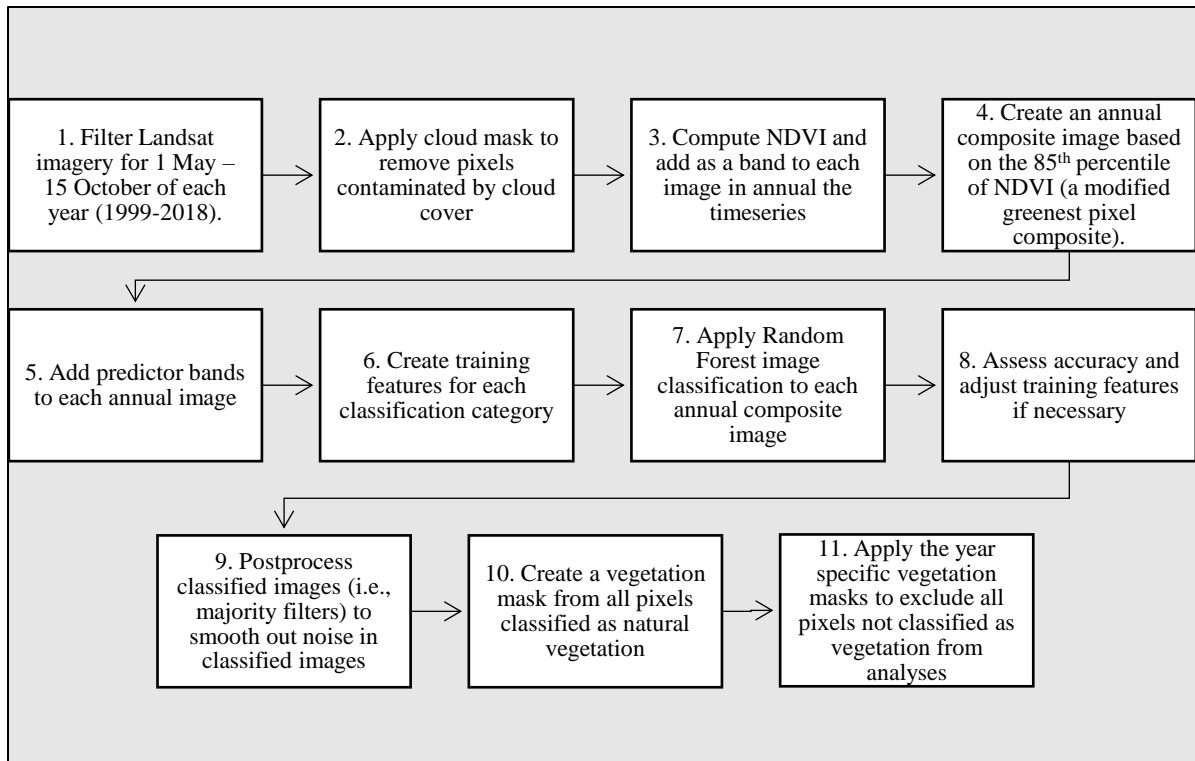


Figure B.2. Vegetation mask derivation process. We used the vegetation masks to remove all pixels not classified as natural vegetation, thereby reducing the influence of non-vegetated pixels on the calculation of marsh condition covariates.

### 6.1 –6.4 Annual summer NDVI composite

Creating composite images from a collection of multitemporal imagery is a common approach to reduce the effects of cloud contamination, atmospheric interference, and sensor error (Holben 1986). In this process, a collection of imagery is compressed into a single image based on some measure of pixel quality. For example, in a greenest pixel composites, each pixel location is sorted such that it represents the highest possible NDVI value from the collection of imagery (i.e., images collected during an entire year for the same location; Holben 1986). We created “modified” greenest pixel composites for each year of the study (1999–2018). Greenest pixel composite images caused problems with subsequent image classification, particularly along: 1) shallow areas of the Colorado River where submerged vegetation can temporarily be exposed and cause spikes in NDVI values and 2) desert washes with sparse vegetation that will temporarily “green-up” after a rain event. When we created a composite image with the highest possible NDVI for each pixel, we experienced increased image classification error (i.e., shallow parts of the river and desert washes were classified as riparian vegetation). We alleviated these problems by creating greenest pixel composite based on the 85<sup>th</sup>

percentile NDVI values. Moreover, classification accuracy was higher for summer composites (i.e., composites built from imagery collected during the summer) than winter or full annual composites. As such, we created yearly composite images from all LS7 imagery collected during 1 May Year<sub>*t*</sub> – 15 October Year<sub>*t*</sub>;  $t = 2006, \dots, 2018$ . We then used these composite images to create year-specific vegetation masks, as discussed below.

### *6.5 Predictor bands*

For Imperial, Cibola, and Havasu National Wildlife Refuge (i.e., those areas with 3-category classification schemes) we used TCW, TCB, TCG, NDMI, and NDSI as predictor bands in the classification. TCW, TCG, NDMI, and NDSI correlate with vegetation condition and soil moisture content. TCB reflects the brightness of the image and helped the models discern bare features (which are much brighter than water and vegetation).

We incorporated temporal dynamics to improve the classification throughout the Lower Gila River and Salton Sea regions (Geerken et al. 2005, Geerken 2009). The Salton Sea and Lower Gila River were heavily interspersed with agriculture, which complicated classification. We fit first order harmonic trend models to a 20-year NDVI (vegetation greenness) timeseries for each pixel in the region to estimate the amplitude and timing of annual change. Agricultural fields are harvested repeatedly throughout the year and thus experience an erratic phenology with repeated high and low NDVI values. Marsh parcels, on the other hand, (typically) exhibit a simple annual cycle with a low NDVI values in the winter and higher NDVI values in the late summer/fall. We improved our ability to accurately discern wetland vegetation from agricultural areas by leveraging their different phenological NDVI cycles and including phase and amplitude (i.e., the timing and magnitude of seasonal change in NDVI) as predictors in the Random Forest classification. Indeed, average classification accuracy in these regions improved from 93.6% ( $\pm 1.1\%$ ) to 97.6% ( $\pm 0.3\%$ ) with the inclusion of phenological covariates.

### *6.6 Training features*

For each study region we selected  $\geq 15$  training features in each category (e.g., water, bare, natural vegetation). We viewed high spatial resolution imagery on Google Earth (not Google Earth Engine) during the study period to ensure the selected training areas remained constant through time (i.e., bare areas remained bare and water features remained as water for duration of study period). We selected training features to represent the full range of spectral variation in each class and scattered them across the extent of the entire image to be classified.

### 6.7 Random forest

In Random Forest, we built a classifier based on the range of spectral values of each training feature in the 5 predictor bands. We then applied the classifier to predict the class (land cover type) of each pixel in the image based on the spectral properties of that pixel (Fig. B.3).



Figure B.3. An example of a classified image clipped to a regional polygon. Green areas are classified as vegetation, blue areas are water and grey areas are bare/desert areas.

### 6.8 Error assessment

To assess accuracy of our classifiers, we randomly partitioned all the pixels in our training features into a training dataset (60% of pixels) and testing dataset (40% of pixels). We then trained the classifier with the training dataset and verified it with the testing data. We assessed the accuracy of the classifier by comparing the classification with the true class of the pixel.

If accuracy was <95%, we adjusted the number and location of training features to better capture the range of spectral values represented by each category and reclassified the image. We iterated this process until we achieved an accuracy >95% for each year of the study window (1999-2018; Table B.1).

Table B.1. Random Forest image classification accuracy for each year and region of the study. NWR = National Wildlife Area and WA = Wildlife Area.

Year	Region			
	Cibola and Imperial NWR	S.B. Salton Sea NWR	Mittry Lake WA and Lower Gila River	Havasu NWR
1999	99.66	97.88	97.24	99.79
2000	99.73	97.77	97.72	99.97
2001	99.76	97.55	97.66	99.90
2002	99.85	97.81	97.14	99.86
2003	99.88	97.70	97.69	99.93
2004	99.18	97.70	97.39	99.86
2005	99.71	97.49	96.82	99.83
2006	99.91	97.88	97.72	99.96
2007	99.78	98.04	97.17	99.93
2008	99.79	97.77	97.47	100.00
2009	99.72	97.96	97.01	99.86
2010	99.68	97.98	97.31	99.93
2011	99.90	97.98	97.79	99.90
2012	99.86	97.76	96.88	99.76
2013	99.74	97.57	97.53	99.87
2014	99.75	97.65	97.27	99.76
2015	99.86	97.83	97.73	99.97
2016	99.91	97.54	98.11	99.93
2017	99.87	97.67	97.67	99.97
2018	99.96	97.54	97.24	99.89

### 6.9 Postprocessing of classified imagery

Pixel-based image classification often results in some isolated, misclassified pixels (Lillesand and Kiefer 1994). As such, classification postprocessing is often applied to reduce this so called “salt and pepper” effect and improve the accuracy of the original classified image (Huang et al. 2014). We used a simple majority filter, in which each pixel is reclassified as the majority class in an  $N \times N$  pixel neighborhood (Stuckens et al. 2000). If no class represents the majority in the neighborhood, pixels are left unchanged. We used a  $2 \times 2$ -pixel neighborhood because many wetland parcels in our study system were quite small and the riparian zone along the Lower Colorado River can be narrow. A small moving window minimized the risk of smoothing out narrow bands of correctly classified vegetation pixels.

### 6.10 – 6.11 Vegetation masking

We aggregated all pixels not classified as natural vegetation to create a binary vegetation/non-vegetation mask. We used the year-specific vegetation mask to remove non-vegetation pixels from all 12 monthly images in the corresponding year. We iterated this process for all years in the timeseries.

### 7. Spatial averages

Once all non-vegetation pixels were removed from the monthly images, we computed the average spectral index value from all pixels in a 224-m buffer around the marsh bird survey points.

### 8. Export index-specific timeseries

Through the processes described above, we built a 20-year timeseries (with 240 monthly values) for each spectral index of interest at each marsh bird survey point and disturbance footprint (>9,000 timeseries). We exported these data from Google Earth Engine for analyses in R (R Core Team 2018).

### 9. Linear interpolation

Cloud contamination occasionally caused missing images in the timeseries (Table B.2). Missing images were rarely sequential (<1% of all missing images occurred on sequential months). As such, we relied on linear interpolation to fill any gaps in the timeseries. Linear interpolation fits a line between the nearest known data points to estimate the value of the missing data. We iteratively applied a linear interpolation to each index-specific timeseries for each marsh bird survey point to ensure a complete timeseries. We graphically inspected interpolated timeseries to assess performance of the interpolation. We performed all linear interpolations with the convenience package, *imputeTS* in R.

Table B.2. Cloud contamination occasionally caused gaps in the Landsat timeseries extracted for each marsh bird survey point. Image region is the “clipping region” in which we processed Landsat imagery. The number of missing images is the average number of images missing from each marsh bird survey point in the region. % missing is the corresponding percentage of the 240-image timeseries that was missing.

Image region	Avg. # of missing images	% of timeseries missing
Havasu Region	0.1	0.04%
Imperial and Cibola Region	1.2	0.5%
Salton Sea Region	2.8	1.2%
Mittry Lake and Gila River	4.4	1.8%

### Proportion vegetated

We estimated the proportion of vegetation within the 224-m buffer of each marsh bird survey point by summing the number of pixels classified as vegetation, calculating their area (each pixel = 0.09 ha) and dividing by the total area of the buffer (15.78 ha). These estimates likely contained error among years due to misclassification in the vegetation mask, but we had no reason to suspect the error was systemic. Indeed, our estimates of the vegetated proportion of buffers tracked reasonably well with observed conditions (Fig. B.4)

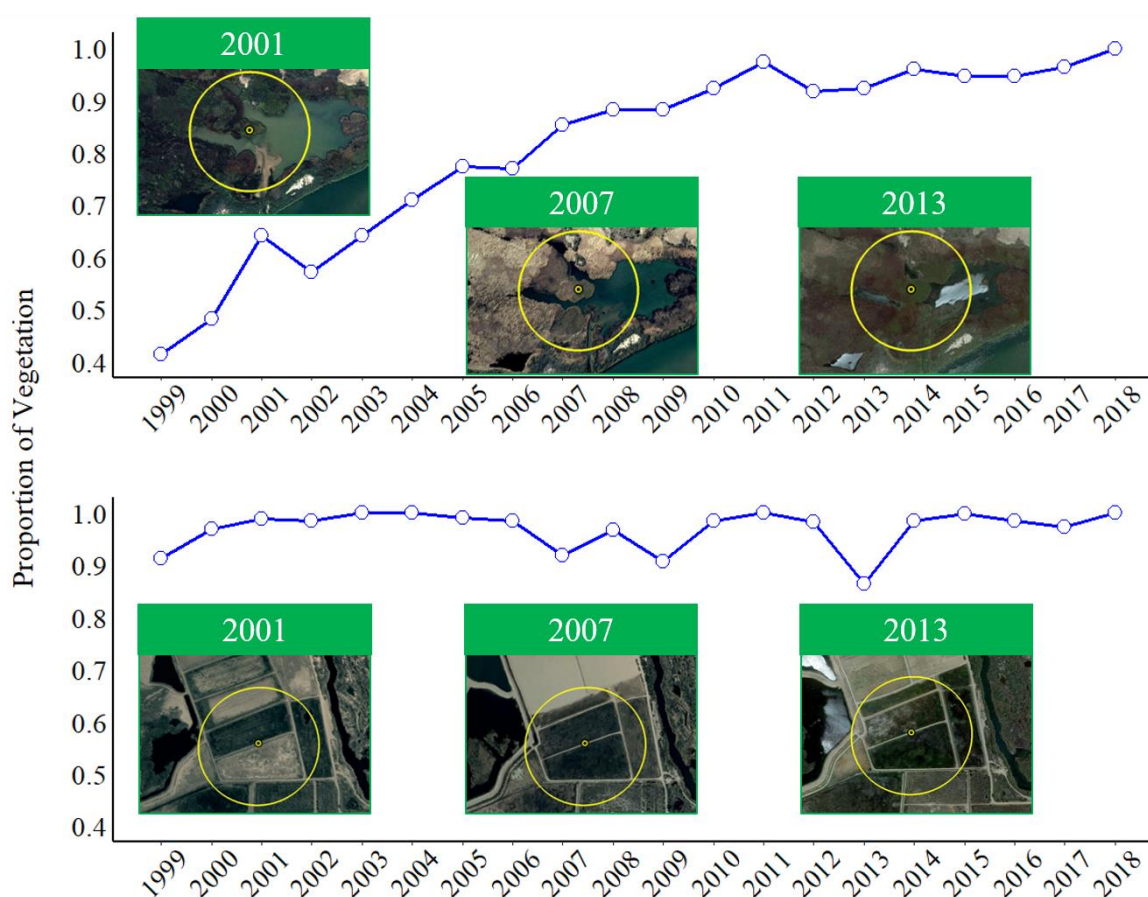


Figure B.4. Proportion of vegetation in the 224-m buffers of survey points through time. The top graph shows proportion of vegetation at an Imperial National Wildlife Refuge managed wetland and the bottom graph shows a more dynamic wetland parcel along the main stem of the Colorado River that experienced a steady increase in wetland vegetation.

## LITERATURE CITED

- Baig, M. H. A., L. Zhang, T. Shuai, and Q. Tong. 2014. Derivation of a Tasseled Cap Transformation based on Landsat 8 at-satellite reflectance. *Remote Sensing Letters* 5:423–431.
- Chignell, S. M., M. W. Luizza, S. Skach, N. E. Young, and P. H. Evangelista. 2018. An integrative modeling approach to mapping wetlands and riparian areas in a heterogeneous Rocky Mountain watershed. *Remote Sensing in Ecology and Conservation* 4:150–165.
- Dahl, T. E. 2006. Remote sensing as a tool for monitoring wetland habitat change. in C. Aguirre-Bravo, P. J. Pellicane, P. D. Burns, and S. Draggan, editors. *Monitoring science and technology symposium: Unifying knowledge for sustainability in the Western Hemisphere. Proceedings RMRS-P-42CD*. Fort Collins, Colorado: US Department of Agriculture, Forest Service, Rocky Mountain Research Station, Denver, Colorado, USA
- Geerken, R. A. 2009. An algorithm to classify and monitor seasonal variations in vegetation phenologies and their inter-annual change. *ISPRS Journal of Photogrammetry and Remote Sensing* 64:422–431.
- Geerken, R., B. Zaitchik, and J. P. Evans. 2005. Classifying rangeland vegetation type and coverage from NDVI time series using Fourier Filtered Cycle Similarity. *International Journal of Remote Sensing* 26:5535–5554.
- Glisson, W. J., C. J. Conway, C. P. Nadeau, and K. L. Borgmann. 2017. Habitat models to predict wetland bird occupancy influenced by scale, anthropogenic disturbance, and imperfect detection. *Ecosphere* 8:1-18
- Gorelick, N., M. Hancher, M. Dixon, S. Ilyushchenko, D. Thau, and R. Moore. 2017. Google Earth Engine: Planetary-scale geospatial analysis for everyone. *Remote Sensing of Environment* 202:18–27.
- Holben, B. N. 1986. Characteristics of maximum-value composite images from temporal AVHRR data. *International Journal of Remote Sensing* 7:1417–1434.
- Huang, C., B. Wylie, L. Yang, C. Homer, and G. Zylstra. 2002. Derivation of a Tasseled Cap Transformation based on Landsat 7 at-satellite reflectance. Raytheon ITSS, USGS EROS Data Center. Sioux Falls, South Dakota, USA

- Huang, X., Q. Lu, L. Zhang, and A. Plaza. 2014. New postprocessing methods for remote sensing image classification: A systematic study. *IEEE Transactions on Geoscience and Remote Sensing* 52:7140–7159.
- Kayastha, N., V. Thomas, J. Galbraith, and A. Banskota. 2012. Monitoring wetland change using inter-annual Landsat time-series data. *Wetlands* 32:1149–1162.
- Lillesand, T. M., and R. W. Kiefer. 1994. *Remote sensing and photo interpretation*. John Wiley and Sons: New York, New York, USA. 950.
- R Core Team. 2018. *R: A language and environment for statistical computing*. R Foundation for Statistical Computing. Vienna, Austria. <https://www.R-project.org/>.
- Stuckens, J., P. R. Coppin, and M. E. Bauer. 2000. Integrating contextual information with per-pixel classification for improved land cover classification. *Remote Sensing of Environment* 71:282–296.
- Wilén, B. O., and M. K. Bates. 1995. The US Fish and Wildlife Service's National Wetlands Inventory Project. *Vegetatio* 118:153–169.
- Wright, C., and A. Gallant. 2007. Improved wetland remote sensing in Yellowstone National Park using classification trees to combine TM imagery and ancillary environmental data. *Remote Sensing of Environment* 107:582–605.